Abou Bekr Belkaid University
Tlemcen Algeria
جامعة أبي بكر بلقايد
تلمسان الجزائر
PEOPLE'S DEMOCRATIC REPUBLIC OF ALGERIA
الجمهورية الجزائرية الديمقراطية الشعبية
MINISTRY OF HIGHER EDUCATION AND SCIENTIFIC RESEARCH
وزارة التعليم العالي و البحث العلمي
FACULTY OF TECHNOLOGY
DEPARTMENT OF BIOMEDICAL ENGINEERING

A Thesis

Presented for obtaining the degree of:

DOCTORATE

In: Biomedical Engineering
Specialty: Biomedical Instrumentation

By:

Hakkoum Khaoula Nour El Houda

Theme

Early detection of pathological behaviors by studying heart sounds

Thesis defended on .... at Tlemcen in Front of the Jury Composed of:

Mr HADJ SLIMANE Zine-Eddine	Full Professor	University of Tlemcen	President
Mr HAMZA CHERIF Lotfi	Associate Professor	University of Tlemcen	Supervisor
Mr DIB Nabil	Associate Professor	University of Tlemcen	Examiner
Mr BENDALHOUM Soufiane	Associate Professor	University of El Bayadh	Examiner
Mr KURSAD UCAR Muhammed	Associate Professor	University of Sakarya	Guest

Academic Year 2024/2025

Dedication

To my beloved parents,
Bachir Hakkoum and Meriem Yamani,
whose unwavering love and support have been my guiding light.

To my brothers and sisters,
thank you for your encouragement and belief in me.

To my best friend from the mosque on campus,
your friendship has been a source of strength and joy.

And to my colleagues in Turkey, Hazal Hilal Yordan and Samia Dardour ,
thank you for your collaboration and support during this journey.

This work is dedicated to all of you,
who have inspired and motivated me every step of the way.

Acknowledgments

First and foremost, I would like to express my deepest gratitude to Allah, who has given me the strength and energy to complete my PhD.

I am profoundly grateful to my thesis supervisor, Professor Hamza Cherif Lotfi, for his unwavering guidance and support throughout my doctoral journey. His expertise and encouragement have been invaluable.

I would also like to extend my heartfelt thanks to Professor Muhammed Kursad Ucar from the Faculty of Engineering, Department of Electrical and Electronics Engineering, Turkey, who welcomed me into his laboratory and provided me with essential guidance and assistance during my research.

My sincere appreciation goes to my brother Hakkoum Abdelkader, a professor of chemistry, for his insightful advice and support throughout my thesis work. Additionally, I would like to thank Mme Kholkhal Chahrazed, our laboratory engineer, for her assistance and support.

I would also like to express my gratitude to the jury members who evaluated my dissertation and provided invaluable feedback that helped improve my work.

To all my colleagues and everyone who contributed to my success and wished me well along this journey, your support, collaboration, and camaraderie have made this experience much more enriching and enjoyable.

Thank you all for being an integral part of my academic journey.

قال رسول الله صلى الله عليه وسلم:

من سلك طريقًا يطلبُ فيه علمًا، سلك اللهُ به طريقًا من طرقِ الجنةِ، وإنَّ الملائكةَ لتضعُ أجنحتَها رضًا لطالبِ العلمِ، وإنَّ العالمَ ليستغفرُ له من في السماواتِ ومن في الأرضِ، والحيتانُ في جوفِ الماءِ، وإنَّ فضلَ العالمِ على العابدِ كفضلِ القمرِ ليلةَ البدرِ على سائرِ الكواكبِ، وإنَّ العلماءَ ورثةُ الأنبياءِ، وإنَّ الأنبياءَ لم يُورِّثُوا دينارًا ولا درهمًا، ورَّثُوا العلمَ فمن أخذَه أخذ بحظٍّ وافرٍ.

الراوي: أبو الدرداء
المحدث: الألباني
المصدر: صحيح أبي داود
الصفحة أو الرقم: 3641
خلاصة حكم المحدث: صحيح
التخريج: أخرجه أبو داود (3641) واللفظ له، والترمذي (2682)، وابن ماجه (223)، وأحمد (21715)

General Introduction

Cardiovascular diseases (CVDs) remain one of the leading causes of morbidity and mortality worldwide. The early detection and effective management of cardiac pathologies are critical in improving patient outcomes and reducing healthcare costs. Traditional methods for assessing cardiovascular health often rely on invasive procedures or subjective interpretations of diagnostic data. Recent advances in signal processing and artificial intelligence (AI) offer promising alternatives for non-invasive cardiovascular monitoring.

Phonocardiography (PCG) is a valuable tool in the non-invasive assessment of heart sounds, providing insights into cardiac function. Despite its potential, the analysis of PCG signals has faced challenges related to noise interference, signal complexity, and the need for accurate interpretation. This thesis aims to explore sophisticated methods for signal processing techniques to enhance the analysis of PCG signals and intracardiac pressure estimation, thereby improving the diagnostic accuracy for various cardiac conditions.

The integration of AI methodologies, particularly machine learning algorithms, offers the potential to revolutionize the landscape of cardiac diagnostics. By leveraging large datasets and sophisticated algorithms, we can automate the detection of pathological features in PCG signals, leading to timely and accurate diagnoses.

Furthermore, non-invasive methods for estimating intracardiac pressure can provide critical information for diagnosing conditions such as heart failure and valvular disorders, which are often difficult to assess with traditional techniques.

Thesis Objectives

The following are the main goals of this thesis:

To investigate advanced signal processing techniques for the extraction and analysis of features from phonocardiogram signals, with a focus on improving the signal-to-noise ratio and enhancing the clarity of cardiac sounds.

To develop machine learning algorithms tailored for the classification and identification of cardiac pathologies based on extracted features from PCG signals.

To explore non-invasive methods for estimating intracardiac pressure, assessing their effectiveness and reliability compared to traditional invasive measurements.

To evaluate the integration of AI methodologies with traditional cardiac monitoring practices, analyzing their impact on diagnostic accuracy and clinical outcomes.

To propose a comprehensive framework for the early detection and management of cardiac diseases that incorporates advanced signal processing and AI technologies, ultimately facilitating timely clinical interventions.

Abstract

This thesis investigates advanced signal processing techniques for the early detection and management of cardiac pathologies, focusing on the analysis of phonocardiogram (PCG) signals and intracardiac pressure estimation. It emphasizes the significance of accurate cardiovascular health assessment as a critical factor in improving patient outcomes. The research employs artificial intelligence (AI) methodologies, leveraging machine learning algorithms to enhance the accuracy of pathological identification in PCG signals. Additionally, it explores non-invasive methods for estimating cardiac pressures, highlighting their crucial role in diagnosing conditions such as heart failure, valvular disorders, and pulmonary hypertension. The findings demonstrate that integrating AI with traditional cardiac monitoring can significantly improve diagnostic precision, facilitating timely clinical interventions and paving the way for more effective cardiovascular disease management.

Keywords: Phonocardiogram, cardiac pathologies, signal processing, artificial intelligence, intracardiac pressure, non-invasive methods, heart disease.

Résumé

Cette thèse étudie des techniques avancées de traitement du signal pour la détection précoce et la gestion des pathologies cardiaques, en se concentrant sur l'analyse des signaux phonocardiographiques (PCG) et l'estimation de la pression intracardiaque. Elle souligne l'importance d'une évaluation précise de la santé cardiovasculaire en tant que facteur critique pour améliorer les résultats pour les patients. La recherche utilise des méthodologies d'intelligence artificielle (IA), exploitant des algorithmes d'apprentissage automatique pour améliorer la précision de l'identification pathologique dans les signaux PCG. De plus, elle explore des méthodes non invasives pour estimer les pressions cardiaques, mettant en évidence leur rôle crucial dans le diagnostic de conditions telles que l'insuffisance cardiaque, les troubles valvulaires et l'hypertension pulmonaire. Les résultats montrent que l'intégration de l'IA avec la surveillance cardiaque traditionnelle peut améliorer significativement la précision diagnostique, facilitant ainsi des interventions cliniques opportunes et ouvrant la voie à une gestion plus efficace des maladies cardiovasculaires.

Mots-clés : Phonocardiogramme, pathologies cardiaques, traitement du signal, intelligence artificielle, pression intracardiaque, méthodes non invasives, maladies cardiaques.

ملخص

تبحث هذه الرسالة في تقنيات معالجة الإشارات المتقدمة للكشف المبكر وإدارة الأمراض القلبية، مع التركيز على تحليل إشارات (PCG) وتقدير الضغط داخل القلب. ويؤكد البحث على أهمية تقييم صحة القلب والأوعية الدموية بدقة كعامل حاسم في تحسين نتائج المرضى. يستخدم البحث منهجيات الذكاء الاصطناعي ،(AI) مستفيداً من خوارزميات التعلم الآلي لتعزيز دقة تحديد الأمراض في إشارات .PCG بالإضافة إلى ذلك، يستكشف طرقًا غير جراحية لتقدير ضغوط القلب، مشددًا على دورها الحاسم في تشخيص حالات مثل فشل القلب، واضطرابات الصمامات، وارتفاع ضغط الدم الرئوي. تظهر النتائج أن دمج الذكاء الاصطناعي مع المراقبة القلبية التقليدية يمكن أن يحسن بشكل كبير من الدقة التشخيصية، مما يسهل التدخلات السريرية في الوقت المناسب ويفتح الطريق لإدارة أكثر فعالية لأمراض القلب والأوعية الدموية.

الكلمات المفتاحية: الإشارات الميكانيكية القلبية PCG ، الأمراض القلبية، معالجة الإشارات، الذكاء الاصطناعي، الضغط داخل القلب، طرق غير جراحية، أمراض القلب.

CHAPTER 1

Study of the Phonocardiogram signal and cardiac pathologies

Contents

List of Figures

1.1 Introduction

1

The assessment of cardiovascular health is of paramount importance in modern medicine, as cardiovascular diseases remain a leading cause of morbidity and mortality worldwide. Among the various diagnostic modalities available, the phonocardiogram (PCG) signal has emerged as a promising non-invasive tool for the evaluation of cardiac structure and function.

The PCG signal represents the acoustic vibrations generated during the cardiac cycle and provides valuable information about the mechanical events occurring within the heart. Over the past decades, extensive research has been conducted to explore the diagnostic potential of PCG signals in the context of various cardiac pathologies [21] [3] [12] The analysis of PCG waveforms has been particularly useful in the detection and monitoring of valve diseases, as specific alterations in the timing, intensity, and characteristics of the four primary heart sounds (S1, S2, S3, and S4) can serve as markers of underlying structural or functional abnormalities [4] .

Common valve pathologies, such as mitral valve prolapse, aortic stenosis, and mitral regurgitation, have been shown to exhibit distinct PCG signal patterns [38] [17] In addition to valve diseases, PCG analysis has also demonstrated potential in the assessment of myocardial abnormalities and hemodynamic changes [39] [62].The identification of subtle variations in the PCG signal can provide insights into the functional status of the heart, potentially aiding in the early detection and management of cardiovascular disorders. Numerous computational techniques, including artificial neural networks [83] [7] [59] support vector machines [50] [79] and decision trees [80] [63] have been explored for the automated analysis and classification of PCG signals. These approaches have shown promising results in the detection and differentiation of various cardiac pathologies based on PCG signal features. Despite the growing body of evidence supporting the clinical utility of PCG analysis, the widespread adoption of this technique in routine medical practice has been limited. This can be attributed to the inherent subjectivity of traditional auscultation methods, as well as the need for more standardized and automated approaches to PCG signal processing and interpretation [42] [6] [72]. PCG signal study seeks to diagnosis in the field of cardiology. The findings of this research may contribute to the development of advanced, non-invasive techniques for the early detection, risk stratification, and management of cardiac diseases, ultimately leading to improved patient outcomes and more efficient healthcare delivery.

1.2 Heart anatomy and functioning

The human heart is situated within the thoracic cavity, specifically in the middle mediastinal compartment, superior to the diaphragm. The size of the normal adult heart varies based on individual differences in height and weight, typically weighing 300-350 grams in males and 250-300 grams in females [1]. The right ventricular wall measures 0.3-0.5 cm in thickness, while the left ventricular wall is thicker, measuring 1.3-1.5 cm [74] [82].

The heart is divided into four distinct chambers - the left and right atria, and the left and right ventricles (Figure 1.1). It is composed of three layers: the epicardium, myocardium, and endocardium. The heart is encased within a double-walled fibroserous sac known as the pericardium, which is further divided into the fibrous pericardium and the serous pericardium. The fibrous pericardium envelops the heart and attaches to the great vessels. The serous pericardium is a closed sac consisting of a visceral layer (the epicardium) and a parietal layer. This space between the two serous layers contains pericardial fluid, which lubricates the heart's surface and prevents friction during cardiac motion [32] [74].

The electrical activity of the heart can be detected through electrocardiography (ECG), which measures the electrical potentials generated by the depolarization and repolarization of the myocardium [51]. The mechanical activity of the heart can be detected through phonocardiography (PCG), which measures the

vibrations and sounds generated by the opening and closing of the heart valves, as well as the turbulent blood flow during the cardiac cycle [40].

The human heart contains four main valves that regulate the unidirectional flow of blood through the cardiovascular system: the aortic valve, mitral valve, tricuspid valve, and pulmonary valve. These valves are composed of thin, flexible leaflets that open and close in response to changes in pressure within the heart chambers.

During diastole, when the ventricles are relaxing and filling with blood, the mitral and tricuspid valves are open, allowing blood to flow from the atria into the ventricles. The aortic and pulmonary valves are closed during this phase, preventing backflow of blood. As the ventricles contract during systole, the mitral and tricuspid valves close, while the aortic and pulmonary valves open, allowing blood to be pumped out of the ventricles and into the aorta and pulmonary arteries, respectively.

The pressure changes within the heart chambers are the driving force behind the opening and closing of the valves. During ventricular diastole, the pressure in the atria is higher than the pressure in the ventricles, causing the mitral and tricuspid valves to open. As the ventricles contract during systole, the pressure in the ventricles rises, exceeding the pressure in the atria and the aorta/pulmonary artery, causing the mitral and tricuspid valves to close and the aortic and pulmonary valves to open. The degree

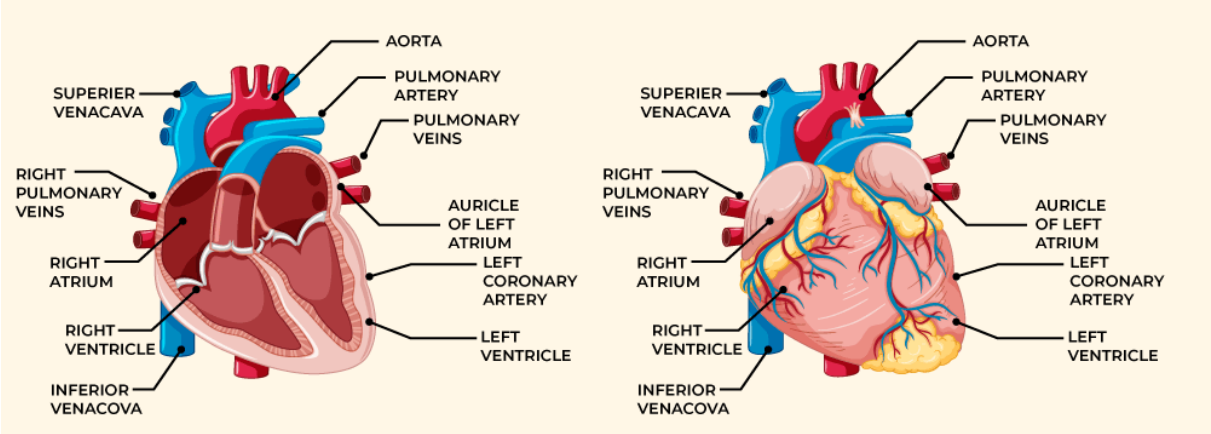

Figure 1.1: Heart Anatomy

of pressure concentration within the heart chambers and great vessels follows a gradient, from the lowest pressure in the right atrium (0-8 mmHg) to the highest pressure in the left ventricle (up to 120 mmHg) [40] . This pressure gradient is essential for the proper functioning of the heart valves and the efficient circulation of blood throughout the body.

1.3 Cardiac auscultation

Cardiac auscultation is one of the most valuable techniques for diagnosing disease. Auscultation of the heart primarily involves listening to the sounds that occur within the body using a stethoscope (Figure 1.2). These heart sounds are primarily caused by the turbulence of blood flow during the closing of the cardiac valves [23]. A systematic approach to cardiac auscultation is required for each patient. The examination should first focus on identifying the physiological heart sounds heard at the various auscultation sites. After characterizing the normal first and second heart sounds, the clinician should then assess for the presence of any additional abnormal heart sounds before evaluating the respiratory sounds.

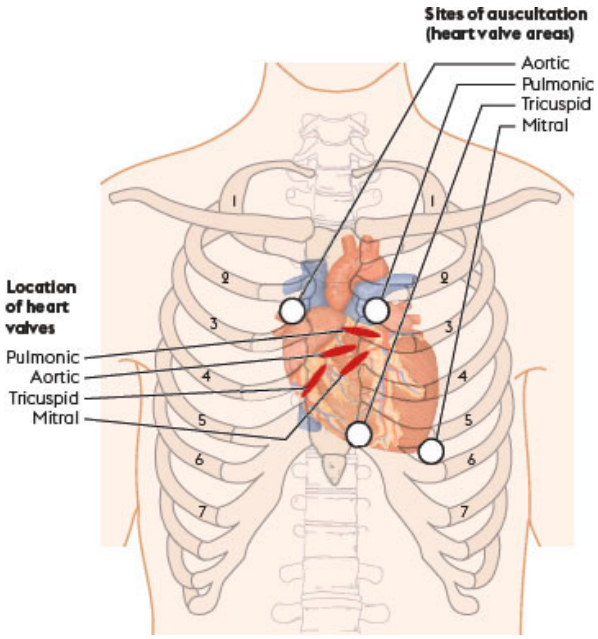

Figure 1.2: Cardiac auscultation

1.4 PCG Signal

The phonocardiogram (PCG) is an acoustic recording of the heart sounds produced by the mechanical activity of the heart (Figure 1.3). The PCG signal represents the vibrations and turbulent blood flow that occur within the cardiovascular system, which can be detected and recorded using a sensitive microphone or sensor placed on the chest wall [68]

Frequency Range: 20-600 Hz [68] [45] .

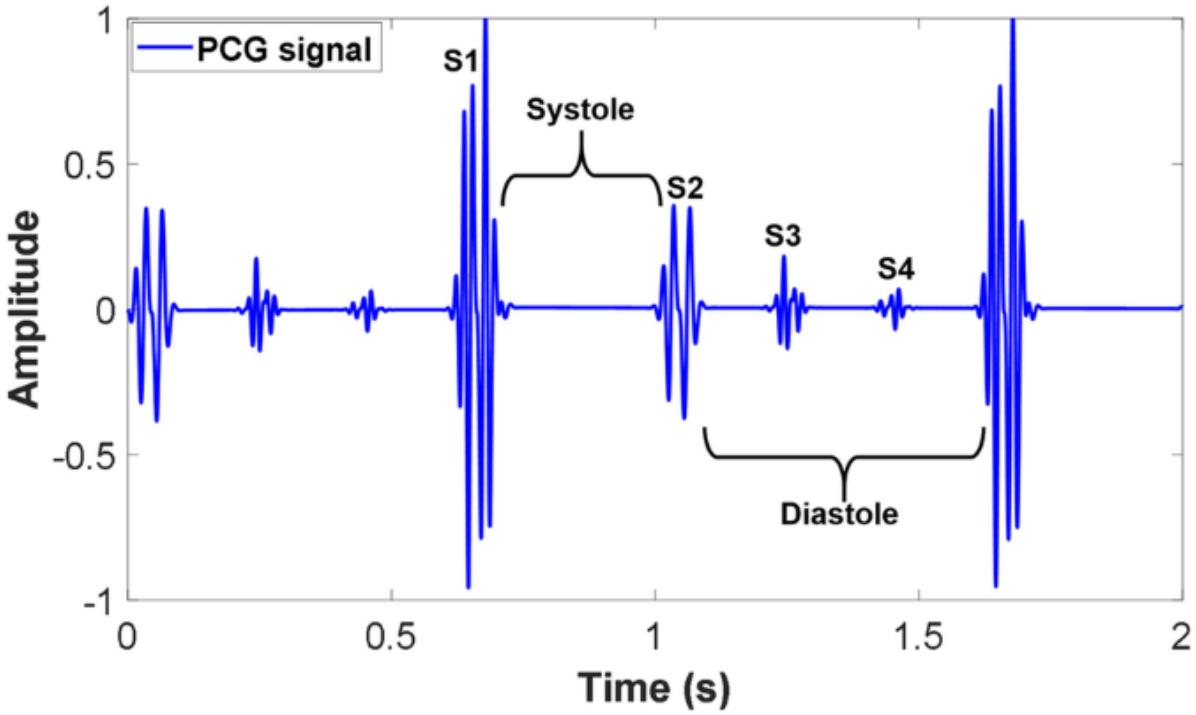

Figure 1.3: PCG Signal

1.5 Heart Sounds

Heart sounds are the noises generated by the mechanical activity of the heart, specifically the opening and closing of the cardiac valves, as well as the flow of blood through the heart chambers and great vessels. These sounds are caused by the vibrations of the heart, blood, and surrounding tissues, and can be heard through auscultation using a stethoscope [24].

1.5.1 First Heart Sound (S1)

Definition: The first heart sound (S1) is the sound produced by the closure of the atrioventricular (AV) valves, namely the mitral and tricuspid valves, at the beginning of ventricular systole.
Production: S1 is generated by the sudden deceleration and closure of the AV valves as the ventricles contract and the intraventricular pressure rises, causing the valve leaflets to snap shut [24] [46].
Time Interval: Occurs at the beginning of ventricular systole
Frequency Range: 25-45 Hz [37] [24]
Duration: 100-200 ms [24] [19]

1.5.2 Second Heart Sound (S2)

Definition: The second heart sound (S2) is the sound produced by the closure of the semilunar valves, namely the aortic and pulmonary valves, at the end of ventricular systole.
Production: S2 is generated by the sudden deceleration and closure of the semilunar valves as the ventricles relax, and the pressure in the aorta and pulmonary artery exceeds the ventricular pressure, causing the valve leaflets to snap shut [24] [46].
Time Interval: Occurs at the end of ventricular systole
Frequency Range: 50-70 Hz [37] [24]
Duration: 80-120 ms [24] [19]

1.5.3 Third Heart Sound (S3)

Definition: The third heart sound (S3) is an abnormal low-pitched, early diastolic sound that is caused by the rapid and forceful filling of the ventricles during early diastole.
Production: S3 is produced by the sudden deceleration of blood flow into the rapidly filling ventricles, causing the ventricular walls to vibrate [46] [9].
Time Interval: Early diastolic
Frequency Range: 20-30 Hz [37] [24]
Duration: 60-100 ms [24] [9]

1.5.4 Fourth Heart Sound (S4)

Definition: The fourth heart sound (S4) is an abnormal late diastolic sound that is caused by the atrial contraction and the sudden increase in ventricular pressure during the final phase of diastole.
Production: S4 is generated by the vibrations of the ventricular walls as they are suddenly stretched by the additional volume of blood pumped in by the atrial contraction [46] [9].
Time Interval: Late diastolic
Frequency Range: 20-30 Hz [37] [24]
Duration: 60-100 ms [24] [9]
Cardiac valve pathologies refer to any abnormalities or dysfunctions affecting the heart's four main valves: the mitral valve (located between the left atrium and left ventricle), the tricuspid valve (located between

the right atrium and right ventricle), the aortic valve (located between the left ventricle and the aorta), and the pulmonary valve (located between the right ventricle and the pulmonary artery). These valves play a crucial role in ensuring the proper and efficient flow of blood through the cardiovascular system. The mitral and tricuspid valves regulate the flow of blood from the atria to the ventricles, while the aortic and pulmonary valves control the outflow of blood from the ventricles to the systemic and pulmonary circulations, respectively. Disruptions to their normal structure and function can lead to various clinical conditions that can significantly impact a patient's health and quality of life.

1.6 Cardiac Pathologies

1.6.1 Aortic Stenosis

Aortic stenosis is a valvular heart disease characterized by the narrowing or obstruction of the aortic valve opening (Figure1.4), which impedes the normal flow of blood from the left ventricle to the aorta [56] [11]. This condition is typically caused by the gradual thickening, calcification, and reduced mobility of the aortic valve leaflets, leading to a reduction in the effective valve orifice area [14] [8].
The most common causes of aortic stenosis include age-related degenerative changes, congenital bicuspid aortic valve, and rheumatic heart disease [34] [77]. Less common etiologies include radiation therapy, inflammatory conditions, and certain metabolic disorders [34] [75]. As the valve narrows, the left ventricle must generate higher pressures to overcome the obstruction, leading to left ventricular hypertrophy and increased myocardial workload [36] [26].
Aortic stenosis can progress over time, and severe cases can result in left ventricular dysfunction, pulmonary hypertension, and ultimately heart failure [44] [49]. Patients with aortic stenosis may experience symptoms such as exertional dyspnea, angina, syncope, and heart failure, with the severity of symptoms often correlating with the degree of valve obstruction [53] [71].
Comprehensive evaluation and management of aortic stenosis typically involve echocardiography, cardiac imaging, and careful monitoring of disease progression[56] [65]. Definitive treatment options include surgical aortic valve replacement or transcatheter aortic valve implantation, depending on the patient's clinical characteristics and risk profile [69] [8].

Auscultation and Phonocardiography in Aortic Stenosis

1. Murmur Characteristics

    - In aortic stenosis, a systolic ejection murmur is typically heard, best heard at the right upper sternal border and radiating to the carotid arteries [60] [22].

    - The murmur is crescendo-decrescendo in nature, starting shortly after the first heart sound (S1) and ending before the second heart sound (S2) (Figure 1.5) [8] [36].

    - The murmur intensity and duration are related to the severity of the aortic stenosis, with a louder and longer murmur indicating more severe obstruction [53] [25].

2. Phonocardiographic Findings

    - On the phonocardiogram (PCG) , the systolic ejection murmur of aortic stenosis typically has a "diamond-shaped" configuration, with a rapid upstroke and a gradual downslope [54] [25].

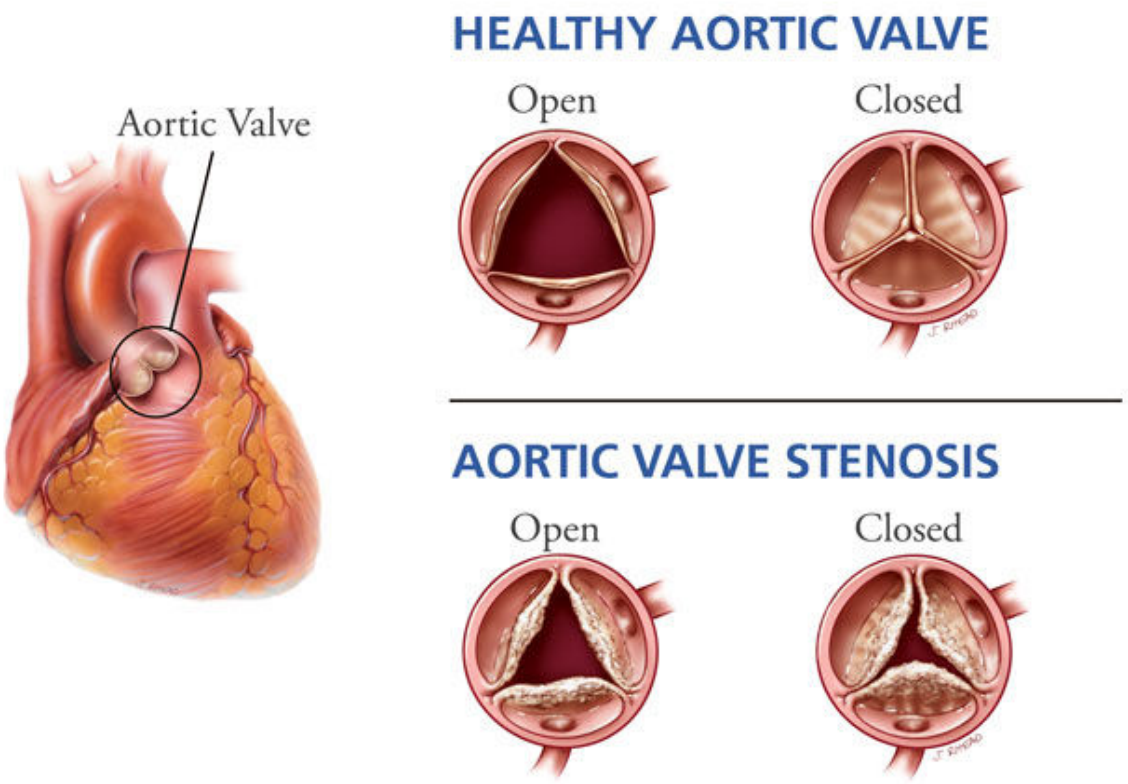

Figure 1.4. Aortic Stenosis

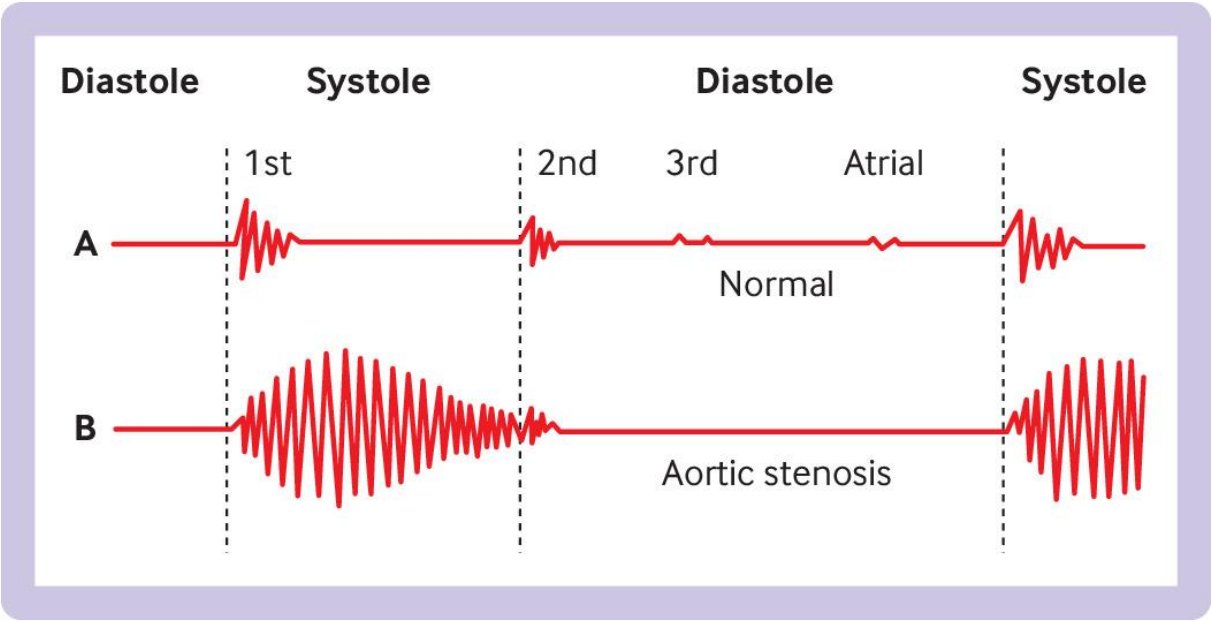

Figure 1.5. PCG Aortic Stenosis

- The timing of the murmur onset and duration can provide information about the severity of the stenosis, with a longer murmur duration indicating more severe disease [30] [47].
- Additional findings on the PCG may include a soft or delayed S2 sound, which can occur due to the increased afterload on the left ventricle [44] [26].

3. Murmur Location

   - The systolic murmur of aortic stenosis is typically heard best at the right upper sternal border, where the aortic valve is located [56] [65].
   - The murmur may also radiate to the carotid arteries, reflecting the high-velocity flow through the narrowed aortic valve [71] [69].
   - Careful auscultation and palpation of the carotid arteries can provide additional information about the severity of the aortic stenosis [8] [34].

1.6.2 Mitral Stenosis

Mitral stenosis is a valvular heart disease characterized by the narrowing or obstruction of the mitral valve orifice (Figure 1.6), which is the opening between the left atrium and the left ventricle [60]. This condition impedes the flow of blood from the left atrium to the left ventricle, leading to an increase in left atrial pressure and a decrease in left ventricular filling [29] [58].

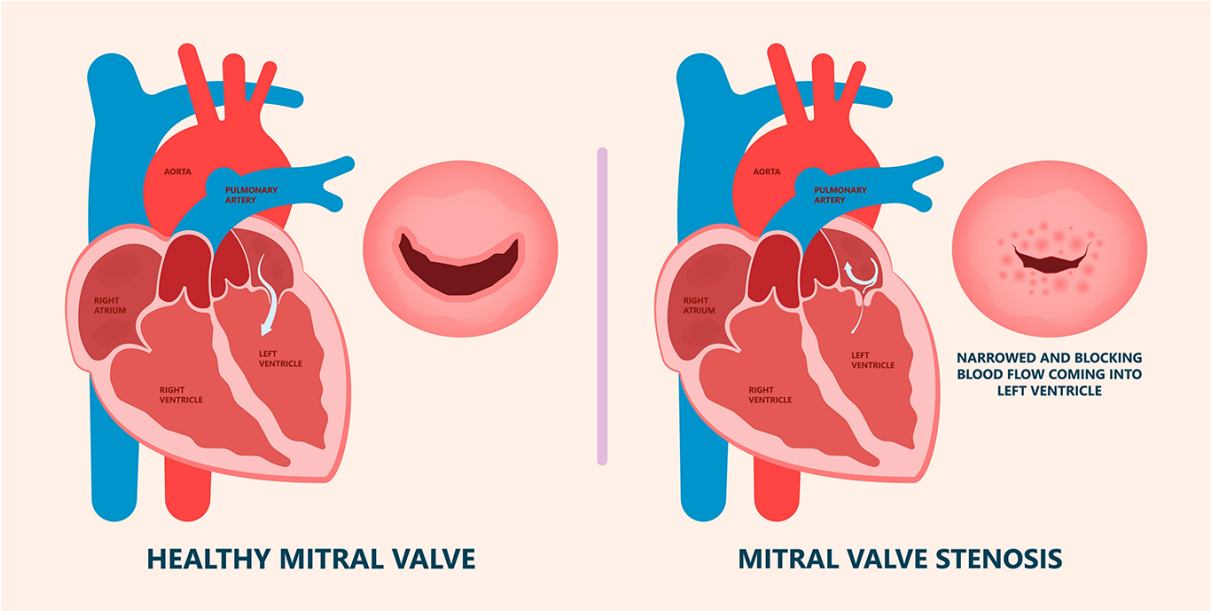

Figure 1.6. Mitral Stenosis

The most common cause of mitral stenosis is rheumatic heart disease, which results from an autoimmune response triggered by a previous streptococcal infection, such as rheumatic fever [15] [52]. Other, less common causes include congenital abnormalities, commissural fusion, and mitral annular calcification [13].

The narrowing of the mitral valve orifice leads to a gradual increase in left atrial pressure, which can eventually lead to pulmonary congestion, shortness of breath, and other symptoms [48]. The severity of mitral stenosis is typically classified based on the mitral valve area, with mild stenosis defined as a valve area greater than 1.5 cm^2, moderate stenosis as a valve area between 1.0 and 1.5 cm^2, and severe stenosis as a valve area less than 1.0 cm^2 [53].

Patients with mitral stenosis may present with a variety of symptoms, including shortness of breath, fatigue, chest pain, palpitations, and peripheral edema [26] [44] . The physical examination often reveals a characteristic diastolic murmur, best heard at the apex of the heart [61] [65].

Diagnosis of mitral stenosis is typically made through echocardiography, which can provide detailed information about the anatomy and function of the mitral valve [67] [28]. Other diagnostic tests, such as cardiac catheterization, may be used to further evaluate the severity of the stenosis and to guide treatment decisions [55] [69].
Treatment for mitral stenosis may include medications to manage symptoms and prevent complications, as well as interventional procedures, such as percutaneous balloon valvuloplasty or surgical mitral valve replacement, for more severe cases [14] [43].

Auscultation and Phonocardiography in Mitral Stenosis

1. Mitral stenosis typically presents with distinct changes in the PCG waveform [2] [73]. The key features that can be observed in the PCG signal include:

   - Delayed and prolonged first heart sound (S1) (Figure 1.7):
     In mitral stenosis, the closure of the mitral valve is delayed, resulting in a delayed and prolonged S1 [81] [27].
   - Opening snap (OS):
     The opening of the narrowed mitral valve creates an audible snap, which can be detected in the PCG signal as a high-frequency vibration immediately after S1 [76].
   - Diastolic murmur:
     A characteristic diastolic murmur, best heard at the apex of the heart, can be observed in the PCG signal. This murmur is caused by the turbulent flow of blood through the narrowed mitral valve orifice [5] [41] .

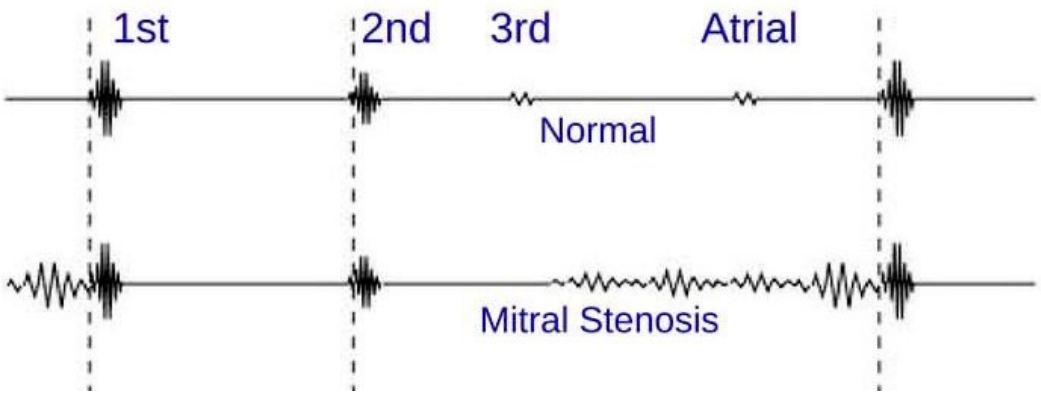

Figure 1.7. PCG Mitral Stenosis

2. Murmur Location

   The location of the murmur can also provide valuable information about the underlying valvular pathology. In the case of mitral stenosis, the murmur is typically:

   - Best heard at the apex of the heart (over the mitral valve area) [35].
   - Radiates to the left axilla and may be heard in the left supraclavicular area [8] [1].
   - Varies in intensity with respiration, often becoming louder during inspiration [13] [58].

1.7 Mitral Regurgitation

1

Mitral Regurgitation is a valvular heart disease characterized by the insufficient closure of the mitral valve , resulting in the backward flow of blood from the left ventricle into the left atrium (Figure 1.8) during ventricular systole [57]. The key aspects of the medical definition of mitral regurgitation are:

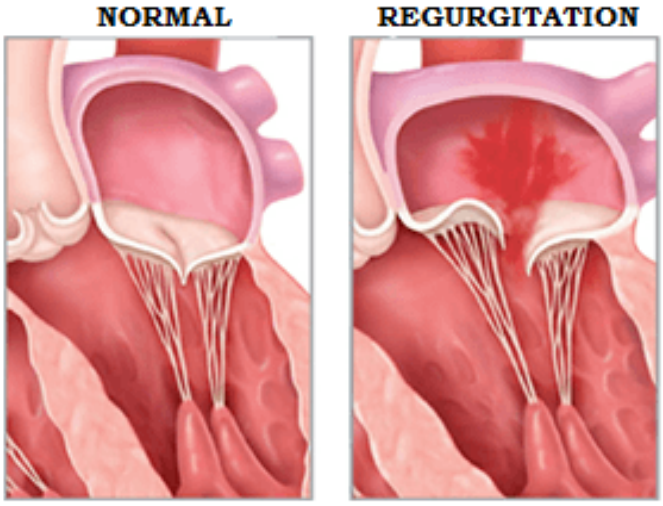

Figure 1.8: Mitral Regurgitation

1. Valvular Heart Disease :
    - Mitral regurgitation is a condition affecting the mitral valve, one of the four main heart valves [60].
    - It is classified as a valvular heart disease, as it involves the structural and functional abnormalities of the mitral valve [57].
2. Insufficient Closure of the Mitral Valve:
    - In a normal functioning mitral valve, the two leaflets (anterior and posterior) close tightly during ventricular systole, preventing the backflow of blood [57].
    - In mitral regurgitation, the mitral valve leaflets do not coapt (come together) properly, leading to an incomplete closure of the valve [57].
3. Backward Flow of Blood:
    - Due to the insufficient closure of the mitral valve, blood flows backward from the left ventricle into the left atrium during ventricular systole [57].
    - This backward flow is known as mitral regurgitation or mitral insufficiency [57].
4. Ventricular Systole:
    - The backward flow of blood occurs specifically during the ventricular systolic phase, when the left ventricle contracts and pumps blood out to the body [57].

Mitral regurgitation can have various underlying causes, such as mitral valve prolapse [33], rheumatic heart disease [16], ineffective endocarditis [66], or ischemic heart disease [31]. The severity of mitral regurgitation can range from mild to severe, and it can lead to volume overload in the left atrium and left ventricle, potentially causing heart enlargement, arrhythmias, heart failure, and other complications if left untreated [57].

Auscultation and Phonocardiography in Mitral Regurgitation

1. Murmur Characteristics in Mitral Regurgitation:

   Holosystolic Murmur:

   - The characteristic murmur associated with mitral regurgitation is a holosystolic murmur [78] [64].
   - This means the murmur is present throughout the entire systolic phase of the cardiac cycle, beginning with the first heart sound (S1) and ending with the second heart sound (S2) (Figure 1.9) [78] [64].

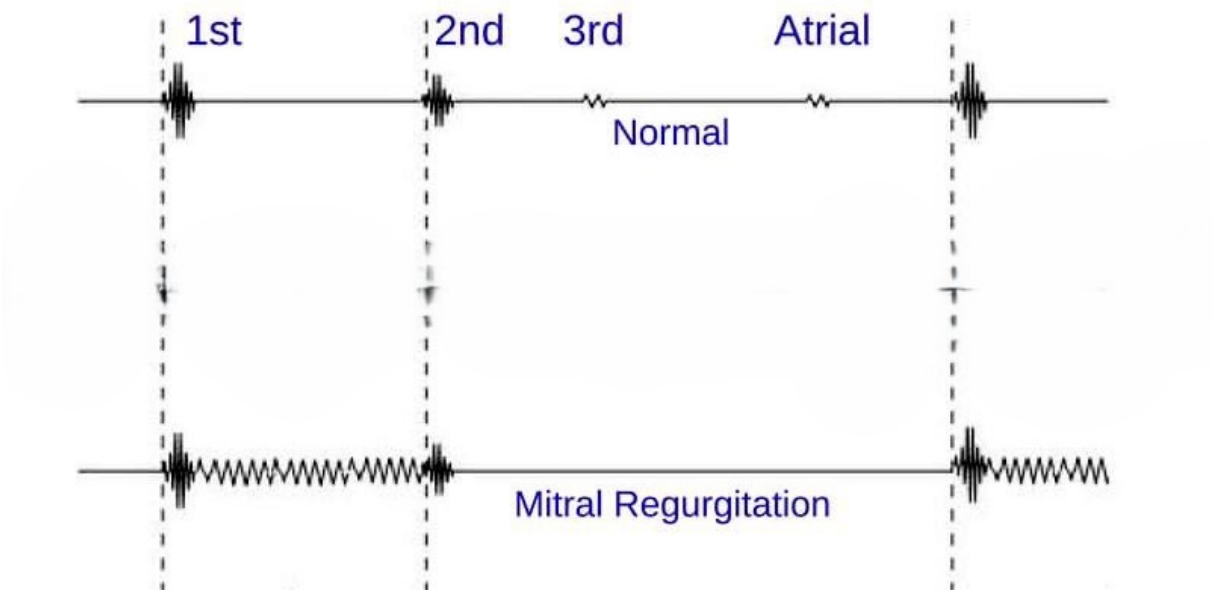

Figure 1.9: PCG Mitral Regurgitation

   Blowing or Swishing Quality:

   - The murmur typically has a ”blowing” or ”swishing” quality, which is caused by the turbulent flow of blood from the left ventricle into the left atrium during systole [78] [64].

   Correlation with Severity:

   - The intensity of the murmur correlates with the severity of the mitral regurgitation [78] [64].
   - Louder and more intense murmurs are generally indicative of more severe mitral regurgitation [78] [64].

2. Phonocardiographic Findings in Mitral Regurgitation:

   Holosystolic Murmur:

- The phonocardiogram in mitral regurgitation typically shows a holosystolic murmur that begins with the first heart sound (S1) and persists throughout systole [70].

Correlation with Severity:

- The intensity and duration of the holosystolic murmur on the phonocardiogram correlate with the severity of the mitral regurgitation [70].
- More severe regurgitation is associated with a louder and longer-lasting murmur on the phonocardiogram [70].

Early Diastolic Murmur:

- In cases of severe mitral regurgitation, the phonocardiogram may also show an early diastolic murmur [70].
- This early diastolic murmur is caused by the rapid flow of blood from the left atrium to the left ventricle during early diastole [70].

3. Murmur Location in Mitral Regurgitation:

Cardiac Apex:

- The holosystolic murmur of mitral regurgitation is best heard at the cardiac apex, which is the point of maximal impulse (PMI) located at the fifth intercostal space, just medial to the midclavicular line [78] [64].

Radiation to the Axilla:

- The murmur may also radiate to the left axilla, as the blood flow is directed towards the left lateral chest wall [78] [64].

1.8 Mitral Valve Prolapse

Mitral Valve Prolapse (MVP) is a common valvular heart disorder characterized by the abnormal systolic displacement of part or all of the mitral valve leaflets into the left atrium during ventricular systole [10][33] (Figure 1.10).
The key features of mitral valve prolapse are:

1. Displacement of the mitral valve leaflets:
   - During ventricular systole, part or all of one or both mitral valve leaflets protrude or bulge back (prolapse) into the left atrium [10] [33].
   - This abnormal systolic displacement of the mitral valve leaflets is the hallmark of this condition [10] [33].
2. Mitral regurgitation:
   - Prolapse of the mitral valve leaflets can lead to incomplete closure of the mitral valve during systole, resulting in mitral regurgitation (backward flow of blood from the left ventricle into the left atrium) [10] [33].

- The severity of mitral regurgitation can range from mild to severe, depending on the degree of valve prolapse and leaflet displacement [10] [33].

3. Genetic and structural abnormalities:

   - Mitral valve prolapse is often associated with inherent structural and connective tissue abnormalities of the mitral valve apparatus, including thickened and redundant valve leaflets [10] [33].
   - In many cases, mitral valve prolapse has a genetic component, with certain inherited connective tissue disorders predisposing individuals to this condition [10] [33].

   Mitral valve prolapse is a common valvular heart disease, affecting approximately 2-3 % of the general population, and is more prevalent in women than men [10] [33] . It is an important condition to recognize and manage, as it can lead to significant complications, such as progressive mitral regurgitation, heart failure, and sudden cardiac death in some cases [10] [33].

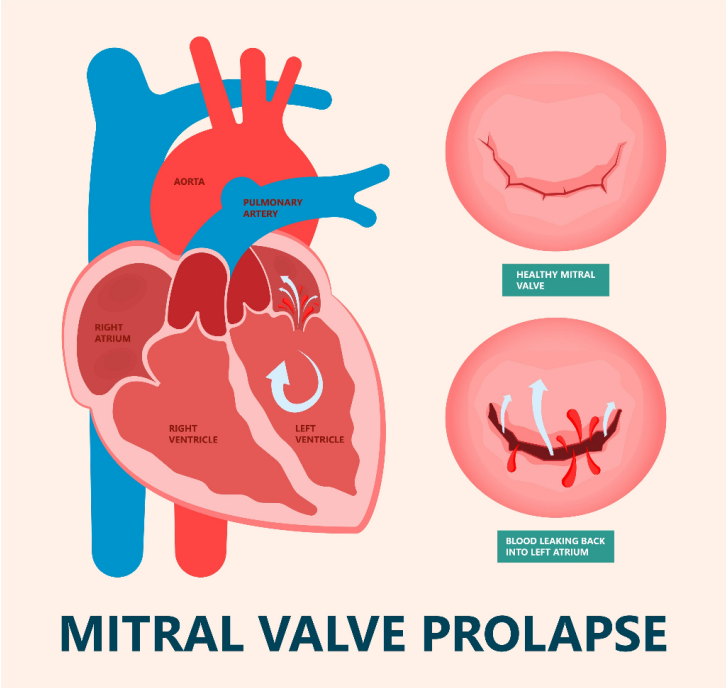

Figure 1.10: Mitral Valve Prolapse

Auscultation and Phonocardiography in Mitral Valve Prolapse MVP

Phonocardiography (PCG) can be used to detect and evaluate the presence of mitral valve prolapse (MVP) by analyzing the characteristics of the heart sounds and murmurs recorded on the chest wall.

1. Phonocardiographic Findings in Mitral Valve Prolapse:

   Mid-to-Late Systolic Click:

   - The primary PCG finding in mitral valve prolapse is the presence of a mid-to-late systolic click [18].
   - This click is caused by the sudden tensing of the prolapsing mitral valve leaflets [18] [78].

- The click typically occurs in mid-to-late systole, after the first heart sound (S1) (Figure 1.11) [18] [78].

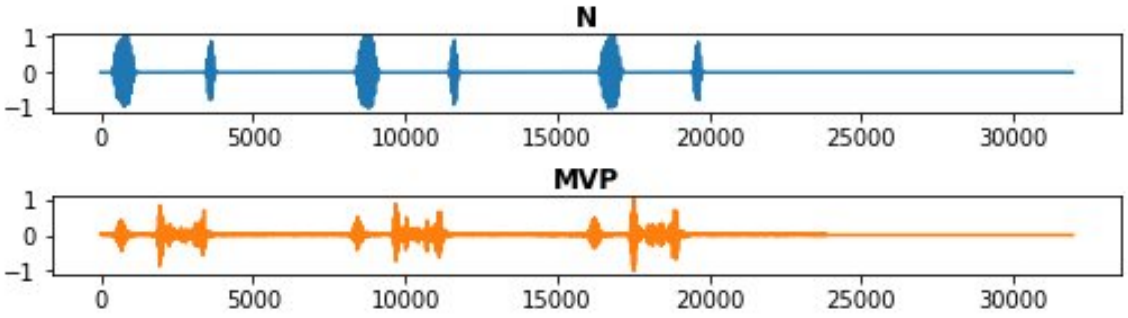

Figure 1.11: PCG Mitral Valve Prolapse

Mid-to-Late Systolic Murmur:

- In addition to the click, a mid-to-late systolic murmur may also be present on the PCG [18] [78].
- This murmur is caused by the turbulent flow of blood through the partially prolapsed mitral valve [18] [78].
- The murmur typically begins after the click and continues until the second heart sound (S2) [18] [78].

2. Murmur Location in Mitral Valve Prolapse:

   Cardiac Apex:

   - The mid-to-late systolic murmur associated with mitral valve prolapse is best heard at the cardiac apex, which is the point of maximal impulse (PMI) located at the fifth intercostal space, just medial to the midclavicular line [78] [20].

   By analyzing the presence of the mid-to-late systolic click and murmur, as well as their location on the PCG, clinicians can identify the presence of mitral valve prolapse. This information, combined with other clinical and echocardiographic findings, can help diagnose and manage this common valvular heart disorder.

1.9 Conclusion

In this chapter, a comprehensive overview of the importance of phonocardiogram (PCG) signals in the detection and analysis of various cardiac pathologies has been provided. The discussion began by introducing the heart and its essential functions, highlighting the significance of accurate diagnosis and monitoring of cardiac conditions.
Through the discussion of heart anatomy and functioning, a foundational understanding of the cardiovascular system and the origin of heart sounds was established. The section on cardiac auscultation further emphasized the role of PCG in augmenting the traditional stethoscope-based examination, allowing for more detailed analysis of heart sounds.

The in-depth exploration of the PCG signal, its characteristics, and the identification of the four key heart sounds provided valuable insights into the diagnostic potential of this non-invasive technique. By examining specific cardiac pathologies, such as aortic stenosis, mitral stenosis, mitral regurgitation, and mitral valve prolapse, changes in the PCG signal were demonstrated to serve as indicators of underlying cardiovascular conditions.

The knowledge gained from this chapter equips healthcare professionals with a deeper understanding of the PCG signal and its applications in the early detection, monitoring, and management of cardiac pathologies. By leveraging this technology, clinicians can make more informed decisions, leading to improved patient outcomes and enhanced quality of care.

As the field of cardiovascular diagnostics continues to evolve, the integration of PCG analysis into routine clinical practice holds great promise in advancing the understanding and management of various heart-related disorders. This chapter serves as a foundation for further research and development in this important area of healthcare.

CHAPTER 1

Bibliography

[1] Mohammed A Al-Hijji, Stephanie ElHajj, Abdallah El Sabbagh, Mohamad A Alkhouli, Juan Crestanello, Mackram F Eleid, Charanjit Rihal, and Mayra Guerrero. Temporal outcomes of transcatheter mitral valve replacement in native mitral valve disease with annular calcification. *Catheterization and Cardiovascular Interventions*, 98(4):E602–E609, 2021.

[2] J Ambrose, DG Pribnow, FD Giraud, KD Perkins, PB Anning, BD Prendergast, PA MacCarthy, AM Shah, DC Buss, MJ Lewis, et al. Cardiac failure. *Current Opinion in Cardiology*, 15:B95–B149, 2000.

[3] Amir Mohammad Amiri and Giuliano Armano. Heart sound analysis for diagnosis of heart diseases in newborns. *APCBEE procedia*, 7:109–116, 2013.

[4] Samit Ari and Goutam Saha. Classification of heart sounds using empirical mode decomposition based features. *International Journal of Medical Engineering and Informatics*, 1(1):91–108, 2008.

[5] Aníbal Arias, Rodolfo Pizarro, Pablo Oberti, Mariano Falconi, Luciano Lucas, Federico Sosa, Diego Funes, and Arturo Cagide. Prognostic value of left atrial volume in asymptomatic organic mitral regurgitation. *Journal of the American Society of Echocardiography*, 26(7):699–705, 2013.

[6] Sumair Aziz, Muhammad Umar Khan, Majed Alhaisoni, Tallha Akram, and Muhammad Altaf. Phonocardiogram signal processing for automatic diagnosis of congenital heart disorders through fusion of temporal and cepstral features. *Sensors*, 20(13):3790, 2020.

[7] Sepideh Babaei and Amir Geranmayeh. Heart sound reproduction based on neural network classification of cardiac valve disorders using wavelet transforms of pcg signals. *Computers in biology and medicine*, 39(1):8–15, 2009.

[8] Helmut Baumgartner, Volkmar Falk, Jeroen J Bax, Michele De Bonis, Christian Hamm, Per Johan Holm, Bernard Iung, Patrizio Lancellotti, Emmanuel Lansac, Daniel Rodriguez Munoz, et al. 2017 esc/eacts guidelines for the management of valvular heart disease. *Polish Heart Journal (Kardiologia Polska)*, 76(1):1–62, 2018.

[9] Lynn Bickley and Peter G Szilagyi. *Bates' guide to physical examination and history-taking*. Lippincott Williams & Wilkins, 2012.

[10] Robert O Bonow, Blase A Carabello, Kanu Chatterjee, Antonio C De Leon, David P Faxon, Michael D Freed, William H Gaasch, Bruce Whitney Lytle, Rick A Nishimura, Patrick T O'Gara, et al. Acc/aha 2006 guidelines for the management of patients with valvular heart disease: a report of the american college of cardiology/american heart association task force on practice guidelines (writing committee to revise the 1998 guidelines for the management of patients with valvular heart disease) developed in collaboration with the society of cardiovascular anesthesiologists endorsed by the society for cardiovascular angiography and interventions and the society of thoracic surgeons. *Journal of the American College of Cardiology*, 48(3):e1–e148, 2006.

[11] Robert O Bonow, Douglas L Mann, Douglas P Zipes, and Peter Libby. *Braunwald's heart disease e-book: A textbook of cardiovascular medicine*. Elsevier Health Sciences, 2011.

[12] Matias Brusco and Homer Nazeran. Digital phonocardiography: a pda-based approach. In *The 26th Annual International Conference of the IEEE Engineering in Medicine and Biology Society*, volume 1, pages 2299–2302. IEEE, 2004.

[13] Blase A Carabello. Modern management of mitral stenosis. *Circulation*, 112(3):432–437, 2005.

[14] Blase A Carabello and Walter J Paulus. Aortic stenosis. *The lancet*, 373(9667):956–966, 2009.

[15] Jonathan R Carapetis. Rheumatic heart disease in asia. *Circulation*, 118(25):2748–2753, 2008.

[16] Jonathan R Carapetis et al. Rheumatic heart disease in developing countries. *N Engl J Med*, 357(5):439–41, 2007.

[17] P Carvalho, P Gilt, J Henriques, L Eugénio, and M Antunes. Low complexity algorithm for heart sound segmentation using the variance fractal dimension. In *IEEE International Workshop on Intelligent Signal Processing, 2005.*, pages 194–199. IEEE, 2005.

[18] Melvin D Cheitlin, Joseph S Alpert, William F Armstrong, Gerard P Aurigemma, George A Beller, Fredrick Z Bierman, Thomas W Davidson, Jack L Davis, Pamela S Douglas, Linda D Gillam, et al. Acc/aha guidelines for the clinical application of echocardiography: a report of the american college of cardiology/american heart association task force on practice guidelines (committee on clinical application of echocardiography) developed in collaboration with the american society of echocardiography. *Circulation*, 95(6):1686–1744, 1997.

[19] Md Tanzil Hoque Chowdhury. *Application of Signal Processing and Deep Hybrid Learning in Phonocardiogram and Electrocardiogram Signals to Detect Early Stage Heart Diseases*. PhD thesis, Middle Tennessee State University, 2022.

[20] Simon Dagk, Selvyn Bleifer, Arthur Grishman, and Ephraim Donoso. Mitral stenosis: Auscultatory and phonocardiographic findings∗. *The American Journal of Cardiology*, 5(6):815–835, 1960.

[21] SM Debbal and A Meziane Tani. Heart sounds analysis and murmurs. *International Journal of Medical Engineering and Informatics*, 8(1):49–62, 2016.

[22] 2010 ACCF/AHA/AATS/ACR/ASA/SCA/SCAI/SIR/STS/SVM GUIDELINES FOR THE DIAGNOSIS, MANAGEMENT OF PATIENTS WITH THORACIC AORTIC DISEASE REPRESENTATIVE MEMBERS*, Loren F Hiratzka, Mark A Creager, Eric M Isselbacher, Lars G Svensson, 2014 AHA/ACC Guideline for the Management of Patients With Valvular Heart Disease Representative Members*, Rick A Nishimura, Robert O Bonow, Robert A Guyton, Thoralf M Sundt III, et al. Surgery for aortic dilatation in patients with bicuspid aortic valves: a statement of clarification

from the american college of cardiology/american heart association task force on clinical practice guidelines. *Circulation*, 133(7):680–686, 2016.

[23] Sean Dornbush and Andre E Turnquest. Physiology, heart sounds. 2019.

[24] Dale Dubin. *Rapid interpretation of EKG's: an interactive course*. Cover Publishing Company, 2000.

[25] Louis-Gilles Durand and Philippe Pibarot. Digital signal processing of the phonocardiogram: review of the most recent advancements. *Critical Reviews™ in biomedical engineering*, 23(3-4), 1995.

[26] Marc R Dweck, Nicholas A Boon, and David E Newby. Calcific aortic stenosis: a disease of the valve and the myocardium. *Journal of the American College of Cardiology*, 60(19):1854–1863, 2012.

[27] Roland Ebringer, Aubrey Pitt, and ST Anderson. Haemodynamic factors influencing opening snap interval in mitral stenosis. *British Heart Journal*, 32(3):350, 1970.

[28] Maurice Enriquez-Sarano, Cary W Akins, and Alec Vahanian. Mitral regurgitation. *The Lancet*, 373(9672):1382–1394, 2009.

[29] Volkmar Falk, Helmut Baumgartner, Jeroen J Bax, Michele De Bonis, Christian Hamm, Per Johan Holm, Bernard Iung, Patrizio Lancellotti, Emmanuel Lansac, Daniel Rodriguez Muñoz, et al. 2017 esc/eacts guidelines for the management of valvular heart disease. *European Journal of Cardio-Thoracic Surgery*, 52(4):616–664, 2017.

[30] Qian Fan, Qiang Xiao, Dezhong Qi, Bingqing Dong, and Xiaoqiang Zhou. Mechanics behaviors and materials investigation for prosthetic heart valves: Development and a critical review. *Available at SSRN 4870587*.

[31] Farzan Filsoufi, Sacha P Salzberg, and David H Adams. Current management of ischemic mitral regurgitation. *Mount Sinai Journal of Medicine*, 72(2), 2005.

[32] H Frank and MD Netter. *Atlas of human anatomy*. Elsevier Inc., 2019.

[33] Lisa A Freed, Daniel Levy, Robert A Levine, Martin G Larson, Jane C Evans, Deborah L Fuller, Birgitta Lehman, and Emelia J Benjamin. Prevalence and clinical outcome of mitral-valve prolapse. *New England Journal of Medicine*, 341(1):1–7, 1999.

[34] Rosario V Freeman and Catherine M Otto. Spectrum of calcific aortic valve disease: pathogenesis, disease progression, and treatment strategies. *Circulation*, 111(24):3316–3326, 2005.

[35] Valentin Fuster, Lars E Rydén, David S Cannom, Harry J Crijns, Anne B Curtis, Kenneth A Ellenbogen, Jonathan L Halperin, Jean-Yves Le Heuzey, G Neal Kay, James E Lowe, et al. Acc/aha/esc 2006 guidelines for the management of patients with atrial fibrillation: A report of the american college of cardiology/american heart association task force on practice guidelines and the european society of cardiology committee for practice guidelines (writing committee to revise the 2001 guidelines for the management of patients with atrial fibrillation): Developed in collaboration with the european heart rhythm association and the heart rhythm society. *Circulation*, 114(7):e257–e354, 2006.

[36] William Grossman. *Grossman's cardiac catheterization, angiography, and intervention*. Lippincott Williams & Wilkins, 2006.

[37] I Guler, FIRAT Hardalac, and FS Erol. Comparison of fft, ar and wavelet methods in transcranial doppler signal obtain from intracerebral vessels. In *2001 Conference Proceedings of the 23rd Annual International Conference of the IEEE Engineering in Medicine and Biology Society*, volume 2, pages 1832–1834. IEEE, 2001.

[38] Cota Navin Gupta, Ramaswamy Palaniappan, and Sundaram Swaminathan. Classification of homomorphic segmented phonocardiogram signals using grow and learn network. In *2005 IEEE Engineering in Medicine and Biology 27th Annual Conference*, pages 4251–4254. IEEE, 2006.

[39] Jose Luis Gutierrez-Bernal and José Luis Zamorano Gomez. Mitral valve. *Dynamic Echocardiography E-Book*, page 48, 2010.

[40] Arthur CMD Guyton. *Text book of medical physiology*. China, 2006.

[41] L Hatle, A Brubakk, A Tromsdal, and B Angelsen. Noninvasive assessment of pressure drop in mitral stenosis by doppler ultrasound. *Heart*, 40(2):131–140, 1978.

[42] Nada Fitrieyatul Hikmah, Achmad Arifin, Tri Arief Sardjono, and Eko Agus Suprayitno. A signal processing framework for multimodal cardiac analysis. In *2015 International Seminar on Intelligent Technology and Its Applications (ISITIA)*, pages 125–130. IEEE, 2015.

[43] Taku Inohara, Shun Kohsaka, John A Spertus, Frederick A Masoudi, John S Rumsfeld, Kevin F Kennedy, Tracy Y Wang, Kyohei Yamaji, Tetsuya Amano, and Masato Nakamura. Comparative trends in percutaneous coronary intervention in japan and the united states, 2013 to 2017. *Journal of the American College of Cardiology*, 76(11):1328–1340, 2020.

[44] Bernard Iung and Alec Vahanian. Epidemiology of valvular heart disease in the adult. *Nature Reviews Cardiology*, 8(3):162–172, 2011.

[45] Najarian Kayvan and Splinter Robert. Biomedical signal and image processing. *US, Taylor and Francis*, 2006.

[46] Nayad Kouras, Daoud Boutana, and Messaoud Benidir. Wavelet based segmentation and time-frequency caracterisation of some abnormal heart sound signals. In *2012 24th International Conference on Microelectronics (ICM)*, pages 1–4. IEEE, 2012.

[47] Beatrice Lattanzi. *Development of clinical grade Pulse Wave Velocity estimation equipment using MEMS microphones*. PhD thesis, Politecnico di Torino, 2018.

[48] Daniel Levy and Daniel Savage. Prevalence and clinical features of mitral valve prolapse. *American Heart Journal*, 113(5):1281–1290, 1987.

[49] Brian R Lindman, Marie-Annick Clavel, Patrick Mathieu, Bernard Iung, Patrizio Lancellotti, Catherine M Otto, and Philippe Pibarot. Calcific aortic stenosis. *Nature reviews Disease primers*, 2(1):1–28, 2016.

[50] Ilias Maglogiannis, Euripidis Loukis, Elias Zafiropoulos, and Antonis Stasis. Support vectors machine-based identification of heart valve diseases using heart sounds. *Computer methods and programs in biomedicine*, 95(1):47–61, 2009.

[51] Jaakko Malmivuo and Robert Plonsey. *Bioelectromagnetism: principles and applications of bioelectric and biomagnetic fields*. Oxford University Press, USA, 1995.

[52] Eloi Marijon, Mariana Mirabel, David S Celermajer, and Xavier Jouven. Rheumatic heart disease. *The Lancet*, 379(9819):953–964, 2012.

[53] Authors/Task Force Members, Alec Vahanian, Ottavio Alfieri, Felicita Andreotti, Manuel J Antunes, Gonzalo Barón-Esquivias, Helmut Baumgartner, Michael Andrew Borger, Thierry P Carrel, Michele De Bonis, et al. Guidelines on the management of valvular heart disease (version 2012) the joint task force on the management of valvular heart disease of the european society of cardiology (esc) and the european association for cardio-thoracic surgery (eacts). *European heart journal*, 33(19):2451–2496, 2012.

[54] Ann Nita Netto, Lizy Abraham, and Saji Philip. Hbnet: a blended ensemble model for the detection of cardiovascular anomalies using phonocardiogram. *Technology and Health Care*, (Preprint):1–21, 2024.

[55] Rick A Nishimura and Blase A Carabello. Hemodynamics in the cardiac catheterization laboratory of the 21st century. *Circulation*, 125(17):2138–2150, 2012.

[56] Rick A Nishimura, Catherine M Otto, Robert O Bonow, Blase A Carabello, John P Erwin III, Lee A Fleisher, Hani Jneid, Michael J Mack, Christopher J McLeod, Patrick T O'Gara, et al. 2017 aha/acc focused update of the 2014 aha/acc guideline for the management of patients with valvular heart disease: a report of the american college of cardiology/american heart association task force on clinical practice guidelines. *Circulation*, 135(25):e1159–e1195, 2017.

[57] Rick A Nishimura, Catherine M Otto, Robert O Bonow, Blase A Carabello, John P Erwin III, Robert A Guyton, Patrick T O'Gara, Carlos E Ruiz, Nikolaos J Skubas, Paul Sorajja, et al. 2014 aha/acc guideline for the management of patients with valvular heart disease: executive summary: a report of the american college of cardiology/american heart association task force on practice guidelines. *Circulation*, 129(23):2440–2492, 2014.

[58] Rick A Nishimura, Alec Vahanian, Mackram F Eleid, and Michael J Mack. Mitral valve disease—current management and future challenges. *The Lancet*, 387(10025):1324–1334, 2016.

[59] Tamer Ölmez and Zümray Dokur. Classification of heart sounds using an artificial neural network. *Pattern recognition letters*, 24(1-3):617–629, 2003.

[60] Catherine M Otto. *Textbook of clinical echocardiography*. Elsevier Health Sciences, 2013.

[61] Catherine M Otto, Rick A Nishimura, Robert O Bonow, Blase A Carabello, John P Erwin III, Federico Gentile, Hani Jneid, Eric V Krieger, Michael Mack, Christopher McLeod, et al. 2020 acc/aha guideline for the management of patients with valvular heart disease: executive summary: a report of the american college of cardiology/american heart association joint committee on clinical practice guidelines. *Journal of the American College of Cardiology*, 77(4):450–500, 2021.

[62] GÜLTEN Özgün and AYLA Açıkgöz. Sağlık teknikerliği öğrencilerinin su ayak izi ve su farkındalığı: Durum saptama çalışması.

[63] Sotiris A Pavlopoulos, Antonis CH Stasis, and Euripides N Loukis. A decision tree–based method for the differential diagnosis of aortic stenosis from mitral regurgitation using heart sounds. *Biomedical engineering online*, 3:1–15, 2004.

[64] James Peto et al. *The heart*. Yale University Press, 2007.

[65] Philippe Pibarot and Jean G Dumesnil. Prosthetic heart valves: selection of the optimal prosthesis and long-term management. *Circulation*, 119(7):1034–1048, 2009.

[66] Bernard D Prendergast and Pilar Tornos. Surgery for infective endocarditis: who and when? *Circulation*, 121(9):1141–1152, 2010.

[67] Teuku Muhammad Haykal Putra, Renan Sukmawan, Dwita Rian Desandri, Celly A Atmadikoesoemah, Elen Elen, and Manoefris Kasim. Left ventricular dimension after mitral valve surgery in rheumatic mitral stenosis: the impact of myocardial fibrosis. *The Journal of Tehran University Heart Center*, 15(3):119, 2020.

[68] Rangaraj M Rangayyan and Sridhar Krishnan. *Biomedical signal analysis*. John Wiley & Sons, 2024.

[69] Filippo Ravalli, Alexander P Kossar, Hiroo Takayama, Juan B Grau, and Giovanni Ferrari. Aortic valve regurgitation: pathophysiology and implications for surgical intervention in the era of tavr. *Structural Heart*, 4(2):87–98, 2020.

[70] P Sudhakar Reddy, Rosemarie Salerni, and James A Shaver. Normal and abnormal heart sounds in cardiac diagnosis: Part ii. diastolic sounds. *Current problems in Cardiology*, 10(4):1–55, 1985.

[71] Anne B Rossebø, Terje R Pedersen, Kurt Boman, Philippe Brudi, John B Chambers, Kenneth Egstrup, Eva Gerdts, Christa Gohlke-Bärwolf, Ingar Holme, Y Antero Kesäniemi, et al. Intensive lipid lowering with simvastatin and ezetimibe in aortic stenosis. *New England journal of medicine*, 359(13):1343–1356, 2008.

[72] Devrim Şahin. Heart sound segmentation using signal processing methods. Master's thesis, Bilkent Universitesi (Turkey), 2015.

[73] NAGUEH SF. Recommendations for the evaluation of left ventricular diastolic function by echocardiography. *J Am Soc Echocardiogr*, 22:107–133, 2009.

[74] Syed Shah, Gopinath Gnanasegaran, Jeanette Sundberg-Cohon, and John R Buscombe. The heart: Anatomy, physiology and exercise physiology. In *Integrating Cardiology for Nuclear Medicine Physicians: A Guide to Nuclear Medicine Physicians*, pages 3–22. Springer, 2009.

[75] Nicolas W Shammas, Rafat F Padaria, and Edmund P Coyne. Pericarditis, myocarditis, and other cardiomyopathies. *Primary Care: Clinics in Office Practice*, 40(1):213–236, 2013.

[76] Yun Hee Shon. *Analysis of the proteoglycan content in fresh and cryopreserved porcine cardiovascular tissues*. Old Dominion University and Eastern Virginia Medical School, 1993.

[77] Samuel C Siu and Candice K Silversides. Bicuspid aortic valve disease. *Journal of the American College of Cardiology*, 55(25):2789–2800, 2010.

[78] COST-EFFECTIVE DIAGNOSTIC Skill. 'cardiac auscultation: A cost-effective diagnostic skill. *Current Problems Cardiol*, 20(7):447–530, 1995.

[79] David B Springer, Lionel Tarassenko, and Gari D Clifford. Support vector machine hidden semi-markov model-based heart sound segmentation. In *Computing in Cardiology 2014*, pages 625–628. IEEE, 2014.

[80] A Ch Stasis, EN Loukis, SA Pavlopoulos, and D Koutsouris. Using decision tree algorithms as a basis for a heart sound diagnosis decision support system. In *4th International IEEE EMBS Special Topic Conference on Information Technology Applications in Biomedicine, 2003.*, pages 354–357. IEEE, 2003.

[81] Morton E Tavel. Cardiac auscultation: a glorious past—and it does have a future! *Circulation*, 113(9):1255–1259, 2006.

[82] Gerard J Tortora and Bryan H Derrickson. *Principles of anatomy and physiology*. John Wiley & Sons, 2018.

[83] Yaseen, Gui-Young Son, and Soonil Kwon. Classification of heart sound signal using multiple features. *Applied Sciences*, 8(12):2344, 2018.

CHAPTER 2

Predictive Modeling for Early Detection of Aortic stenosis Pathology using PCG Multifractal Detrended Fluctuation Analysis and SVM Classification

Contents

List of Figures

List of Tables

2.1 Introduction

Cardiovascular diseases pose a major health challenge worldwide, affecting a substantial portion of the population.The U.S. Cardiovascular Society reports that more than one in three adults are affected by heart-related issues. Furthermore, The Global Health Agency highlighted that Cardiovascular disorders caused approximately 17.9 million casualties in 2016, accounting for about 31% of all global fatalities.[51][53] [9].

To address this challenge, researchers have focused on the early detection and accurate diagnosis of Cardiovascular disorders using signal-processing methods. Notable progress has been made in cardiac research, especially in the analysis of phonocardiogram (PCG) signals. These innovative techniques offer improved accuracy and precision compared to conventional approaches such as frequency, energy, and entropy analysis.

Fractal dimension analysis of heart sounds has emerged as a promising avenue for distinguishing between pathological and healthy Cardiac acoustic signals . For example, Azmy et all [8], performed a contrastive analysis of individuals with aortic conditions, mitral valve pathologies(prolapse and regurgitation) , and also those who had undergone valvular surgery,revealing distinct variations in the fractal dimensions of their heart sounds. Likewise,Thomas et all [50] investigated the complex patterns of heart sounds, employing the Hurst exponent for effective classification and categorization.They also applied fractal decomposition to segment heart sounds and seriousness of mitral valve issues. In another study, researchers Gavrovska et all [23] conducted a comparative analysis using multifractal techniques to evaluate spectral patterns and the Hölder exponent among individuals with mitral valve prolapse and healthy controls, emphasizing the significance of sophisticated methods in enhancing our understanding of phonocardiographic signals. Recent studies by Guo et all [38] have also examined the multifractal characteristics of heart sounds in patients with heart failure with preserved ejection fraction (HFpEF) compared to healthy individuals, identifying eleven features that may serve as potential diagnostic markers.

This research employs a novel approach for analyzing phonocardiographic signals through multifractal detrended fluctuation analysis (MFDFA), which offers a fresh perspective on diagnosing cardiac conditions. MFDFA addresses the limitations of traditional fluctuation analysis methods and provides reliable findings in temporal evaluations. This technique has garnered notable attention across various fields, including financial market studies [42], brain activity research [22], seismic activity assessments [3], gait analysis [19], speech signal processing [48], heart rhythm variability [16], financial time series evaluations [54], DNA analysis [4], geoelectrical studies [45], characterization of aquatic sounds [14], protective strategies for DC-ring microgrids based on renewable energy sources [5], airflow measurements [46], and the study of infant cries in both typical and atypical conditions [36]. Moreover, MFDFA has been applied to studies focusing on carbonate platform bathymetry [39], the multifractal characteristics of avian vocalizations [11], and analyses of stability in micro milling processes [27], among various other fields.

2.2 Phonocardiogram Signal

A phonocardiogram (PCG) records the sounds produced during the Heart cycle phase.This signal consists of two primary forms of noise: hemodynamic noise and mechanical noise.Hemodynamic noise arises from the movement of blood within the chambers of the heart, whereas mechanical noise is generated by the movement of the heart valves as they open and close. These noise elements contribute to the distinct heart sounds and offer important insights for assessing cardiac health. The PCG signal reveals two prominent heart sounds: the first heart sound (S1) and the second heart sound (S2) (Fig 2.11).

The S1 sound corresponds to the closure of the atrioventricular (AV) valves, which separate the atria and ventricles. The S2 sound, on the other hand, is associated with the closure of the semilunar valves, which

regulate blood flow from the ventricles to the arteries.

2

2.2.1 Aortic narrowing

Aortic narrowing is evaluated by identifying murmurs occurring between the first heart sound (S1) and the second heart sound (S2) in the phonocardiographic (PCG) signal (see Figure 2.1).

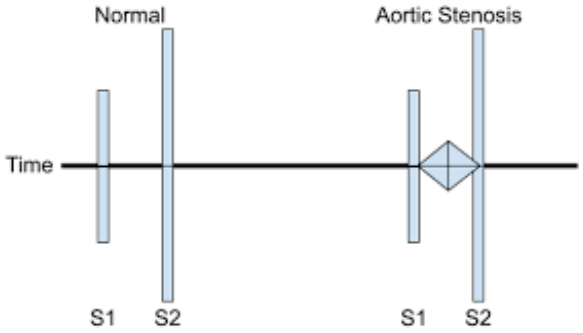

Figure 2.1: Aortic Stenosis

Previous studies [32] [26] have clearly shown that multifractal detrended fluctuation analysis (MFDFA), rooted in fractal geometry, provides a flexible framework for understanding a wide range of patterns and structures across various scientific fields. It thoroughly analyzes the multifractal properties of irregular patterns.

2.3 Fractal geometry

Historically, mathematics domain was largely shaped by Euclidean geometry, which concentrated on regular shapes like circles, triangles, squares, and rectangles.These structured geometric forms were the primary focus of mathematical study. However, the later introduction of geometries that do not conform to Euclidean principles, such as Riemannian and Poincaré geometries, which dealt with curved structures and forms, significantly broadened the field of mathematical investigation.These advancements eventually resulted in the formation of a new area of study known as fractal geometry, also referred to as natural geometry. The introduction of fractal geometry illuminated the irregular patterns observed in nature, showing that what appears chaotic or unpredictable often has an identifiable system or underlying framework. This insight has clarified why the behaviors of various organisms, despite seeming erratic, actually follow specific patterns or systems [17].

2.3.1 The Julia Set:

The **Julia set** is a fundamental concept in the field of fractal geometry, named after the French mathematician Gaston Julia. It is intricately related to the dynamics of complex functions and provides insight into the behavior of iterative processes in the complex plane [28].

2.3.2 Mathematical Foundation

Let x, y real variables , where the relationship between them is defined by the equation [Eq.(2.1)] :

$$y = x^2 + 1 \tag{2.1}$$

$(x, y) \in \mathbb{R}^2$
When $x = 0$, the corresponding y-value is:

$$y = 0^2 + 1 = 1$$

If x is then given the most recent y-value, it follows that:

$$y = 1^2 + 1 = 2$$
$$\downarrow$$
$$x = 1$$

$$y = 2^2 + 1 = 5$$
$$\downarrow$$
$$x = 2$$

$$y = 5^2 + 1 = 26$$
$$\downarrow$$
$$x = 5$$

$$y = 26^2 + 1 = 677$$
$$\downarrow$$
$$x = 26$$

$$y = n$$
$$\downarrow$$
$$x = n$$

$$y = n^2 + 1$$

This iterative process of substituting the last y-value back into x generates a peculiar, yet regular graphical representation.
By replacing the real variables x and y with complex numbers Z_n and Z_{n+1}, the equation becomes $Z_{n+1} = Z_n^2 + 1$, where $Z_n, Z_{n+1} \in \mathbb{C}$, and $\mathbb{C}$ represents the complex number system. The equation becomes [Eq. (2.2)]:

$$Z_{n+1} = Z_n^2 + 1 \tag{2.2}$$

where $Z = r + ri$, and $i = \sqrt{(-1)}$
If the constant 1 is replaced with an arbitrary complex number C, the equation takes the form:

$$Z_{n+1} = Z_n^2 + C$$

By selecting a specific complex value for C, such as $C = 0.3 + 0.5i$, and providing initial values for Z_n, the subsequent values of Z_{n+1} can be calculated according to the equation:

$$Z_{n+1} = Z_n^2 + 0.3 + 0.5i$$

To represent the infinite set of points generated by this iterative process, the implementation of a computer program is required. After the execution of this computational procedure and the subsequent visualization of the resulting values, the characteristic shape of the *Julia set* emerges, revealing the pro-

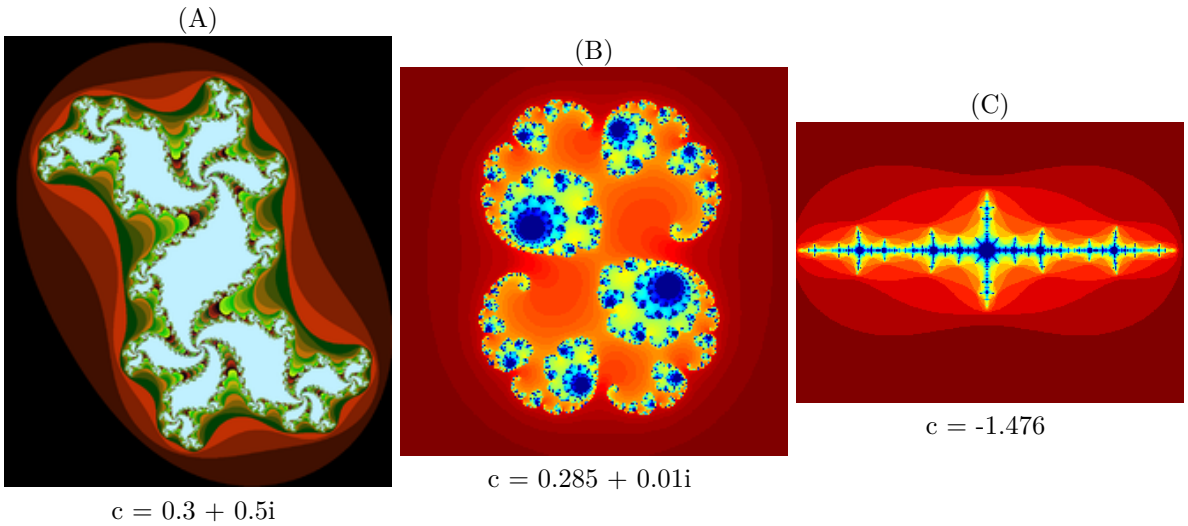

Figure 2.2: Various Values of c in the Julia set.

found mathematical insights that underpin this fundamental concept in the field of fractal geometry.The forms generated by the Julia set with different values of 'C' Illustrated in the Figure 2.2 .

2.3.3 Fractals and the Aesthetics of the Julia Set

The Julia set exhibits fractal properties, characterized by self-similarity and intricate detail at every level of magnification. These properties make it a subject of significant interest in the study of fractals and digital art, due to its visually complex and infinitely detailed structures.

2.3.4 Relationship with the Mandelbrot Set

The Julia set is closely related to the **Mandelbrot set**.The Mandelbrot set is utilized to determine the nature of the corresponding Julia set. If the parameter c lies within the Mandelbrot set, the associated Julia set is connected. Conversely, if c lies outside the Mandelbrot set, the associated Julia set is disconnected . In particular, the mathematician Benoit Mandelbrot concentrated on a particular portion of the Julia set,leading to the identification of the Mandelbrot set (Figure2.3), which can be expressed mathematically as [Eq.2.3]:

$$\begin{cases} Z_0 = 0 \\ Z_{n+1} = Z_n + C \end{cases} \tag{2.3}$$

Benoit Mandelbrot laid the groundwork for fractal studies [40, 17].In the context of fractal geometry, the Mandelbrot set can be characterized as a group of geometric figures formed by breaking down a larger shape into smaller replicas, each resembling a scaled-down version of the original (Figure 2.4).

2.3.5 Fractals Dimension

The dimensions in classical geometry are generally integers such as d=1, d=2, or d=3; however, in fractal geometry, dimensions can be irregular and fractional, as exemplified by the Von Koch curve[1] [7].
The construction of the Von Koch Curve follows a systematic iterative process [34].Initially, a line segment (step A) is divided into three equal parts, and the middle section is removed, leaving two smaller segments. An equilateral triangle is then added to the center, connecting the two remaining segments (as illustrated

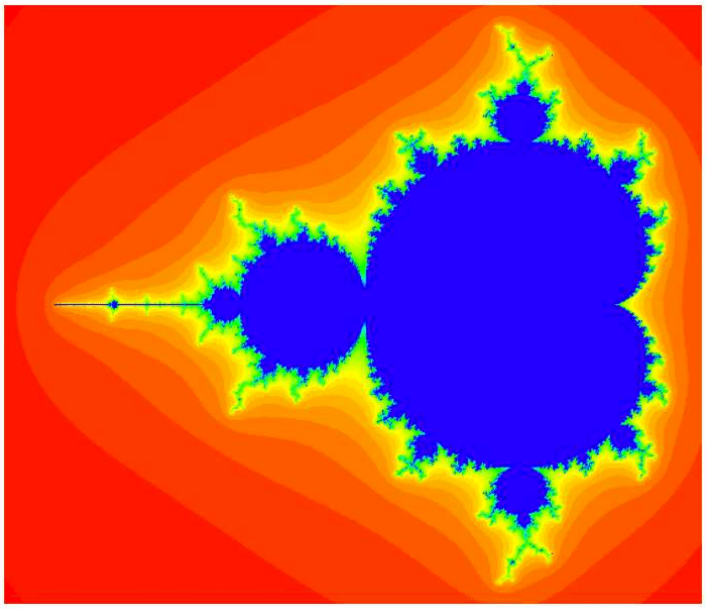

Figure 2.3: Mandelbrot set

in step B of the diagram). This same procedure is then applied to each of the newly created segments, and the process is repeated iteratively (as shown in steps C through E of the diagram).

The recursive methodology used to generate the Von Koch Curve can be further explored using a mathematical theorem that relates the number of identical shapes obtained after a given number of construction stages to the fractal dimension of the resulting pattern. Specifically, it has been observed that after three stages of the Von Koch Curve construction, four identical shapes are produced. This observation can be expressed as the equation $4 = 3^d$, where d represents the fractal dimension of the Von Koch Curve2.5. Solving this equation for the fractal dimension d yields [Eq.2.4]:

$$d = \frac{\ln(4)}{\ln(3)} \approx 1.26 \tag{2.4}$$

This calculated fractal dimension aligns with the empirically observed fractal dimension of the Von Koch Curve, which is approximately 1.26. This non-integer dimension is a hallmark of fractal geometry and highlights the inherent complexity and self-similarity exhibited by this geometric structure, which cannot be fully captured by traditional integer-based dimensional descriptions.

The same method can be used to determine the dimensions of other fractal shapes. For example, for Sierpinski's Triangle [35], it has been observed that after two stages of construction, three identical sections are obtained. This observation can be expressed as the equation $3 = 2^d$, where d represents the fractal dimension of Sierpinski's Triangle Figure 2.6 [44]. Solving this equation [Eq.2.5] yields [15]:

$$d = \frac{\ln(3)}{\ln(2)} \approx 1.58 \tag{2.5}$$

Similarly, for Sierpinski's Carpet [37], it has been observed that after three stages of construction, eight identical sections are obtained (Figure 2.7). This observation can be expressed as the equation $8 = 3^d$, where d represents the fractal dimension of Sierpinski's Carpet. Solving this equation yields [15](Figure 2.6:

$$d = \frac{\ln(8)}{\ln(3)} \approx 1.89 \tag{2.6}$$

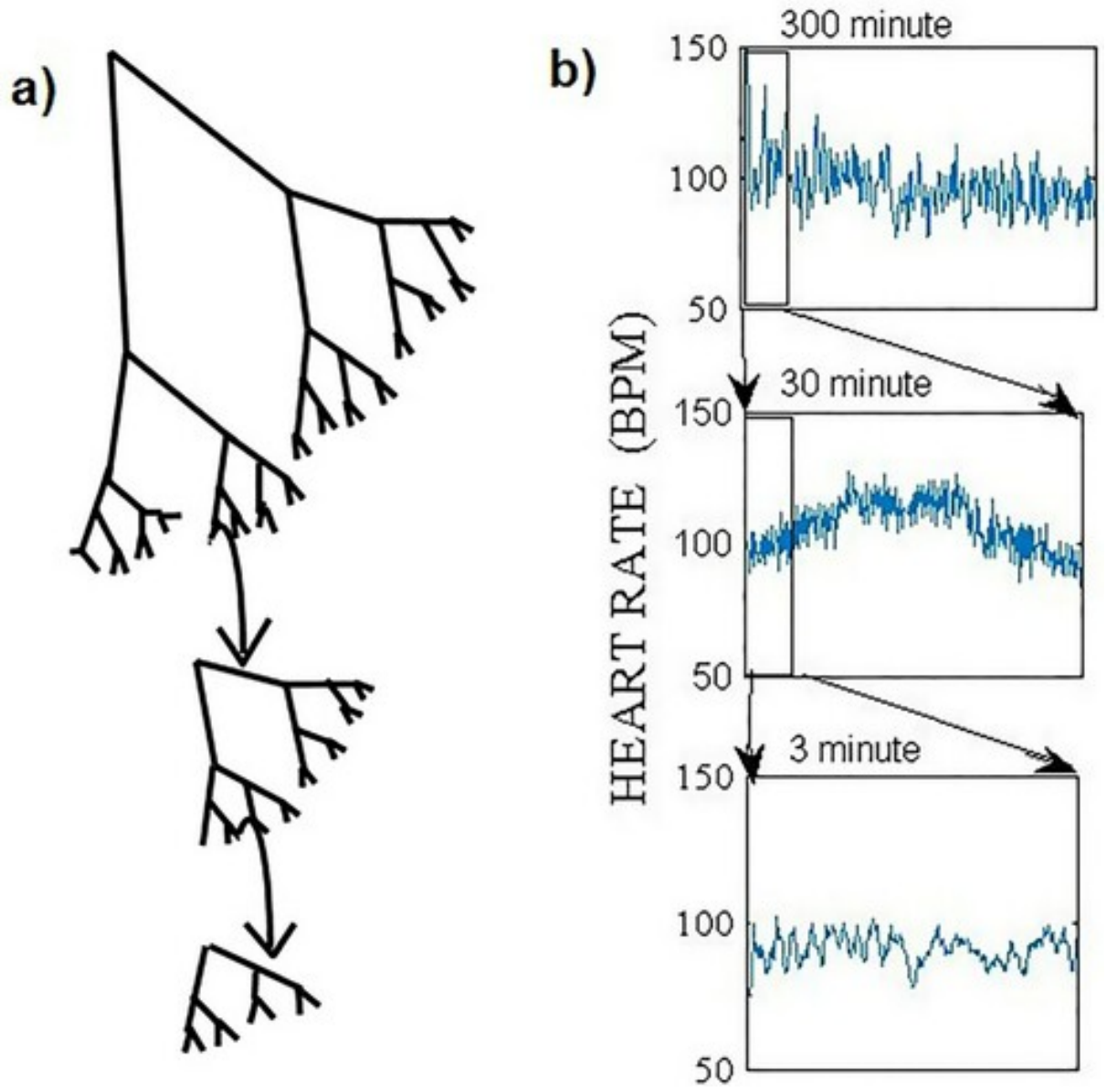

Figure 2.4. On the left side of the image, there is a fractal resembling a tree, featuring self-similar branches that reflect the overall structure in its components. On the right side, the image illustrates a fractal process akin to heart rate regulation, showcasing fluctuations that exhibit statistical self-similarity across various time scales.

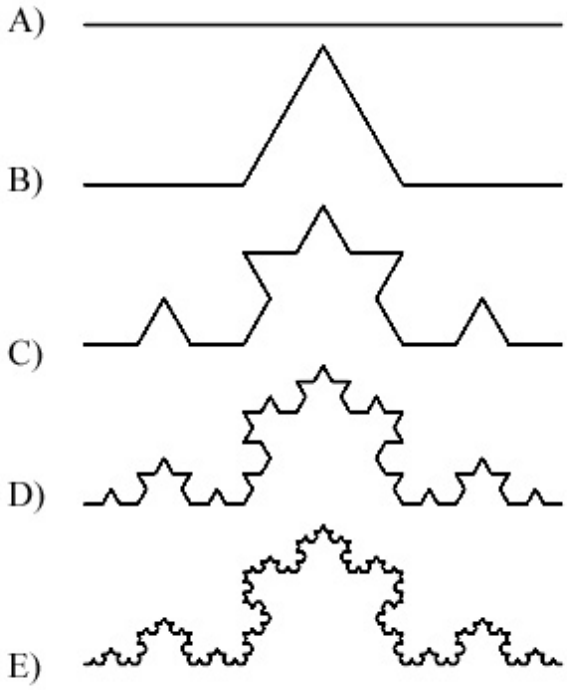

Figure 2.5. Von Koch Curve construction

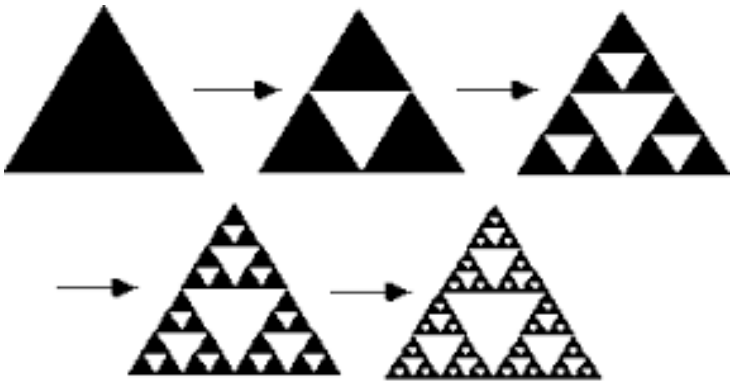

Figure 2.6. Construction of Sierpinski Triangle

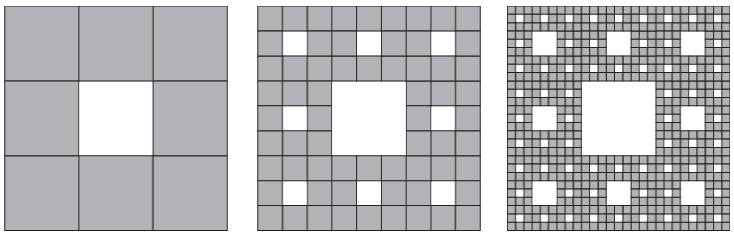

Figure 2.7. Construction of Sierpinski Carpet

The non-integer fractal dimensions observed in geometric structures such as the Von Koch Curve and Sierpinski's Triangle/Carpet highlight the inherent complexity and self-similarity exhibited by these objects. These fractal dimensions cannot be fully captured by traditional integer-based dimensional descriptions, as they reflect the highly irregular and intricate nature of these shapes.
The concept of non-integer fractal dimensions is closely related to the notion of Hausdorff dimension, which provides a more general mathematical framework for characterizing the dimensional properties of fractals and other highly irregular sets[21]. The Hausdorff dimension, denoted as d_H, is defined by the formula [Eq.2.7]:

$$d_H = \frac{\ln n}{\ln h} \tag{2.7}$$

where: * n represents the number of equal partitions or sections obtained after a given construction stage * h denotes the number of minimum divisions or scaling factor used to obtain the n sections
This formula captures the relationship between the scale-invariant, self-similar nature of fractals and their dimensional properties, allowing for a more nuanced and precise quantification of their complexity compared to traditional integer-based dimensions.
The Hausdorff dimension has become a fundamental tool in fractal geometry, dynamical systems theory, and other areas of mathematics and physics that deal with the analysis of complex, self-similar structures. It has proven invaluable for quantifying the dimensional properties of a wide range of natural and artificial phenomena, from coastlines and river networks to the structure of the universe and financial markets.

2.4 Support vector machine SVM

Support Vector Machine (SVM) is a supervised machine learning algorithm used primarily for classification task, although it can also be adapted for regression.

2.4.1 SVMs Hyperplane

SVMs work by finding the optimal hyperplane that separates different classes of data in the input space. The key idea behind SVMs is to identify the hyperplane that maximizes the margin, or distance, between the decision boundary and the closest data points from each class (Figure 2.8). SVMs are particularly effective at handling high-dimensional data and can learn complex, non-linear decision boundaries through the use of kernel functions. This makes them a powerful tool for a wide range of classification problems, from image recognition to text categorization [18].

2.4.2 kernel functions for SVM

The kernel of SVM algorithms consists of a set of mathematical functions. Input data is transformed into the desired form by the kernel according to its purpose. There are various kernel functions used by various SVM methods. Different types of these functions may exist. For instance, radial basis function (RBF), sigmoid, polynomial, linear, and nonlinear. Describe the vector, text, picture, graph, and sequence data kernel functions. The most common class of kernel functions are RBFs [33]. Due to its local and infinite response across the entire x-axis, the Gaussian radial basis function (RBF) kernel [Eq.2.8] [43]:

$$K(X_i, X_j) = \exp(-\gamma \|X_i - X_j\|^2) \tag{2.8}$$

for $\gamma > 0$; it is occasionally expressed as: $\gamma = 1/2\sigma^2$
Here,Xi, Xj represent the two inputs of the function K,where γ is the kernel parameter,and σ is the kernel argument. The role of these parameters is crucial in the performance of the SVM model:

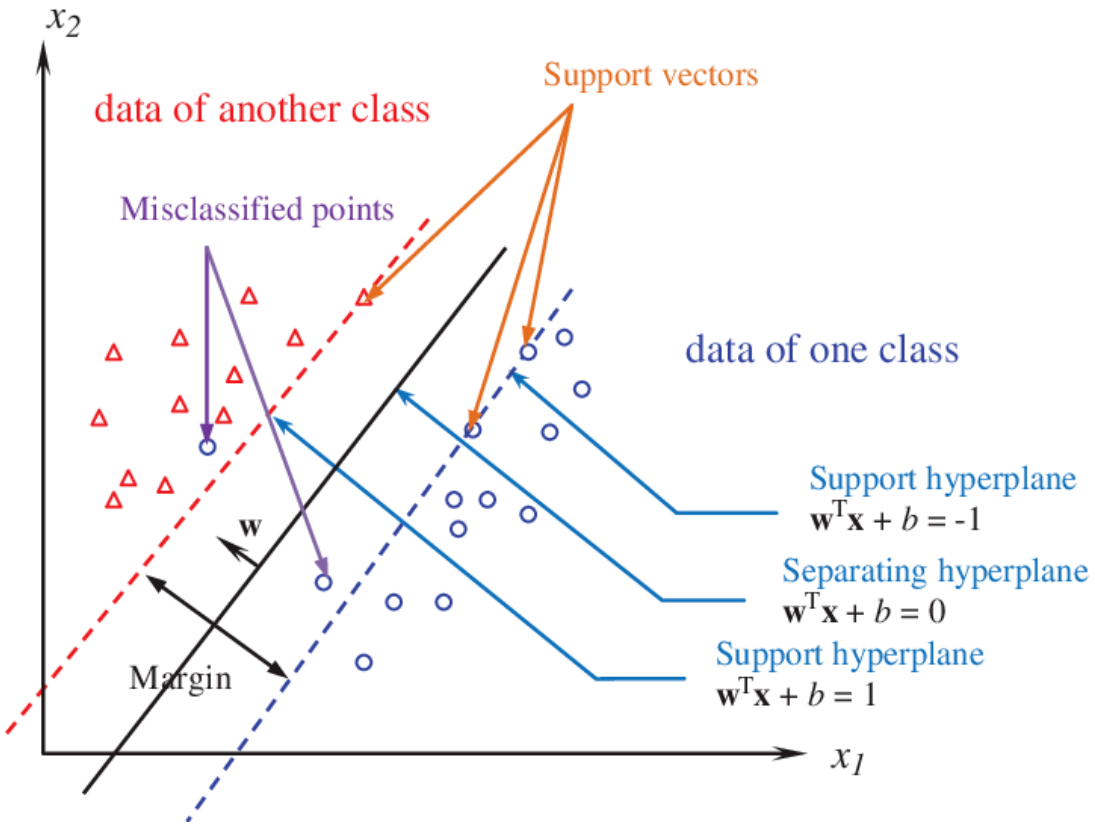

Figure 2.8. hyperplane diagram [31].

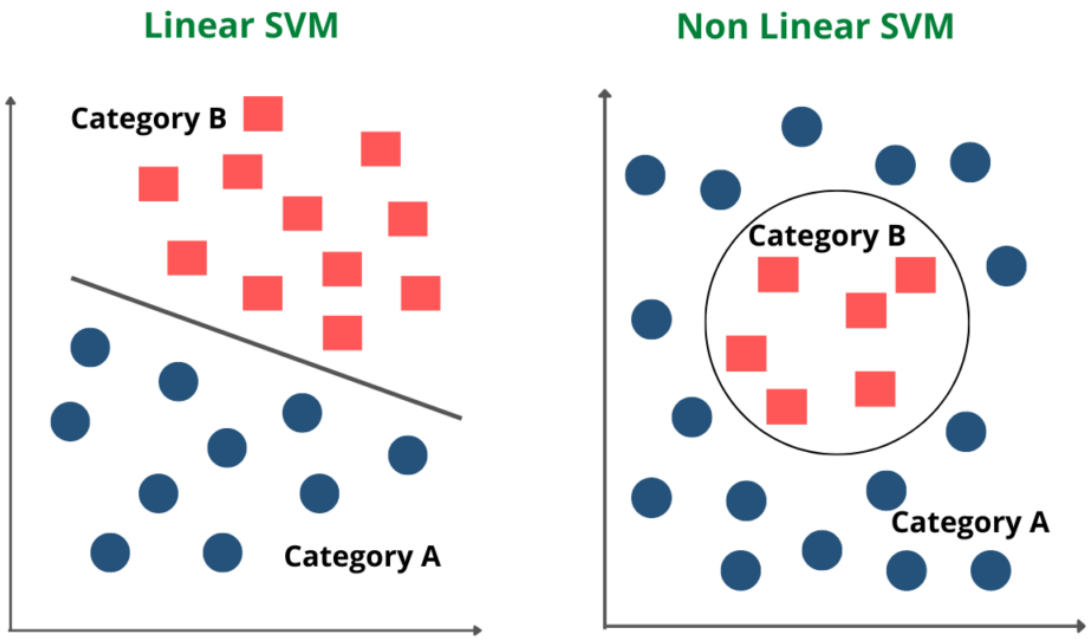

Figure 2.9. SVM classifiers for separating data in both linear and nonlinear contexts[12].

Gamma (γ): A small value of γ means the Gaussian has a large variance, resulting in a smooth decision boundary. This is good for datasets with minimal noise. A large value of γ means the Gaussian has a small variance, resulting in a complex decision boundary. This is good for datasets with a lot of noise, as it allows the SVM to fit the training data more closely. Choosing the right value of γ is important to avoid over-fitting or under-fitting the training data.
Sigma (σ): σ is the standard deviation of the Gaussian function in the RBF kernel. A larger σ leads to a wider Gaussian function, resulting in a smoother decision boundary. A smaller σ leads to a narrower Gaussian function, resulting in a more complex decision boundary. Tuning σ is important to balance the bias-variance tradeoff in the SVM model.

2.5 Classification

Classification is a core task in machine learning and data mining that involves categorizing data into predefined classes or labels based on their features. This process is vital across various domains, including finance, healthcare, marketing, and natural language processing. Understanding the different types of classification is essential for selecting the appropriate approach for a given problem.

2.5.1 Binary Classification

In the simplest case, SVMs are used for binary classification tasks, where the goal is to assign each input data point to one of two classes. The SVM algorithm works by finding the optimal hyperplane that separates the two classes with the largest possible margin.
Mathematically, the binary SVM optimization problem can be formulated as follows [Eq.2.9]:

$$\begin{aligned} &\text{Minimize: } (1/2)\|\mathbf{w}\|^2 \\ &\text{Subject to: } y_i(\mathbf{w}^\top \mathbf{x}_i + b) \geq 1, \text{ for all } i = 1, \ldots, n \end{aligned} \tag{2.9}$$

Where $\mathbf{w}$ is the normal vector to the hyperplane, b is the bias term, $\mathbf{x}_i$ are the input data points, and y_i are the corresponding class labels (+1 or -1).
The solution to this optimization problem yields the optimal hyperplane parameters $\mathbf{w}$ and b, which can then be used to classify new, unseen data points.

2.5.2 Multi-class Classification

While SVMs were originally designed for binary classification tasks, they can also be extended to handle multi-class problems, where the goal is to assign each input data point to one of more than two classes. There are several strategies for extending SVMs to multi-class classification, including:
1. One-versus-Rest (OvR): Train one SVM for each class, where the positive class is the current class and the negative class is the combination of all other classes.
2. One-versus-One (OvO): Train one SVM for each pair of classes, and use a voting scheme to determine the final prediction.
3. Multiclass SVM: Formulate the multi-class problem as a single optimization problem, rather than decomposing it into multiple binary subproblems.
The choice of the multi-class strategy depends on the specific problem at hand, the size and complexity of the dataset, and the desired trade-offs between computational efficiency and classification accuracy.
Overall, SVMs are a powerful and versatile machine learning technique that have been successfully applied to a wide range of classification problems in various domains. Their ability to handle high-dimensional

data and learn complex decision boundaries make them a go-to choice for many practitioners and researchers.

2.6 Method

The current research examines the identification of aortic valve narrowing condition through a collection of 200 healthy and 200 irregular Cardiac acoustic signals(physionet). The classification of these Cardiac acoustic signals was carried out by analyzing their multifractal and self-similar dynamics,utilizing software created by Espen A. F. Ihlen, which can be accessed at `www.ntnu.edu/inm/geri/software` [29].
Additionally, support vector machine (SVM) classification, executed in MATLAB R2022b, was used for further analysis and classification. The comprehensive methodology and sequence of steps followed in this research are depicted in (Figure 2.10),which visually represents the entire analytical process. The following sections of the manuscript will provide a detailed explanation of each step in the methodology, highlighting the importance of each element within the framework of this study.

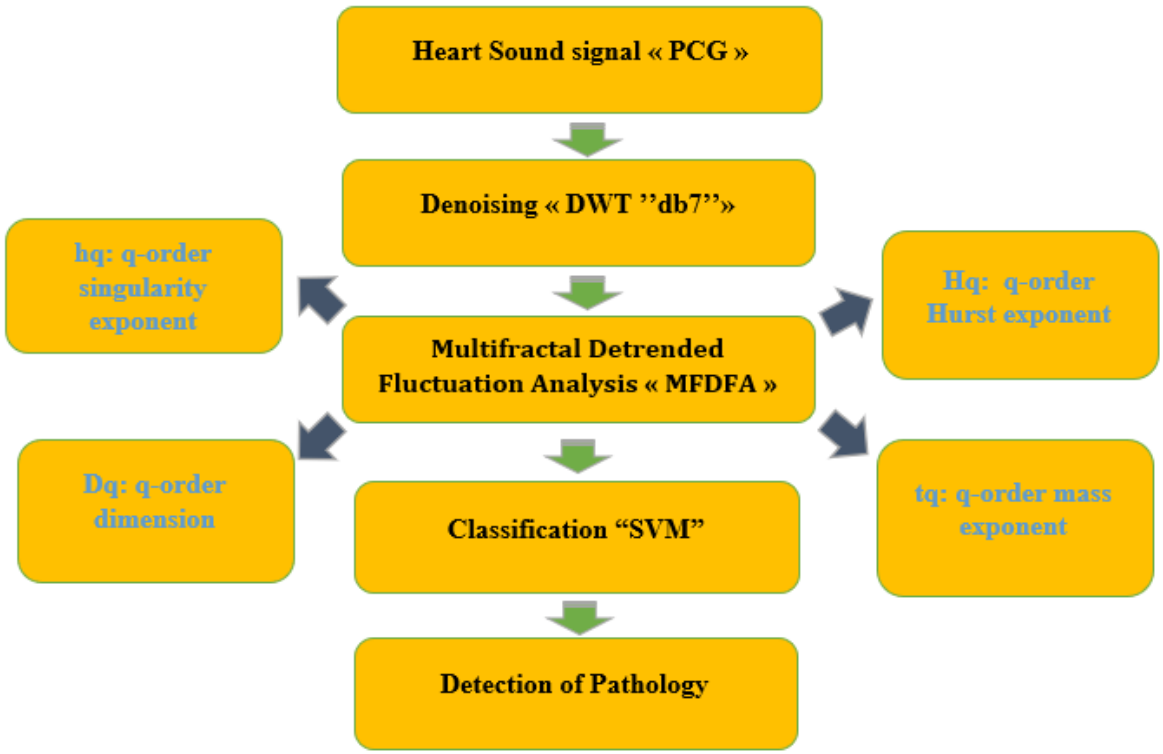

Figure 2.10. Diagram illustrating the techniques for analyzing and classifying Phonocardiogram signals.

2.6.1 Denoising

The application of the discrete wavelet transform (DWT) is a critical signal processing technique for enhancing phonocardiogram (PCG) recordings.The Discrete Wavelet Transform (DWT) breaks down the acquired signal into separate frequency bands, allowing for the detection and elimination of unwanted noise and artifacts while maintaining the essential features of the PCG waveforms. This denoising process is of utmost importance in ensuring the accuracy of multifractal detrended fluctuation analysis (MFDFA) by reducing potential inaccuracies in the estimation of model parameters and averting misunderstandings between diseased and healthy PCG signal scenarios.

The meticulous application of DWT-based denoising is a crucial pre-processing step that enables the reliable extraction of the underlying multifractal and self-similar dynamics from the PCG signals, which form the basis for the subsequent classification analysis presented in this study.

2.6.2 Utilization of MATLAB for the analysis PCG signals through MFDFA1 and MFDFA2

a. **A crucial initial requirement for optimal performance of MFDFA1 and MFDFA2 is that the signal must resemble a noise-like time series**

The dynamics of signals often fall into one of two main categories: a random walk process or a noise-like temporal behavior.

The differentiation between random walk and noise-like time series can present significant visual challenges. To mitigate this issue, Eke et al. (2002) proposed the computation of the Hurst exponent utilizing detrended fluctuation analysis (DFA). Their results indicated that when the Hurst exponent H lies within the interval of 0.2 to 0.8, the time series can be classified as noisy. Conversely, if the Hurst exponent H falls ranging from 1.2 to 1.8, the temporal data necessitates preprocessing prior to the application of MFDFA1 and MFDFA2. Table 2.1 summarizes the various classifications of the Hurst exponent derived from monofractal DFA, in addition to the requisite conversion steps that should be undertaken pertaining to biomedical temporal data before employing MFDFA1 and MFDFA2.

To mitigate significant flaws in the multifractal frequency field and address the challenge of approaching zero in the logarithmic calculations of log (Fq) and log (RMS), it is essential to ascertain that local fluctuations, measured by the root mean square (RMS), across MFDFA1 and MFDFA2 are not negligible. This precaution is vital for preserving the reliability of the computations and minimizing the risk of inaccuracies in the multifractal analysis.

The scale of the temporal data demonstrates consistency, signifying a direct correlation among log (scale) and log (Fq). This relationship indicates that as the scale of the temporal data either grows or diminishes, the associated values of Fq exhibit a stable pattern. The straight association across these logarithmic scales is a fundamental Attribute in the assessment of the temporal data, facilitating the recognition of of intrinsic patterns and actions across diverse scales.

Hurst exponent	Conversion
<0.2	Signal = cumsum(X - mean(X))
0.2-0.8	No conversion
0.8-1.2	No conversion
1.2-1.8	Signal = diff(X)
>1.8	Signal = diff(diff(X))

Table 2.1: Biomedical Time Series Data Conversion (Noble 2006)

b. **The parameters of input values scale, q, and m**

b.1 **Scale**

In the context of Multifractal Detrended Fluctuation Analysis (MFDFA) of PCG (Phonocardiogram) signals, the ”scale” parameter refers to the size of the segments into which the signal is divided during the analysis. series [41].

- The scale parameter, typically denoted as ’**s**’, represents the length of the non-overlapping segments into which the PCG signal is divided.

- The MFDFA algorithm calculates the fluctuation function 'F(s,q)' for each segment size '**s**', which is then used to determine D(h) 'the multifractal spectrum ' and H(q) 'the generalized Hurst exponents'.

- The choice of the scale parameter 's' is an important step in the MFDFA analysis, as it can significantly influence the multifractal properties of the PCG signal.

- The scale parameter should be determined in alignment with the features of the PCG signal and the objectives of the research. Typically, the scale parameter is selected to encompass a variety of segment sizes, ranging from the smallest meaningful segment to the largest size that still allows for reliable statistical estimates [47].

- A common approach is to use a logarithmically spaced range of scale values, such as **s = [4, 8, 16, 32, 64, 128, 256]**. This allows for the exploration of the signal's multifractal properties across different scales.

- The minimum scale '**s**' should be large enough to capture the smallest meaningful fluctuations in the PCG signal, while the maximum scale should be small enough to ensure that the segments still contain enough data points for reliable statistical analysis.

- The choice of the scale parameter range can also be informed by the signal's characteristics, such as the sampling rate, the dominant frequencies, and the expected fractal structure.

By analyzing the PCG signal across a range of scales, the MFDFA method can reveal the multifractal properties of the signal at different levels of detail, providing a more comprehensive understanding of the underlying physiological processes.

b.2 q order

The concept of the q-order is fundamental in multifractal analysis, as it allows for the weighting of periods with both large and small variations within the PCG signal. It is essential to employ a range of positive and negative q-orders in the analysis to fully capture the multifractal nature of the data [30]. Incorporating both positive and negative q-orders enables the detection and characterization of the distinct scaling properties associated with the regions of the PCG signal exhibiting large fluctuations as well as those exhibiting smaller variations. This comprehensive approach to the selection of q-orders is crucial for obtaining a robust and meaningful multifractal description of the underlying dynamics inherent in the PCG signal .

b.3 Trend order m

The selection of the detrending polynomial order m or trend order in the Multifractal Detrended Fluctuation Analysis (MFDFA) algorithm is a crucial parameter that can influence the multifractal analysis of the PCG signal. By employing different values of m, such as m=1 and m=2, the analysis was able to investigate the sensitivity of the multifractal properties to the detrending polynomial order.

For the case of m=1 (linear detrending) MFDFA1, the first-order polynomial was used to detrend the PCG signal segments, removing any linear trends or non-stationarities in the signal. The multifractal spectrum D(h) and the generalized Hurst exponents H(q) were then computed based on the detrended signal segments. The linear detrending is generally suitable for capturing the enduring correlations and fractal attributes of the PCG signal.

For the case of m=2 (quadratic detrending) MAFDFA2, the second-order polynomial was used to detrend the PCG signal segments, removing any quadratic trends or more complex non-stationarities in the signal.the multifractal spectrum D(h) and H(q) the generalized

Hurst exponents were computed based on the detrended signal segments. The quadratic detrending can help remove more complex trends, providing a deeper understanding of the multifractal properties of the PCG signal[41].

In the examination of the phonocardiogram (PCG) signal, the Multifractal Detrended Fluctuation Analysis (MFDFA) technique was employed, specifically utilizing the MFDFA1 and MFDFA2 functions available in MATLAB. This well-recognized algorithm enabled a thorough multifractal assessment of the PCG signal. MFDFA is a commonly used approach for measuring the self-similar and irregular properties of the phonocardiogram signal (x) using multifractal characterization. The Multifractal Detrended Fluctuation Analysis (MFDFA) involves multiple distinct phases [47]:

1. Initial Phase:
   - Computation of the integral representation of the PCG signal, frequently termed the signal's "trajectory" or "profile" [Eq.2.10] :

$$y_k = \sum_{i=1}^{k} [x_i - \overline{x}] \tag{2.10}$$

   Where $\overline{x}$ denotes the mean of x computed across the series. It is essential to emphasize that the incorporation of $\overline{x}$ into the equation lacks effect on the ultimate worth of $F[n]$.

2. Subsequent Phase:
   - The derived integral representation $y(k)$ is partitioned into a series of non-overlapping intervals, each of uniform length s, with the total number of intervals represented as N_s. The count of contiguous intervals is established by partitioning the length of the integral representation N (Signal length) by the segment length s and approximating the resulting value to the nearest integer through the use of the "int" function [49] .To guarantee that all data is utilized, this windowing procedure is executed from the opposite end of the integral representation [10] The choice of appropriate segment lengths is essential for the accurate determination of the fluctuation function. The shortest segment The length must be ample enough large to to prevent overfitting, whereas the longest fragment length must be kept small enough to ensure a sufficient number of intervals for the computation of the fluctuation function [Eq.2.11]:

$$F[n] = \sqrt{\frac{1}{N} \sum_{k=1}^{N} (y[k] - \bar{y}[k]_n)^2} \tag{2.11}$$

   where $\bar{y}[k]_n$ represents the local trend of the integral representation $y(k)$ within each segment of length n.

3. Tertiary Phase:

   The local trend determination for every segment of length 2Ns "The fluctuation $F^2(s, v)$":
   - for the procedure in the forward direction [Eq.2.12]:

$$F^2(s, v)_f = \frac{1}{s} \sum_{i=1}^{s} [y\{(v-1)s + i\} - y_v(i)]^2 \tag{2.12}$$

   And $v = 1.....N_s$

– for the procedure in the backward direction [Eq.2.13]:

$$F^2(s,v)_b = \frac{1}{s}\sum_{i=1}^{s}[y\{(N-(v-N_s)s+i\}) - y_v(i)]^2 \tag{2.13}$$

Where v is permitted to assume values within the range of $N_s + 1$ to $2N_s$

To perform a comprehensive analysis, the standard detrended fluctuation analysis (DFA) is carried out by assessing the range of segment indices $\{T = N_s + 1, N_s + 2, ..., 2N_s\}$ [20][25]. This specified range guarantees that all segments within the PCG signal are included in the computation of local trends.

By deriving the local trends through these methodologies, we can quantify the fluctuations present in each segment, thereby enhancing our understanding of the underlying dynamics and patterns inherent in the PCG signal.

4. Fourth Phase:
   – To derive the fluctuation function, an average is computed across all segments (from v = 1 to 2Ns) to derive the q^{th} order fluctuation function [Eq.2.14]:

$$F_q(s) = \left[\frac{1}{2N_s}\sum_{v=1}^{2N_s}\left\{F^2(s,v)^{\frac{q}{2}}\right\}\right]^{\frac{1}{q}} \tag{2.14}$$

   In this context, q denotes the fluctuation criterion, which can assume any actual worth, thereby allowing for a focused analysis on a range of global fluctuation magnitudes.

5. Fifth Phase:
   – To examine the scaling characteristics of the fluctuation functions, the power-law scaling function is utilized to investigate the log-log relationship between $Fq(s)$ and s for each q value. This relationship is represented by the following approximation [Eq.2.15]:

$$F_q(s) \sim s^{h(q)} \tag{2.15}$$

6. Sixth Phase:
   – This phase focuses on estimating the multifractal frequency field through the analysis of scaling exponents obtained from the q-order moments of the PCG signal.
   The multifractal spectrum offers important insights into the allocation of these scaling exponents, highlighting the signal's multifractal characteristics and its behavior across various time scales.

This thorough methodological framework enabled the extraction of 16 parameters from the PCG signal, which were later classified using Support Vector Machine (SVM) techniques.

2.6.3 Classification

The distinction between healthy and pathological PCG signals, especially in instances of aortic narrowing, can be proficiently accomplished using the SVM model with a Gaussian RBF kernel.
The classification process involves the following procedures:

1. Data preprocessing:
    - A collection of 400 signals, each with 16 attributes, was compiled. These attributes represent different characteristics derived from the signals.
2. Data division for training and testing:
    - The dataset was arbitrarily partitioned into training and testing sets. The training set was used to develop the SVM model, while the testing set was reserved for performance evaluation.
3. Feature selection:
    - A technique such as Sequential Feature Selection was used to identify the most significant subset of features. This step aimed to reduce dimensionality and enhance the SVM model's ability to distinguish between different classes.
4. SVM model optimization:
    - The SVM model was developed utilizing the chosen features from the training dataset. The algorithm identified the fundamental patterns and connections within the data to create the decision boundary that distinguishes the Categories.
5. Model validation:
    - The performance of the developed SVM model was assessed using the test dataset. The evaluation involved comparing the predicted classifications with the actual labels of the test samples. Standard metrics, including accuracy and precision, were used to quantify the effectiveness of the model's categorization.

Employing the SVM technique for this classification challenge allowed for the successful sorting of signals into distinct categories based on their attributes. The careful selection of relevant features, paired with the development of the SVM model, ensured accurate categorization, as demonstrated by the assessment outcomes.

2.7 Results

2.7.1 Signal enhancement

The process of enhancing the PCG signal through Discrete Wavelet Transform (DWT) using the db7 minimax wavelet over 8 levels demonstrates how DWT can significantly improve the credibility and accuracy of subsequent assessments, especially in the detection and profiling of heart-related disorders in PCG signals. This effectiveness is illustrated in the comparative analysis found in Figures 2.11 and 2.12, which is essential for increasing the consistency and precision of future analytical methods. In Figure 2.11, a healthy PCG signal is depicted, revealing key components associated with the closure of the cardiac valves, commonly known as the first and second heart sounds, which are typical indicators of a well-functioning cardiovascular system.

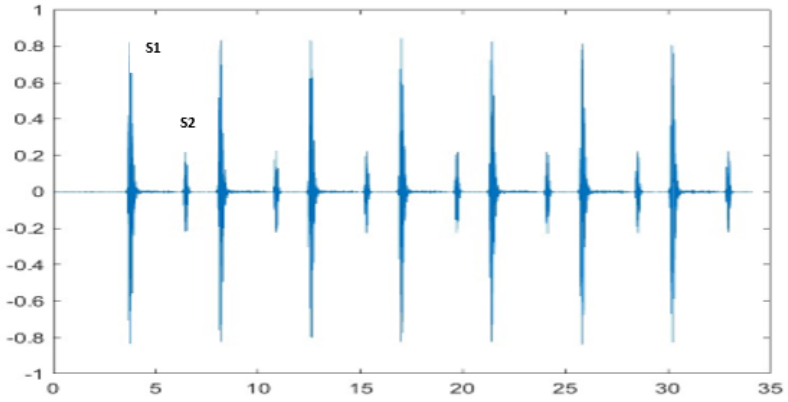

Figure 2.11. Filtering of normal phonocardiogram signal

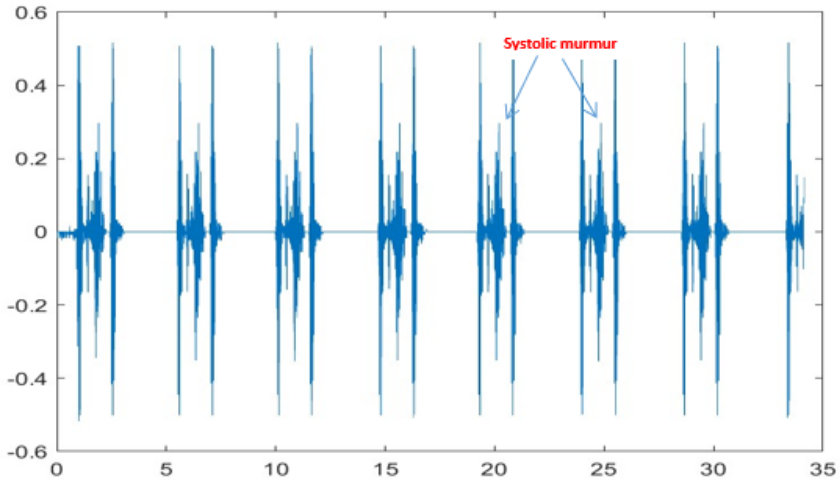

Figure 2.12: Filtering of aortic stenosis phonocardiogram signal

Conversely, (Figure 2.12) presents a PCG signal that points to aortic stenosis. Here, a systolic murmur occurring between S1 and S2 signifies a pathological issue with the aortic valve. This evident deviation emphasizes the effectiveness of DWT in improving both the reliability and accuracy of subsequent analyses, as well as in the detection and characterization of cardiovascular conditions within PCG signals.

2.7.2 Study of PCG signal with MFDFA

Prior to applying Multifractal Detrended Fluctuation Analysis (MFDFA), we computed the Hurst exponent of the heart sound using Detrended Fluctuation Analysis (DFA), as shown in (Figure 2.13, Figure 2.14 ,Figure 2.15, Figure 2.16,Figure 2.17, Figure 2.18) The results indicated a Hurst exponent (H) ranging from 0.8 to 1.2 (see Table 2.2) . This fractal analysis of the phonocardiogram signal enabled the extraction of several key parameters listed in (Table 2.3) that are crucial for the detection of aortic stenosis:

Number	Cases	Hurst exponent
200	Normal PCG Signal	0.8 - 1.2
200	Aortic Stenosis	0.7

Table 2.2: Calculation of DFA Hurst Exponent

Parameters	Normal PCG	Aortic stenosis
Ht (max)	6.4161	0.90551
Ht (mode)	1.8271	0.6944
Ht (min)	1.6062	0.13043
tq(max)	1.3706	−0.99724
tq(mode)	−1.3249	−1.1124
tq(min)	−4.6359	−2.9683
RMS	0.0834	0.0193
Hq(max)	1.4544	0.78732
Hq(mode)	1.2998	0.44965
Hq(min)	1.1853	0.0013801
Dq(max)	0.99573	0.97768
Dq(mode)	0.85518	0.72654
Dq(min)	0.6218	0.72552
hq(max)	1.60565	0.8967
hq(mode)	1.3169	0.53894
hq(min)	1.1129	−0.13586

Table 2.3: Attributes of normal versus abnormal PCG signal

The approach employed involves the extraction of 16 unique parameters from the phonocardiogram (PCG) signal, which are then classified using Support Vector Machine (SVM) techniques. The parameters are defined as follows:

- **Peak Values:**
  - **Ht (max), Hq (max), tq (max), Dq (max), hq (max):** Represents the highest amplitude recorded, the peak value of the generalized Hurst exponent characterizing sustained correlations, the longest duration observed between heart sounds, the peak value of the generalized dimension indicating scaling properties, and the peak value of the singularity exponent characterizing localized fluctuations, respectively.
- **Mode Values:**
  - **Ht (mode), Hq (mode), tq (mode), Dq (mode), hq (mode):** Denotes the predominant amplitude, the most frequently observed fractal property, the most common interval between heart sounds, the most common scaling property, and the most frequently occurring irregularity, respectively.

- **Minimum Values:**
  - **Ht (min), Hq (min), tq (min), Dq (min), hq (min):** Indicates the minimum amplitude detected, the least fractal characteristic, the shortest interval recorded, the least scaling characteristic observed, and the lowest value of the singularity exponent, respectively.
- **RMS:** The root mean square value of the acoustic cardiac signal serves as an indicator of the total energy or amplitude in the signal.

The 16 parameters extracted from the phonocardiogram (PCG) signal encapsulate diverse characteristics, including amplitude distribution, duration distribution, energy levels, fractal properties, scaling characteristics, and local irregularities. These metrics provide crucial insights into the dynamics and properties of cardiac signals.
Estimating multifractal characteristics—specifically the Hurst exponent, scaling exponent, and root mean square (RMS) values—plays a crucial role in differentiating normal cardiac function from aortic stenosis. Notably, the parameters associated with aortic stenosis tend to be lower than those seen in healthy individuals, indicating a diminished multifractal nature in these cases. This change is linked to the mechanical alterations in the myocardium that occur with aortic stenosis compared to normal heart function. The multifractal spectrum, obtained from local fluctuations and probability distributions, illustrates a narrower range of healthy behaviors relative to disease conditions, which display two distinct peaks, as shown in Figure 2.13 and Figure 2.17 We leveraged the multifractal characteristics of heart sounds

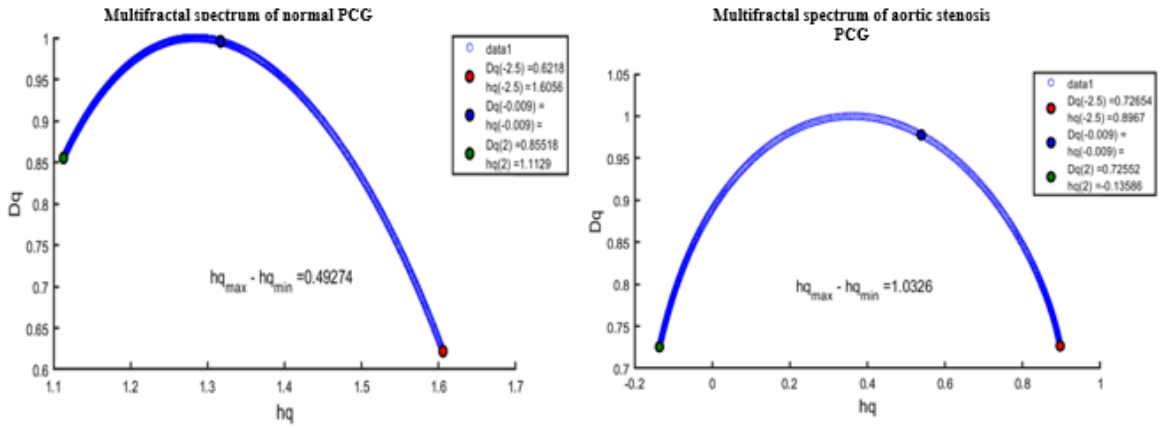

Figure 2.13. Multifractal Spectrum and q-Order RMS Calculation for Normal Conditions and Aortic Stenosis

[29]to facilitate the detection and diagnosis of heart diseases through Multifractal Detrended Fluctuation Analysis (MFDFA), resulting in several key outcomes:
(1) Based on multifractal theory, a lower Hurst exponent (H) in aortic stenosis indicates a more pronounced anti-correlation compared to normal states[50] [52].
(2) The variation in the generalized Hurst exponent highlights the differences in long-range correlations between large and small fluctuations. [38].
(3) The parameters h(qmin) and h(qmax) reflect the attenuation rates of minimum and maximum fluctuations; their lower values signify rougher fluctuations, which are indicative of aortic stenosis pathology [13].
(4) The myocardial perfusion status in patients with aortic stenosis is generally worse than that of healthy individuals.
(5) There is a noticeable reduction in the multifractal intensity of the PCG signal in patients with aortic stenosis.

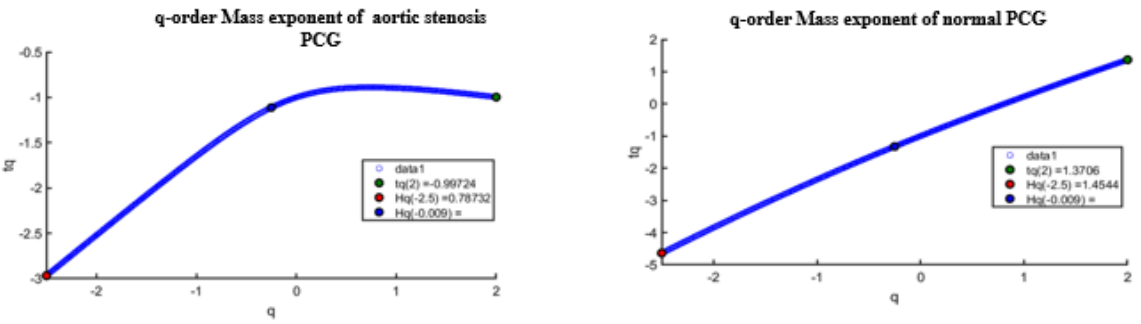

Figure 2.14. q-Order Mass Exponent Analysis for Normal Conditions and Aortic Stenosis

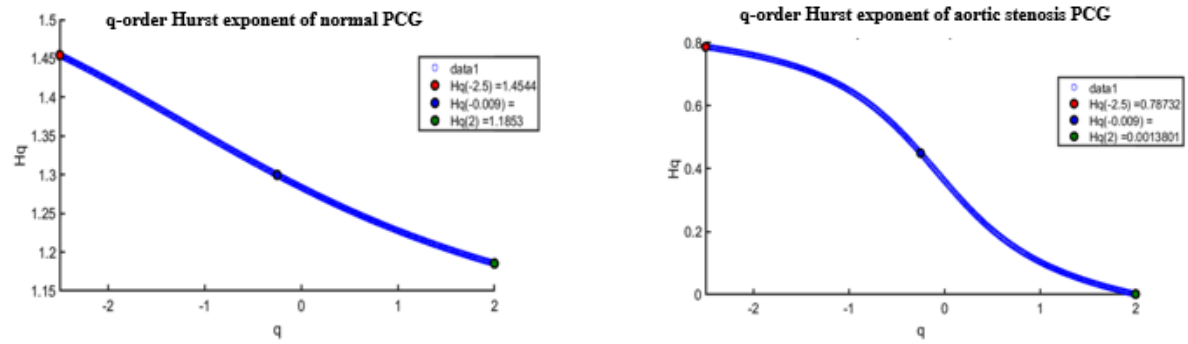

Figure 2.15. q-Order Hurst Exponent for Normal and Aortic Stenosis

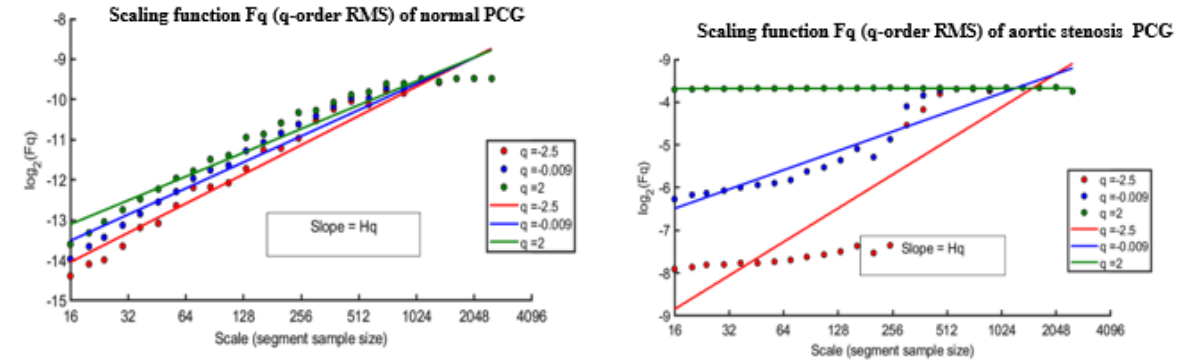

Figure 2.16. Scaling function in healthy individuals versus those with aortic stenosis

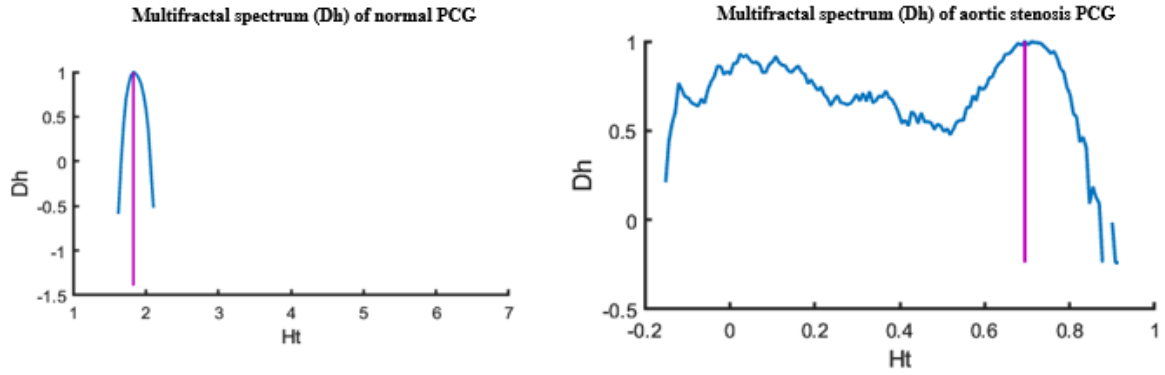

Figure 2.17. Multifractal Spectrum Derived from Local Fluctuations in Normal and Aortic Stenosis

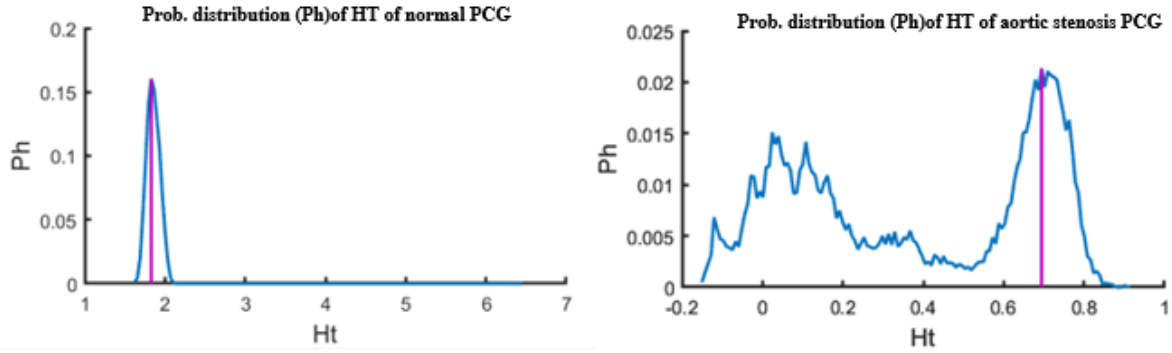

Figure 2.18. Probability Distribution of Ht for Normal Conditions and Aortic Stenosis

2.7.3 Classifiation

The classification of heart sound features using Support Vector Machine (SVM) achieved an impressive accuracy of 98.5075%. Employing SVM for phonocardiogram (PCG) signal classification offers several important contributions, which can be summarized as follows:

- Enhanced Accuracy and Noise Resilience

  SVM effectively manages complex, high-dimensional data, making it an ideal choice for PCG classification. Its capability to identify optimal decision boundaries improves classification accuracy while demonstrating robustness against noise and variability, allowing it to capture relevant patterns and minimize interference.

- Non-linearity Management and Strong Generalization

  SVM adeptly addresses non-linear relationships within PCG signals by utilizing kernel functions to transform data into higher-dimensional spaces, facilitating the detection of non-linear decision boundaries. Additionally, SVM shows strong generalization abilities, enabling it to classify unseen PCG signals accurately after training on a limited dataset, which is crucial for real-world applications.

- Clarity of Results

  SVM offers interpretable outcomes by highlighting support vectors that define classification boundaries. These vectors provide insights into the most significant features, enhancing the understanding of the classification process and its results.

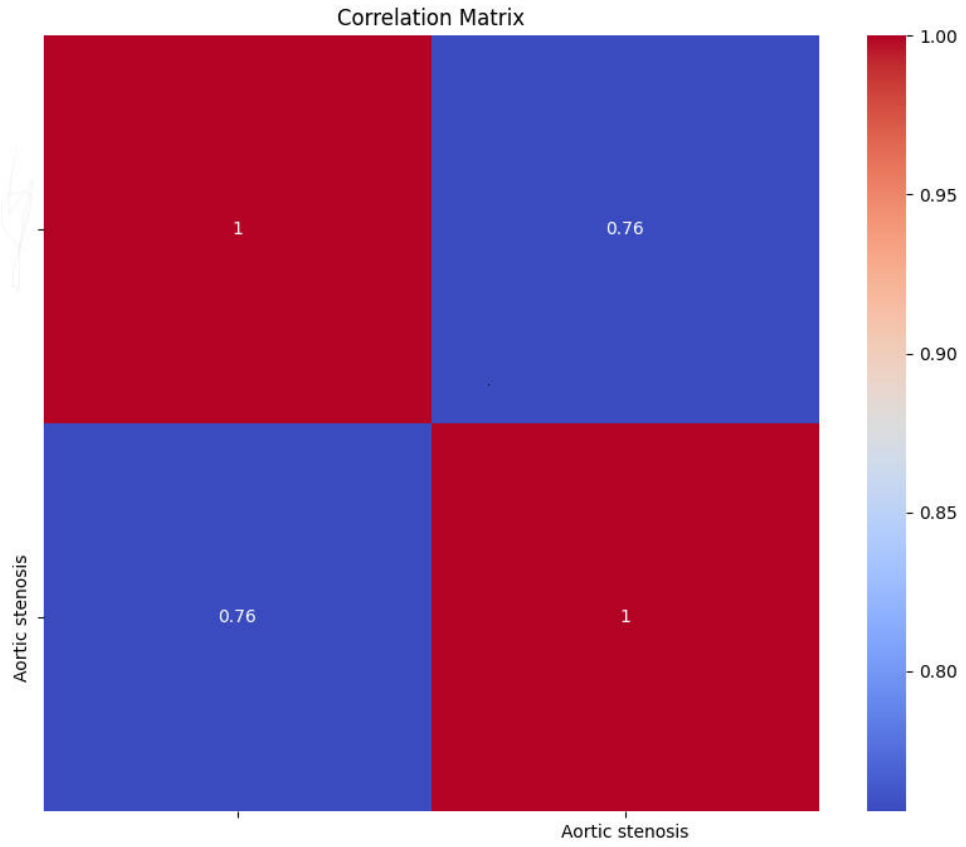

Figure 2.19. Correlation matrix comparing parameters and Aortic Stenosis Label

By outlining these advantages and underscoring the distinct benefits of using SVM for PCG signal classification, we can emphasize the specific contributions this approach offers to the analytical process. Our feature selection was guided by prior research that demonstrated their effectiveness, and we further confirmed their relevance through correlation analysis. This analysis showed a notable positive correlation coefficient of 0.76 between the parameters associated with "Normal" and "Aortic Stenosis" conditions, indicating a significant linear relationship between these variables, as illustrated in Figure 2.19. The high classification accuracy achieved with our SVM model, combined with this strong correlation, underscores the importance of all parameters in distinguishing between different pathologies. Each parameter contributes unique and critical insights essential for accurate classification, which is reflected in our impressive results.Therefore, incorporating all parameters into our classification model is vital for optimal performance.

2.8 Discussion

The multifractal detrended fluctuation analysis (MFDFA) applied to phonocardiogram (PCG) signals provides critical insights into their complex fractal characteristics. Key metrics derived from MFDFA, such as the generalized fractal dimension spectrum (Dq) and the Hölder exponent spectrum (Dh), enhance our understanding of the scaling behaviors and local dynamics of PCG signals [56] [2]. The Dq spectrum effectively characterizes the multifractal properties, while the Dh spectrum captures local behaviors and small-scale variations, which are essential for analyzing singularities in continuous functions [6].

In prior studies, including those by Mohamed Mostafa et al. [8], fractal analysis combined with support vector machines (SVM) was used to analyze heart sound signals. Their approach utilized Butterworth filtering, while we employed discrete wavelet transform (DWT) and focused on MFDFA1 and MFDFA2 functions. Their research aimed at classifying heart valve diseases and coronary artery diseases more generally, whereas our analysis specifically targets aortic stenosis. Similarly, Ana Gavrovska et al. [23] investigated mitral valve prolapse (MVP), achieving a 96% accuracy rate by extracting Hurst exponents, and later enhanced their analysis with a local variance estimation method. Other studies, such as those by Yineng et al. [55] and Thomas et al. [50], further demonstrated the effectiveness of fractal analysis in classifying various cardiac conditions, yielding results comparable to ours. Our research achieved an

Year / Authors	Approach	Categories	Attributes	classifier	Outcomes
2017,Azmy et al. [8]	MFDFA	Individuals without health issues who have conditions like coronary artery disease or heart valve disorders	Hq, tq, hq, Ph, Dq	SVM	Acc: 96.875 %
2015,Zheng et al. [55]	MF-DFA, MF-DFA -EMD	Health-CHF	-Fq,-PSD,-IMF	LS-SVM	Acc: 95.39 %
2016,Thomas et al.[50]	Segmentation using MF-DFA	Heart sound –Mitral Regurgitation	-S1,-S2	/	Demonstrated efficiency in processing time and overall accuracy in detecting heart sound
2022,Zheng et al. [56]	-Time Area, -Frequency Area, -Extraction of Nonlinear Features	Phonocardiogram Signals, Heart Sound Frequency Band Signals, Heart Sound Segments	-Multi-faceted Heart Sound Features, -Multi-scale Heart Sound Characteristics	LS-SVM	Acc: 82.10 %
2014,Gavrovska et al. [24]	-Multifractal Detrended Fluctuation Analysis, -local variance assessment	Normal PCG-Aortic stenosis PCG	- Variance,-H Hurst exponent	/	Narrow range of healthy behaviour
2013,Gavrovska et at.[23]	Multifractal Evaluation	Healthy and Mitral Valve Prolapse Heart Sound Signals	Hurst exponent H	Algorithm	Dataset with 97 recordings achieved an accuracy of 96.91%, while the dataset with 20 recordings attained an accuracy of 90%
2016,Thomas et al.[50]	multifractal analysis (singularity spectra analysis)	PCG signals for Mitral Regurgitation categorized as moderate, moderately severe, and severe	Hurst exponent Hq	/	Multifractal analysis can serve as an initial diagnostic approach to quantify mitral regurgitation by utilizing PCG
Proposed Method	**multifractal analysis MFDFA**	**PCG signals for Normal and Aortic Stenosis conditions**	**Ht (maximum, mode, minimum), tq (maximum, mode, minimum), Hq (maximum, mode, minimum), Dq (maximum, mode, minimum), hq (maximum, mode, minimum), and RMS**	**Support Vector Machine**	**accuracy of 98.5075 %**

Table 2.4: Literature Comparison

impressive accuracy rate of 98.5075% in detecting aortic stenosis, highlighting the efficacy of the MFDFA method when combined with SVM classification. This surpasses previous efforts and underscores the potential of this approach for improving early detection and diagnosis, ultimately enhancing patient outcomes. Notably, significant differences in scaling ranges between PCG signals from patients with aortic stenosis and those deemed normal reveal distinct fractal characteristics. Normal signals exhibit a narrow scaling range and a simpler multifractal structure, indicated by a minimal value of hq(max) − hq(min) (0.49274). In contrast, aortic stenosis signals show a broader scaling range and a more complex multifractal structure, reflected by a larger value of hq(max) − hq(min) (1.0326) (Figure 2.13).

The Hq graph for aortic stenosis significantly contrasts with that of normal signals, displaying lower Hq values (Figure 2.15), which implies a reduction in long-range correlations in the aortic stenosis signal compared to normal conditions. This alteration may stem from changes in the aortic valve's physical characteristics or shifts in blood flow, affecting the cardiovascular system's dynamics. Furthermore, the scaling function Fq, depicted in Figure 2.16, reveals that the scaling properties and complexities associated with aortic stenosis diverge from those in healthy cases [8] [23]. Analyzing the correlation between the fractal dimension Dh and the height parameter Ht in Figure 2.17 reveals a significant peak at approximately 1.7 times the value of Ht, indicating a specific frequency range where the fractal dimension is maximized. Conversely, the histogram of PCG data for aortic stenosis displays a complex pattern with multiple peaks and troughs, suggesting increased variability. The probability distribution of different Hurst exponents in PCG signals, as shown in Figure 2.18, highlights the complexity and self-similarity of the signals. Healthy cases show a narrow distribution, indicating stability, while pathological cases exhibit a distribution with two peaks, reflecting greater variability influenced by underlying factors or conditions [8].

However, it is crucial to recognize the limitations of MFDFA, particularly in selecting appropriate parameters like the q order and scale range, as these choices significantly affect the results. In conclusion, applying MFDFA to PCG signals has yielded valuable insights into their complexity and fractal characteristics, effectively distinguishing between normal and aortic stenosis cases. Despite the promising accuracy and correlations observed, further research and validation are necessary to better understand the clinical implications and effectiveness of this method in cardiovascular diagnostics.

2.9 Conclusion

This study focused on the innovative application of signal processing techniques to differentiate between "Normal" and "Aortic Stenosis" heart conditions. By employing advanced machine learning methods, specifically SVM, the analysis achieved an impressive accuracy of 98.5075 %, indicating a significant advancement in the diagnostic potential of PCG signal analysis.

The integration of MFDFA with SVM represents a novel approach to identifying cardiac pathologies. This method effectively harnessed features from PCG signals to classify conditions, particularly highlighting the differences associated with aortic stenosis. The results emphasize the method's capability to enhance diagnostic accuracy in clinical settings.

Future research should expand this approach by incorporating a more extensive dataset that includes a broader range of cardiac conditions. This would allow for a more comprehensive validation of the methodology and its applicability in diverse clinical scenarios. Overall, the findings underscore the importance of innovative analytical techniques in improving the detection and understanding of cardiovascular diseases.

CHAPTER 2

Bibliography

[1] Paul S Addison. *Fractals and chaos: an illustrated course*. CRC Press, 1997.

[2] Mehmet Furkan Akça and Onur Sevli. Predicting acceptance of the bank loan offers by using support vector machines. *International Advanced Researches and Engineering Journal*, 6(2):142–147, 2022.

[3] Aftab Alam, Nanping Wang, Ermioni Petraki, Adnan Barkat, Fuqiong Huang, Muhammad Ali Shah, Demetrios Cantzos, Georgios Priniotakis, Panayiotis H Yannakopoulos, Michail Papoutsidakis, et al. Fluctuation dynamics of radon in groundwater prior to the gansu earthquake, china (22 july 2013: M s= 6.6): Investigation with dfa and mfdfa methods. *Pure and Applied Geophysics*, 178(9):3375–3395, 2021.

[4] Eugen Mircea Anitas. Fractal analysis of dna sequences using frequency chaos game representation and small-angle scattering. *International Journal of Molecular Sciences*, 23(3):1847, 2022.

[5] Kanche Anjaiah, Pradipta Kishore Dash, and Mrutyunjaya Sahani. A new protection scheme for pv-wind based dc-ring microgrid by using modified multifractal detrended fluctuation analysis. *Protection and Control of Modern Power Systems*, 7(1):1–24, 2022.

[6] A Atbi, SM Debbal, F Meziani, and A Meziane. Separation of heart sounds and heart murmurs by hilbert transform envelogram. *Journal of medical engineering & technology*, 37(6):375–387, 2013.

[7] Alberto Averna, Stefania Coelli, Rosanna Ferrara, Sergio Cerutti, Alberto Priori, and Anna Maria Bianchi. Entropy and fractal analysis of brain-related neurophysiological signals in alzheimer's and parkinson's disease. *Journal of neural engineering*, 20(5):051001, 2023.

[8] Mohamed Moustafa Azmy and Reem Mohamady. Heart sounds recognition using multifractal detrended fluctuation analysis and support vector machine. In *2017 IEEE Jordan Conference on Applied Electrical Engineering and Computing Technologies (AEECT)*, pages 1–4. IEEE, 2017.

[9] Olaniyan Akintunde Babatunde, Sunday Olakunle Olarewaju, Adeleye Abiodun Adeomi, Joel Olufunminiyi Akande, Adebobola Bashorun, Chukwuma David Umeokonkwo, and James Olusegun Bamidele. 10-year risk for cardiovascular diseases using who prediction chart: findings from the civil servants in south-western nigeria. *BMC cardiovascular disorders*, 20:1–10, 2020.

[10] Michael Batty and Paul A Longley. *Fractal cities: a geometry of form and function*. Academic press, 1994.

[11] Rabindev Bishal, Gabriel B Mindlin, and Neelima Gupte. Multifractal analysis of birdsong and its correlation structure. *Physical Review E*, 105(1):014118, 2022.

[12] Colin Campbell and Yiming Ying. *Learning with support vector machines*. Springer Nature, 2022.

[13] P Carvalho, P Gilt, J Henriques, L Eugénio, and M Antunes. Low complexity algorithm for heart sound segmentation using the variance fractal dimension. In *IEEE International Workshop on Intelligent Signal Processing, 2005.*, pages 194–199. IEEE, 2005.

[14] Kranthikumar Chanda, Shubham Shet, Bishwajit Chakraborty, Arvind K Saran, William Fernandes, and G Latha. Fish sound characterization using multifractal detrended fluctuation analysis. *Fluctuation and Noise Letters*, 19(01):2050009, 2020.

[15] Kim Christensen. Percolation theory. *Imperial College London*, 1:87, 2002.

[16] David Cornforth, Herbert F Jelinek, and Mika Tarvainen. A comparison of nonlinear measures for the detection of cardiac autonomic neuropathy from heart rate variability. *Entropy*, 17(3):1425–1440, 2015.

[17] Lokenath Debnath*. A brief historical introduction to fractals and fractal geometry. *International Journal of Mathematical Education in Science and Technology*, 37(1):29–50, 2006.

[18] Xiaojian Ding, Jian Liu, Fan Yang, and Jie Cao. Random radial basis function kernel-based support vector machine. *Journal of the Franklin Institute*, 358(18):10121–10140, 2021.

[19] Srimonti Dutta, Dipak Ghosh, and Sucharita Chatterjee. Multifractal detrended fluctuation analysis of human gait diseases. *Frontiers in physiology*, 4:55963, 2013.

[20] John W Essam. Percolation theory. *Reports on progress in physics*, 43(7):833, 1980.

[21] M Fernández-Martínez and Miguel A Sánchez-Granero. Fractal dimension for fractal structures: A hausdorff approach revisited. *Journal of Mathematical Analysis and Applications*, 409(1):321–330, 2014.

[22] Lucas G Souza França, José G Vivas Miranda, Marco Leite, Niraj K Sharma, Matthew C Walker, Louis Lemieux, and Yujiang Wang. Fractal and multifractal properties of electrographic recordings of human brain activity: toward its use as a signal feature for machine learning in clinical applications. *Frontiers in physiology*, 9:1767, 2018.

[23] Ana Gavrovska, Goran Zajić, Irini Reljin, and Branimir Reljin. Classification of prolapsed mitral valve versus healthy heart from phonocardiograms by multifractal analysis. *Computational and mathematical methods in medicine*, 2013(1):376152, 2013.

[24] Ana M Gavrovska, Milorad P Paskaš, Irini S Reljin, and Branimir D Reljin. On variance based methods in computer-aided phonocardiography. In *12th Symposium on Neural Network Applications in Electrical Engineering (NEUREL)*, pages 9–12. IEEE, 2014.

[25] Ary L Goldberger. Fractal variability versus pathologic periodicity: complexity loss and stereotypy in disease. *Perspectives in biology and medicine*, 40(4):543–561, 1997.

[26] Gao-Feng Gu and Wei-Xing Zhou. Detrended fluctuation analysis for fractals and multifractals in higher dimensions. *Physical Review E—Statistical, Nonlinear, and Soft Matter Physics*, 74(6):061104, 2006.

[27] Jingchao Guo, Anhai Li, and Rufeng Zhang. Tool condition monitoring in milling process using multifractal detrended fluctuation analysis and support vector machine. *The International Journal of Advanced Manufacturing Technology*, 110:1445–1456, 2020.

[28] Donald E Herbert. Fractal physiology, by james b. bassingthwaighte, larry s. liebovitch, and bruce j. west and nonlinear dynamics and chaos, by steven h. strogatz, 1996.

[29] Espen AF Ihlen. Introduction to multifractal detrended fluctuation analysis in matlab. *Frontiers in physiology*, 3:141, 2012.

[30] M Jannesar, T Jamali, A Sadeghi, SMS Movahed, G Fesler, E Meyer, B Khoshnevisan, and GR Jafari. Multiscaling behavior of atomic-scale friction. *Physical Review E*, 95(6):062802, 2017.

[31] Dah-Jing Jwo, Jia-Chyi Wu, and Kuan-Lin Ho. Support vector machine assisted gps navigation in limited satellite visibility. *Computers, Materials & Continua*, 69(1), 2021.

[32] Maha Abdulameer Kadhim. Analysing and processing medical images with increased performance using fractal geometry. *Periodicals of Engineering and Natural Sciences (PEN)*, 10(1):544–556, 2022.

[33] Khalil Valizadeh Kamran, Bakhtiar Feizizadeh, Behnam Khorrami, and Yousef Ebadi. A comparative approach of support vector machine kernel functions for gis-based landslide susceptibility mapping. *Applied Geomatics*, 13(4):837–851, 2021.

[34] Selim Kara, Ertan Arda, and Önder Pekcan. Fractal dimensions of κ-carrageenan gels during gelation and swelling. *Journal of Macromolecular Science, Part B*, 57(11-12):715–731, 2018.

[35] Ghriti Khanna and Narinder Sharma. Fractal antenna geometries: A review. *International Journal of Computer Applications*, 153(7):29–32, 2016.

[36] Salim Lahmiri, Chakib Tadj, and Christian Gargour. Nonlinear statistical analysis of normal and pathological infant cry signals in cepstrum domain by multifractal wavelet leaders. *Entropy*, 24(8):1166, 2022.

[37] Qing-Hui Liu, Li-Feng Xi, and Yan-Fen Zhao. Dimensions of intersections of the sierpinski carpet with lines of rational slopes. *Proceedings of the Edinburgh Mathematical Society*, 50(2):411–427, 2007.

[38] Yongmin Liu, Xingming Guo, and Yineng Zheng. An automatic approach using elm classifier for hfpef identification based on heart sound characteristics. *Journal of medical systems*, 43(9):285, 2019.

[39] Vasudev P Mahale, Bishwajit Chakraborty, V Purnachandra Rao, and Tejas Salkar. Characterization of carbonate platform bathymetry off western india employing multifractal detrended fluctuation analysis (mfdfa). In *OCEANS 2022-Chennai*, pages 1–5. IEEE, 2022.

[40] Benoit B Mandelbrot, Carl JG Evertsz, and Martin C Gutzwiller. *Fractals and chaos: the Mandelbrot set and beyond*, volume 3. Springer, 2004.

[41] Jorge Luis Morales Martínez, Ignacio Segovia-Domínguez, Israel Quiros Rodríguez, Francisco Antonio Horta-Rangel, and Guillermo Sosa-Gómez. A modified multifractal detrended fluctuation analysis (mfdfa) approach for multifractal analysis of precipitation. *Physica A: Statistical Mechanics and its Applications*, 565:125611, 2021.

[42] Laura Raisa Miloş, Cornel Haţiegan, Marius Cristian Miloş, Flavia Mirela Barna, and Claudiu Boţoc. Multifractal detrended fluctuation analysis (mf-dfa) of stock market indexes. empirical evidence from seven central and eastern european markets. *Sustainability*, 12(2):535, 2020.

[43] Nitish Kumar Mishra, Manish Kumar, and GPS Raghava. Support vector machine based prediction of glutathione s-transferase proteins. *Protein and peptide letters*, 14(6):575–580, 2007.

[44] Peshal B Nayak. Multiband fractal antenna designs. 2020.

[45] Alejandro Ramírez-Rojas, LR Moreno Torres, and R Páez-Hernández. Multifractal analysis of seismic geoelectric signals observed prior a earthquake of m6. 7. In *2015 International Conference on Electromagnetics in Advanced Applications (ICEAA)*, pages 1098–1103. IEEE, 2015.

[46] Ertuğrul Saatçi and Esra Saatçi. Multifractal behaviour of respiratory signals. 2020.

[47] Pengjian Shang, Yongbo Lu, and Santi Kamae. Detecting long-range correlations of traffic time series with multifractal detrended fluctuation analysis. *Chaos, Solitons & Fractals*, 36(1):82–90, 2008.

[48] Debdeep Sikdar, Rinku Roy, and Manjunatha Mahadevappa. Multifractal analysis of electroencephalogram for human speech modalities. In *2017 8th International IEEE/EMBS Conference on Neural Engineering (NER)*, pages 637–640. IEEE, 2017.

[49] Luciano Telesca and Michele Lovallo. Analysis of the time dynamics in wind records by means of multifractal detrended fluctuation analysis and the fisher–shannon information plane. *Journal of Statistical Mechanics: Theory and Experiment*, 2011(07):P07001, 2011.

[50] Rijil Thomas, Ling Lieng Hsi, Soh Cheong Boon, and Erry Gunawan. Classification of severity of mitral regurgitation patients using multifractal analysis. In *2016 38th Annual International Conference of the IEEE Engineering in Medicine and Biology Society (EMBC)*, pages 6226–6229. IEEE, 2016.

[51] AHA Statistical Update. Heart disease and stroke statistics—2020 update: a report from the american heart association. *Circulation*, 141(9):e139–e596, 2020.

[52] Jithendra Vepa, Paresh Tolay, and Abhishek Jain. Segmentation of heart sounds using simplicity features and timing information. In *2008 ieee international conference on acoustics, speech and signal processing*, pages 469–472. IEEE, 2008.

[53] Hannah K Weir, Robert N Anderson, Sallyann M Coleman King, Ashwini Soman, Trevor D Thompson, Yuling Hong, Bjorn Moller, and Steven Leadbetter. Peer reviewed: heart disease and cancer deaths—trends and projections in the united states, 1969–2020. *Preventing chronic disease*, 13, 2016.

[54] Yang Yujun, Li Jianping, and Yang Yimei. Multiscale multifractal multiproperty analysis of financial time series based on rényi entropy. *International Journal of Modern Physics C*, 28(02):1750028, 2017.

[55] Yineng Zheng, Xingming Guo, Jian Qin, and Shouzhong Xiao. Computer-assisted diagnosis for chronic heart failure by the analysis of their cardiac reserve and heart sound characteristics. *Computer methods and programs in biomedicine*, 122(3):372–383, 2015.

[56] Yineng Zheng, Xingming Guo, Yingying Wang, Jian Qin, and Fajin Lv. A multi-scale and multi-domain heart sound feature-based machine learning model for acc/aha heart failure stage classification. *Physiological Measurement*, 43(6):065002, 2022.

CHAPTER 3

AI-Driven Signal Processing Techniques for the Early Identification of Pathological Conditions in Phonocardiograms

Contents

List of Figures

List of Tables

3.1 Introduction

Recent advancements in Artificial Intelligence (AI) and signal processing techniques have opened promising avenues for the early detection of pathological conditions [37, 56]. Conditions such as cardiovascular diseases can often be diagnosed through the analysis of specific patterns and abnormalities in physiological signals. Among these signals, the phonocardiogram (PCG), which captures heart sounds, has emerged as a significant source of information for identifying cardiac abnormalities [14].

Previous research has demonstrated the efficacy of AI algorithms in the automatic detection of myocardial infarction [59], employing convolutional neural networks for heart sound analysis [11], and utilizing machine learning-based classification algorithms to identify various heart disorders from PCG signals [49]. Additionally, hybrid multi-round transfer learning classifiers have been applied to PCG signal classification [57], and transfer learning approaches have been utilized in conjunction with spectrogram analysis for PCG classification [27]. Arslan et al. decomposed PCG signals into Intrinsic Mode Functions (IMFs) using the Hilbert-Huang transform, investigating the impact of these modes on the classification of PCG signals [75]. Their study highlighted the superior performance of the Deep Neural Network (DNN) model, achieving a precision of 98.9 %.

Roy et al. focused on diagnosing abnormal murmurs in heart sounds through the extraction of features from time-frequency domain representations, employing Probability Neural Networks (PNN) for feature extraction based on acoustic intensities during systole and diastole [33]. Maity explored transfer learning with pre-trained convolutional neural networks for PCG classification, achieving an overall accuracy of 99 % [36]. Another study by Samanta et al. proposed a deep Convolutional Neural Network (CNN) for classifying valvular heart diseases using PCG signals, achieving a classification accuracy of 99.6 % during fivefold cross-validation [9]. Grzegorczyk et al. introduced a machine learning algorithm based on neural networks for PCG signal analysis, utilizing a Hidden Markov Model for signal segmentation [25]. In a study by Pranab et al., simultaneous PCG signals were acquired from four auscultation sites, employing artificial neural networks (ANN) for binary classification [54]. Their proposed sub-band-based spectral features demonstrated commendable performance across both clean and noisy datasets. Rajan et al. presented a novel wavelet-based bank of correlators for PCG signal classification, utilizing Morlet wavelets as correlating filters [46]. This study also introduced a method for the detection and classification of PCG signals utilizing a simple perceptron.

Furthermore, researchers have examined the coupling analysis of PCG signals with other physiological signals, such as the Electrocardiogram (ECG), for non-destructive detection of Coronary Artery Disease (CAD) stenosis severity [17]. This approach provides valuable insights into the relationship between PCG and ECG signals, facilitating the assessment of CAD stenosis severity. Scalogram analysis and deep learning techniques have been employed for the classification of unsegmented PCG signals [15], enabling more efficient and automated solutions without the necessity for explicit segmentation. Additionally, lightweight end-to-end PCG classification neural network models have been proposed for wearable devices, facilitating real-time monitoring and diagnosis [74].

Building on these advancements, this paper presents a novel method for the classification of unsegmented PCG signals. The proposed method integrates a comprehensive feature extraction technique that utilizes a 39-filter setup as a preprocessing step to derive 39 individual signals from a single PCG signal. This extensive filtering strategy provides a detailed representation of the underlying physiological processes, enabling a thorough analysis of pathological conditions. Moreover, Multifractal Detrended Fluctuation Analysis (MFDFA), a powerful tool for decomposing complex physiological signals [27, 6, 62], is applied to the PCG signal to obtain six distinct signals, each capturing specific aspects of cardiac dynamics.

In this study, to enhance performance, the Spearman correlation-based feature selection algorithm is employed to identify the 24 most informative features from each of the 280 signals derived from the initial

PCG signal. These selected features encompass a wide range of morphological, temporal, and spectral characteristics, providing a comprehensive representation of the underlying pathological conditions. The application of the Spearman correlation-based feature selection algorithm enhances the effectiveness of the proposed approach. Various classification algorithms, including Support Vector Machines (SVM), k-nearest neighbors (kNN), Ensemble Tree methods, and hybrid models, are utilized to provide a robust assessment of performance and generalizability.

There is an increasing interest in leveraging AI and advanced signal processing techniques for the early detection of cardiac pathologies, particularly focusing on the PCG signal. Manual auscultation, which relies on subjective judgments based on a clinician's expertise, remains the conventional method for addressing pathological conditions in clinical practice. However, this method is fraught with limitations, including reliance on clinician expertise, which can lead to inconsistencies and variability in diagnosis. Additionally, it may lack the sensitivity required to detect subtle abnormalities in PCG signals, particularly in the early stages of pathology. While echocardiography (ECG) has been utilized as an alternative, it is often less accurate.

The challenge of selecting optimal features from the PCG signal for the early detection of pathologies is critical. The complexity of the PCG signal, which contains a wealth of information, necessitates the identification of the most relevant and informative features for accurate pathology detection.

This study proposes a novel approach that integrates AI algorithms with PCG signal processing to enhance the accuracy and efficiency of pathology detection. To address the challenge of selecting the most pertinent features from the PCG signal, a feature extraction algorithm specifically designed for PCG signals is utilized, incorporating MFDFA. This technique has proven effective in capturing both temporal and spectral properties present within the PCG signal.

Through the application of MFDFA, the feature extraction algorithm yields a comprehensive set of features that provide a rich representation of the underlying physiological processes. These features encompass a wide range of morphological, temporal, and spectral characteristics, enabling a thorough representation of the underlying pathological conditions.

In addition, the Spearman method is employed for feature selection, evaluating the statistical correlation between each feature and the target pathology. This allows for the identification of the subset of features that are most relevant and informative for early detection. The feature selection process aims to encompass features that capture long-range correlations, fractal properties, and other relevant temporal and spectral characteristics.

By combining the strengths of MFDFA-based feature extraction with the effectiveness of the Spearman method for feature selection, the proposed approach enhances the accuracy and efficacy of pathology detection. It ensures that the selected features capture critical information present in the PCG signal, facilitating early detection of pathologies with improved precision and reliability.

To ensure accurate early detection, various classification models are employed, with the algorithm's performance hinging on the selection and optimization of specific parameters. Future research should focus on further validating this method using clinical and experimental data to demonstrate its validity and applicability within the clinical and diagnostic medical fields.

The organization of this paper is as follows: Section 3.2 outlines the methodologies employed, including PCG denoising, MFDFA analysis, feature extraction, and classification. The results are presented in Section 3.3, followed by an in-depth discussion in Section 3.4. Finally, Section 3.5 summarizes the conclusions drawn from this study, highlighting its implications and potential avenues for future research. Detailed elaboration of our approach can be found in the forthcoming sections.

3.2 Materials and Methods

The execution of the procedures outlined in this study adhered to the methodological framework illustrated in Figure 3.1.

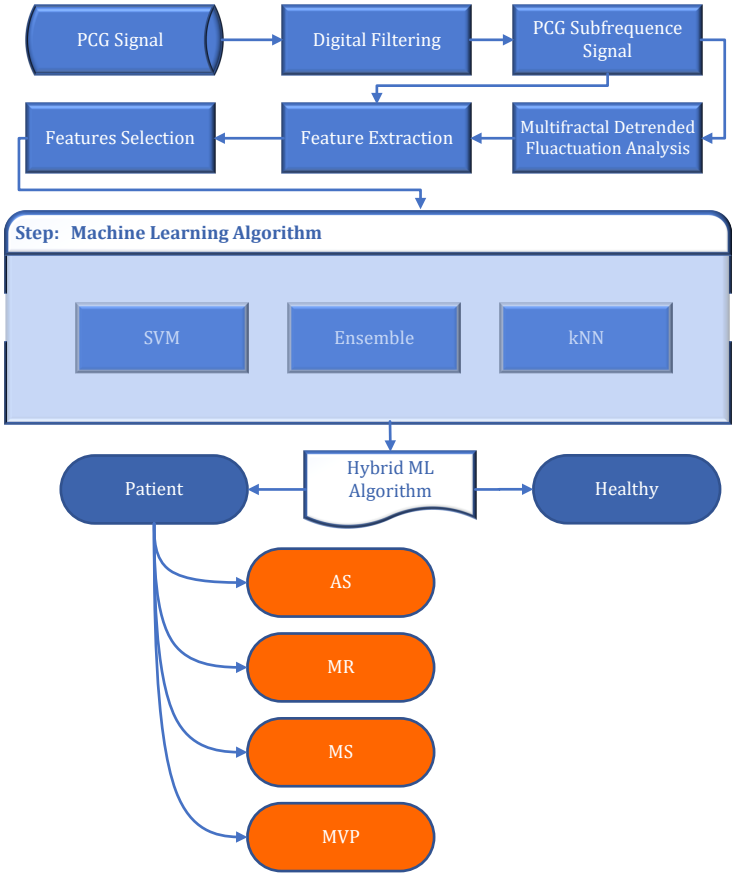

Figure 3.1: Flow Diagram

AS: Aortic stenosis, MR: Mitral Regurgitation, MS: Mitral Stenosis, MVP: Mitral Valve Prolapse

3.2.1 Data Collection

The dataset utilized in this scientific study encompasses a comprehensive collection of 1000 PCG signals, which have been meticulously categorized into five distinct classes as delineated in Table 3.1. These signals were derived from a publicly accessible repository hosted at the Github [71].

3.2.2 Signal Filtering

In order to obtain more information from the PCG signal, the signal was divided into different frequency components by applying a digital filter (Table 3.2). In the literature S1, S2, S3, and S4 frequency ranges have been reported at different values [12]. Additionally, different values have been reported in the normal PCG frequency range. In order to use the PCG signal more efficiently and prevent information loss, filters have been designed for each frequency range (Table 3.2). After digital filtering, 39 new PCG signals were obtained from one PCG signal, each with a different frequency component. All filters used IIR Chebyshev Type II filter structure.

Table 3.1: Distribution Data

Label	Classes	Number of Samples Per Class
Abnormal	AS	200
	MR	200
	MS	200
	MVP	200
Normal	N	200
Total		1000

Specifically, for the PCG signals, 11 distinct ranges were identified. For the first heart sound (S1), 9 different ranges were utilized, while for the second heart sound (S2), 7 ranges were employed. Additionally, for the third heart sound (S3), 6 ranges were utilized, and for the fourth heart sound (S4), 6 distinct filter ranges were also employed (Table 3.2).

After the filtering process, a total of 39 signals were obtained. Together with the first signal, a total of 40 signals of an individual to be continued to be processed.

Table 3.2: Filter frequency ranges applied to the PCG signal

No	FR	Normal PCG Information	R	No	S1	R	No	S2	R	No	S3	R	No	S4	R
1	100-600 Hz	Abnormal-Aortic Stenosis AS	[**3**]	**1**	50–150 Hz	[**38**]	**1**	50–200 Hz	[**38**]	**1**	50–90 Hz	[**67**]	**1**	50–80 Hz	[**67**]
2	15-50 Hz	Abnormal-Gallop frequencies	[**52**]	**2**	10-120Hz	[**8**]	**2**	10-400 Hz	[**41**]	**2**	<30 Hz	[**7**]	**2**	<20 Hz	[**7**]
3	20-650 Hz	Abnormal-Heart murmurs	[**1**]	**3**	10-140 Hz	[**4**]	**3**	120-200Hz	[**8**]	**3**	15-60 Hz	[**43**]	**3**	15-45 Hz	[**43**]
4	100-1000 Hz	Abnormal-Pathological case	[**45**]	**4**	10-200 Hz	[**13**]	**4**	20–200 Hz	[**13**]	**4**	15–65 Hz	[**51**]	**4**	15–65 Hz	[**51**]
5	500-600 Hz	Abnormal heart Sound	[**63**]	**5**	10-50 Hz	[**26**]	**5**	20-250 Hz	[**13**]	**5**	20-40Hz	[**8**]	**5**	15-75 Hz	[**13**]
6	10-800 Hz	Both-healh and unhealth Heart Sound	[**52**]	**6**	20–200 Hz	[**51**]	**6**	40–70 Hz	[**7**]	**6**	25-75Hz	[**13**]	**6**	40-80Hz	[**8**]
7	5–1000 Hz	Both-PCG Signal Clinically	[**47**]	**7**	30–50 Hz	[**7**]	**7**	45–65 Hz	[**5**]						
8	20-150 Hz	Normal heart Sound	[**63**]	**8**	40–65 Hz	[**5**]									
9	20-200 Hz	Normal heart Sound	[**52**]	**9**	50-150Hz	[**38**]									
10	20-250 Hz	Normal heart Sound	[**38**]												
11	50-150 Hz	Normal heart Sound	[**34**]												

FR: Frequency Range, R: Reference

3.2.3 Multifractal Detrended Fluctuation Analysis

MFDFA was conducted on a total of 40 signals, comprising 39 filtered PCG signals and 1 raw signal. Each signal was decomposed into six distinct components to capture their inherent multifractal properties. Thus, yielding a total of 240 signals (40 signals $\times$ 6 components). The comprehensive findings of this analysis are succinctly summarized in Table 3.4.

3.2.4 Feature Extraction

Upon decomposing the signals, the focus shifted towards extracting features from the 280 signals produced by the applied MFDFA analysis, including 39 signals obtained through filtering and the raw signal. The objective was to quantitatively identify significant characteristics that could offer valuable insights into the underlying dynamics of the PCG signals. To accomplish this, a tailored feature extraction method was employed, resulting in a total of 6720 distinct features (24 features per signal $\times$ 280 signals). These features were meticulously organized in Table 3.3, providing a comprehensive overview of the diverse set of characteristics obtained from the PCG signals. Furthermore, Table 3.4 succinctly summarized the methodology employed in the study, offering a concise outline of the preprocessing MFDFA and feature extraction processes.

Table 3.3: Mathematical and Code Representation of Time Series Features for PCG Signals

No	Feature	Equation
1	Kurtosis	$x_{kur} = \frac{\sum_{i=1}^{n}(x(i)-\overline{x})^4}{(n-1)S^4}$
2	Skewness	$x_{ske} = \frac{\sum_{i=1}^{n}(x_i-\overline{x})^3}{(n-1)S^3}$
3	* IQR	$IQR = iqr(x)$
4	CV	$CV = (S/\overline{x})100$
5	Geometric Mean	$G = \sqrt[n]{x_1 + \cdots + x_n}$
6	Harmonic Mean	$H = n/\left(\frac{1}{x_1} + \cdots + \frac{1}{x_n}\right)$
7	Activity - Hjort Parameters	$A = S^2$
8	Mobility - Hjort Parameters	$M = S_1^2/S^2$
9	Complexity - Hjort Parameters	$C = \sqrt{(S_2^2/S_1^2)^2 - (S_1^2/S^2)^2}$
10	* Maximum	$x_{max} = max(x_i)$
11	Median	$\underset{\sim}{x} = \begin{cases} x_{\frac{n+1}{2}} & : x \text{ odd} \\ \frac{1}{2}(x_{\frac{n}{2}} + x_{\frac{n}{2}+1}) & : x \text{ even} \end{cases}$
12	* Mean Absolute Deviation	$MAD = mad(x)$
13	* Minimum	$x_{min} = min(x_i)$
14	* Central Moments	$CM = moment(x, 10)$
15	Mean	$\overline{x} = \frac{1}{n}\sum_{i=1}^{n} = \frac{1}{n}(x_1 + \cdots + x_n)$
16	Average Curve Length	$CL = \frac{1}{n}\sum_{i=2}^{n} \lvert x_i - x_{i-1}\rvert$
17	Average Energy	$E = \frac{1}{n}\sum_{i=1}^{n} x_i^2$
18	Root Mean Squared	$X_{rms} = \sqrt{\frac{1}{n}\sum_{i=1}^{n} \lvert x_i\rvert^2}$
19	Standard Error	$S_{\overline{x}} = S/\sqrt{n}$
20	Standard Deviation	$S = \sqrt{\frac{1}{n}\sum_{i=1}^{n}(x_i - \overline{x})}$
21	Shape Factor	$SF = X_{rms}/\left(\frac{1}{n}\sum_{i=1}^{n}\sqrt{\lvert x_i\rvert}\right)$
22	* Singular Value Decomposition	$SVD = svd(x)$
23	* 25% Trimmed Mean	$T25 = trimmean(x, 25)$
24	* 50% Trimmed Mean	$T50 = trimmean(x, 50)$
25	Average Teager Energy	$TE = \frac{1}{n}\sum_{i=3}^{n}(x_{i-1}^2 - x_i x_{i-2})$

*** The property was computed using MATLAB**

IQR Interquartile Range, CV Coefficient of Variation

S^2**: variance of the signal** x

S_1^2**: Variance of the 1st derivative of the signal** x

S_2^2**: Variance of the 2nd derivative of the signal** x

Table 3.4: Methodology

Data	Signal Name	Number of Signal	Number of Feature
Original Signal	**Raw Signal**	1	24
Filtered Signal	**Normal**	11	264
	S1	9	216
	S2	7	168
	S3	6	144
	S4	6	144
	Total	40	960
MFDFA Method Applied Signal	**Raw Signal**	6	144
	Normal	66	1584
	S1	54	1296
	S2	42	1008
	S3	36	864
	S4	36	864
	Total	240	5760
Total		280	6720

3.2.5 Spearman Feature Selection Algorithm

In the current stage of the feature selection process, Spearman correlation coefficient calculations were performed between 6720 distinct features derived from 280 signals and the target variable for both normal and pathological cases.

Table 3.5: Feature Selection

		MKU	MFDFA	All
NSF	5%	48	288	336
	10%	96	576	672
	15%	144	864	1008
	20%	192	1152	1344
	25%	240	1440	1680
	30%	288	1728	2016
	35%	336	2016	2352
	40%	384	2304	2688
	45%	432	2592	3024
	50%	480	2880	3360
NTF	100%	960	5760	6720

NSF: Number of Selected Features
NTF: Number of Total Features

The Spearman correlation coefficient is a useful measure for assessing the monotonic relationship between variables, particularly in the presence of nonlinear relationships [64]. By evaluating the Spearman correlation, the strength and direction of the association between each feature and the target variable were determined. Subsequently, the features were ranked in descending order based on their Spearman correlation coefficients. A higher correlation coefficient indicated a stronger relationship with the target

variable. This ranking enabled prioritization of features that are likely to provide more informative and relevant insights for further analysis. To refine the feature set, the features were organized into 10 groups, with each group containing a specific number of selected features. The determination of the number of features in each group was guided by the desired balance between feature richness and model complexity, as outlined Table 3.5.

3.2.6 Machine Learning Algorithm

This study developed an innovative hybrid model that combines the strengths of three different machine learning algorithms used in the classification of PCG signals. This model includes popular techniques such as SVM,DT, kNN and Ensemble Tree, which also stand out in the literature with high accuracy rates.

Support Vector Machines (SVM)

SVM address classification or regression problems using a quadratic programming technique. Thanks to this approach, it provides a significant advantage in problem solving by eliminating the risk of getting stuck in local minima [18]. The basic principle of SVM is to find a classification hyperplane or hyperspace to separate data points. The most important features used by this method are:

Maximum Margin Principle: SVM tries to find the widest margin (i.e. largest gap) between classes. This wide margin increases the generalization ability of the model and creates a model that is more resistant to overfitting [18].

Kernel Trick: SVM utilize kernel functions to model non-linear relationships. These functions transform the data into a higher-dimensional space, making it linearly separable. Popular kernel functions include the Radial Basis Function (RBF), polynomial, and sigmoid kernels [58].

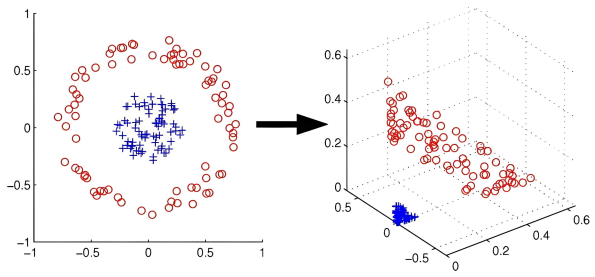

Figure 3.2: Kernel Trick in SVM [48]

On the left side of Figure 3.2, data points belonging to two different classes (red squares and green circles) are shown intermixed. This scenario represents a situation where separation with a linear line is not possible. For such datasets, SVM can use non-linear kernels such as RBF (Radial Basis Function) instead of linear kernels.On the right side of the visualization, data points are transformed into a three-dimensional space using the kernel method, and a surface (decision surface) separates them. In this new space, the distinction between the two classes is clearly made by the decision surface. Thus, the kernel method enables separation by transforming the data points into a ”feature space”.

In machine learning, understanding the nature of data and selecting appropriate kernels plays a crucial role in the success of a model. With this approach, SVM algorithms can provide flexible and effective solutions to complex classification problems.

Robustness: SVM is robust against small variations in the feature space, which means that the model tends to produce consistent results on different datasets [69].

Soft Margin Classifier: In real-world data, achieving a perfect separation may not always be possible. SVM handles this situation by allowing some data points to be on the wrong side of the margin (i.e., by tolerating some errors). This flexibility enables the model to perform well even on slightly noisy data [68].

k-Nearest Neighbors (kNN)

kNN algorithm, introduced by Fix and Hodges in 1952, is a widely preferred non-parametric approach for classification and regression problems. Considered one of the fundamental techniques in machine learning, kNN is characterized by the value of k used for feature selection. This value ensures the selection of the most common class among the k nearest neighbors based on the closest k neighbors in the dataset to determine the class of a point. As shown in Figure 3.3, the algorithm attempts to determine the nearest neighbors among all examples in the dataset for each sample. Therefore, an increase in the size of the dataset can significantly increase the computational workload [10].

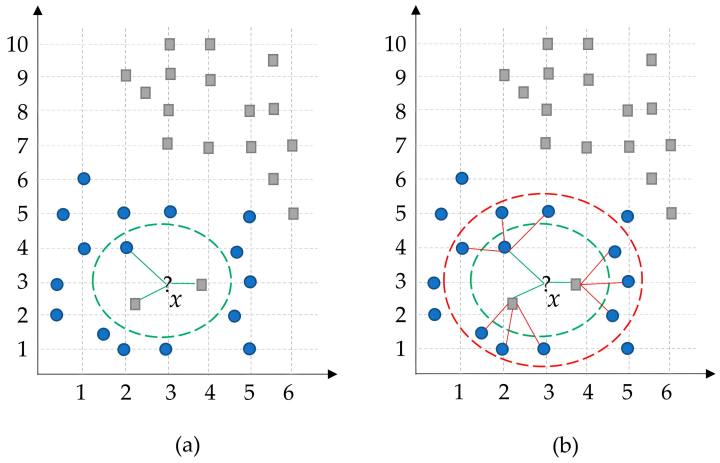

Figure 3.3: k-Nearest Neighbors Algorithm. (a) low-level neighborhood; (b) high-level neighborhood. (?, circle, square, red and green dot boxes, and lines respectively represent the neighbors of an instance point x, a specific class of instances, another specific class of instances, boundaries indicating high-level neighborhood and low-level neighborhood, and the membership of neighbors to an instance point [32].)

The time complexity of kNN is low because training only involves calculating the Euclidean distance [21]. When making predictions for a classification or regression problem, the algorithm calculates the Euclidean distance between a given query point (test example) and the existing points in the dataset. The Euclidean distance d, is defined as the linear distance between two points and is calculated using the following formula:

$$d(p,q) = \sqrt{(q_1 - p_1)^2 + (q_2 - p_2)^2 + \cdots + (q_n - p_n)^2} \tag{3.1}$$

Here, p and q represent two points in an n-dimensional space, and $p_1, p_2, \ldots, p_n$ ile $q_1, q_2, \ldots, q_n$ are the coordinates of these points. In the kNN algorithm, to predict a class, the Euclidean distance between the test example and each example in the training dataset is calculated, and the k nearest neighbors with the shortest distances are identified. The classes of these neighbors are then used to predict the class of the test example using majority vote or weighted methods.

As the kNN algorithm relies on a distance-based approach, normalizing the training data can significantly improve the classification accuracy of the algorithm.

Ensemble Decision Trees

Ensemble Decision Trees is a machine learning technique that consists of combining multiple decision trees. This approach offers more powerful and accurate predictions by overcoming the limitations of a single model. Popular ensemble methods such as Bagging, Boosting, and Random Forest combine multiple decision trees trained on different subsets of data. Thus, they address the overfitting problem, which is common in traditional decision trees, by splitting the dataset and features into multiple parts and processing them on multiple trees [55].
Figure 3.4 below shows an Ensemble Decision Tree model with three trees.

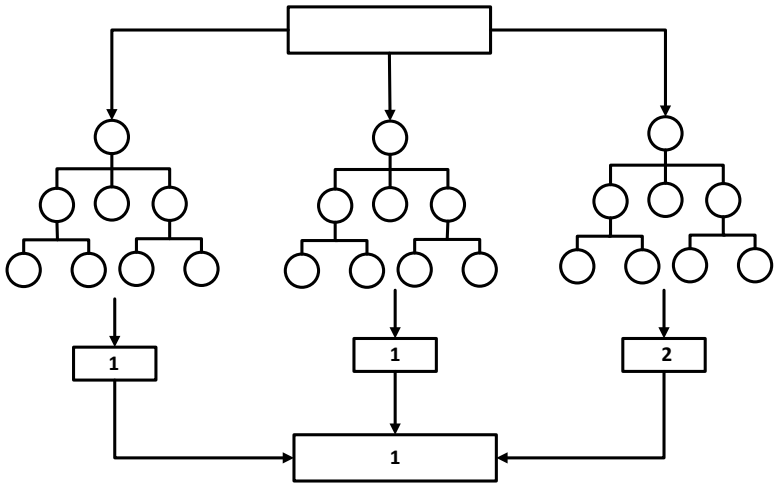

Figure 3.4: Ensemble Decision Trees structure

This model expands the limited analysis offered by each decision tree alone, obtaining more stable and reliable predictions with an integrated approach.

Hybrid Machine Learning Algorithm

Hybrid methods are approaches that aim to achieve higher performance by combining the characteristics of different prediction methods [55].
In this study, a Hybrid model encompassing SVM, kNN, and Ensemble Decision Trees has been designed. This tribrid model integrates the advantages of SVM, kNN, and Ensemble Decision Trees. By doing so, it enhances the prediction accuracy and generalization ability of the model while strengthening its performance on different datasets through the diversity provided by different algorithms (Figure 3.5).

3.2.7 Performance Evaluation Criteria

During the construction of machine learning models, 80% of the data was utilized for the training phase, while the remaining 20% was allocated for the testing phase.
In this study, six basic criteria commonly used in the literature to evaluate model performance are discussed: Accuracy, Specificity, Sensitivity, F-Measure, Kappa and AUC values. These metrics enable a comprehensive examination of the model's overall and specific case performance on the dataset.
Accuracy is one of the metrics that quantitatively expresses the overall performance of a classification model. This metric reflects how accurate the model's predictions are and is expressed as the ratio of the number of samples correctly classified (TP and TN) by the model over the total number of samples [65].

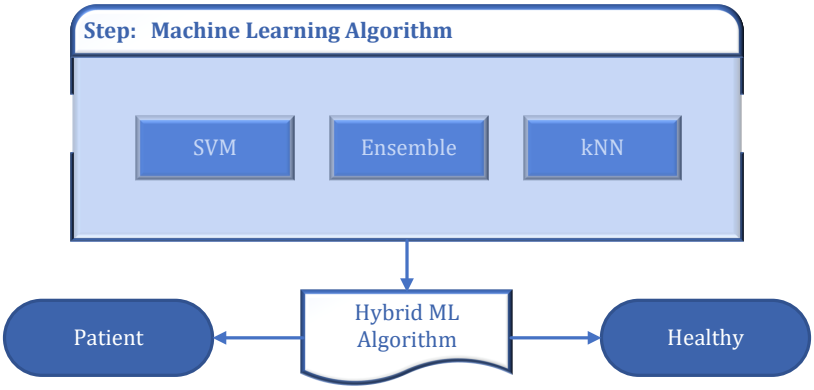

Figure 3.5: Hybrid ML Algorithm

$$\text{Accuracy} = \frac{TP + TN}{TP + TN + FP + FN} \tag{3.2}$$

Specificity is a ratio that indicates how effectively a classification model detects healthy individuals. This metric is expressed as the ratio of the number of healthy individuals that the model correctly classifies as negative (TN) to the total number of individuals that are actually healthy. In other words, specificity reflects how successfully the model recognizes healthy individuals and does not misclassify them as diseased. The calculation formula for specificity is [65]:

$$\text{Specificity} = \frac{TN}{TN + FP} \tag{3.3}$$

Sensitivity is a ratio that indicates how effectively the classification model detects the positive class. This metric is expressed as the ratio of the number of examples that the model correctly classifies as positive to the total number of examples that are actually positive. In other words, sensitivity reflects how successfully the model recognizes a positive situation and does not misclassify it as a negative. The calculation formula for sensitivity is [65]:

$$Sensitivity = \frac{TP}{TP + FN} \tag{3.4}$$

Sensitivity is a vital metric in medical diagnostics and statistical modeling, especially in diagnosing serious health problems such as heart disease. High sensitivity in heart disease research is crucial to minimizing false negative results, as such errors can pose serious health risks to patients [39].

F-Measure, F-Measure is the harmonic mean of precision and sensitivity. Its value varies between 0 and 1; 1, excellent performance; 0 indicates poor performance. This score balances both the model's ability to correctly detect the positive class and its false positive rate. Thus, it more clearly reflects the overall performance of the classification algorithm. F-Measure is calculated by taking the harmonic mean of precision and recall values with the following formula [40]:

$$FMeasure = \frac{2 \times (\text{Precision} \times \text{Recall})}{\text{Precision} + \text{Recall}} \tag{3.5}$$

AUC, this metric is one of the important statistical measures used in the performance evaluation of medical diagnostic models. AUC is obtained by measuring the area under the Receiver Operating Characteristic (ROC) curve and quantitatively expresses the capacity of the classification model to distinguish different situations. The AUC value is calculated on a scale ranging from 0 to 1. It shows how effectively the model distinguishes between positive (disease is present) and negative (disease is not present) states;

A high AUC value indicates that the model performs this discrimination with high accuracy. This feature plays a critical role in determining the reliability of the model, especially in accurately diagnosing serious health problems such as heart disease [40].

Kappa value is an important statistical metric that measures how much a classification model deviates from random guesses. This statistical measure calculates the model's observed fit rate by comparing it to a random fit rate. The kappa value varies between -1 and 1, but generally takes a value between 0 and 1. The closer the kappa value is to 1, the better the model's predictions fit the observed data; when it is 1, it indicates that they are in perfect agreement [16]. As the kappa value approaches 0, it indicates that the predictions are in line with random guesses, that is, they do not differ from the level expected by random chance. On the other hand, negative Kappa values approaching -1 indicate that the model's predictions are inversely proportional to the observed data, and when -1, there is a perfect incompatibility between them [31].

The table below shows 3.6, a scale developed by Landis and Koch in 1977 and used in interpreting the Kappa statistic. This scale has been adopted as a standard method for assessing the level of agreement of two or more observers' evaluations, especially in clinical and practical research [16].

Table 3.6: Interpretation Ranges for Kappa Statistics

Kappa Statistic	Strength of the Agreement
<0.00	Poor
0.00 - 0.20	Slight
0.21 - 0.40	Fair
0.41 - 0.60	Moderate
0.61 - 0.80	Substantial
0.81 - 1.00	Almost Perfect

Kappa statistics indicate the stability and reliability of the model, especially in cases where there is class imbalance. It is important in evaluating its quality. In fields such as heart disease diagnostic models, the Kappa statistic is used to determine how well the model's classification decisions differ from random guesses and how well it represents actual conditions [40].

In the study, the performance of various classification models was evaluated in terms of different performance metrics on the full feature set and feature sets selected through various algorithms. Research results have revealed how effectively these models and algorithms can be used in the diagnosis of heart disease. It is anticipated that the proposed system will be useful and helpful for doctors and other healthcare providers in accurately and effectively diagnosing patients with heart disease at early stages.

3.3 Results

The aim of this study is to utilize advanced AI and PCG Signal Processing Techniques for the early detection of pathologies. The study employs various classification methods, including kNN, DT, SVM, Ensemble Tree Methods and Hybrid. The results, presented in Table 3.7, Table 3.8 and Table 3.9, provide an evaluation of the performance criteria for the Binary Classification Task (Normal vs. Pathological Cases) with Holdout "20." The evaluation is conducted using features without MFDFA method, features with MFDFA method and all features respectively. The evaluation considers four classification methods: kNN, SVM, Ensemble Tree Methods and Hybrid

Across all three datasets (Time Series Feature, MFDFA Features, All Features), the Ensemble and Hybrid methods consistently achieve the highest performance in terms of accuracy, sensitivity, specificity, F-

Measure, Kappa and AUC. This indicates that these methods are robust and effective in handling datasets with varying levels of feature selection and a large number of features (Figure3.7 ,3.8 and 3.6).
SVM and kNN also show good performance, but they may be more sensitive to variations in the dataset and the specific task being addressed. In the Time Series Feature dataset, all four methods achieve perfect accuracy (100 %) in the majority of the experiments, indicating their ability to correctly classify all data points. In the MFDFA Features dataset, the Ensemble and Hybrid methods achieve perfect accuracy (100 %) in the majority of the experiments, while SVM and kNN achieve high accuracy scores but may experience slight variations. Similarly, in the all Features dataset, the Ensemble and Hybrid methods achieve perfect accuracy (100%) in the majority of the experiments, while SVM and kNN achieve high accuracy scores but may experience slight variations.
All four methods consistently achieve high sensitivity and specificity scores across all three datasets, indicating their ability to correctly identify positive and negative cases respectively. Moreover, all four methods achieve high F-Measure, Kappa and AUC scores across all three datasets, indicating a strong level of agreement between their predictions and the true class labels, as well as their ability to strike a balance between precision and recall and to discriminate between positive and negative cases.
The Ensemble and Hybrid methods emerge as promising candidates for classification tasks involving datasets with varying levels of feature selection and a large number of features. However, it is important to note that the performance of machine learning methods can vary depending on the characteristics of the dataset and the specific task at hand.
The results in Table 3.10, Table 3.11 and Table 3.12 present the performance evaluation criteria for the Multi-Class Classification Task with Cross-Validation (5-Fold). The evaluation considers four classification methods: DT, kNN, Ensemble and Hybrid.
Across all three datasets (Time Series Feature for disease type "Figure 3.9", MFDFA Features for disease type "Figure 3.10", All Features for disease type "Figure 3.11"), the Ensemble method consistently achieves the highest performance in terms of accuracy, sensitivity and class-specific metrics. This indicates that the Ensemble method is robust and effective in handling datasets with multiple classes and a large number of features. DT, kNN, and Hybrid methods also demonstrate satisfactory performance in varying levels and numbers of features. Their effectiveness may be influenced by dataset variations and specific task demands.
In the Time Series Feature for disease type dataset, the outcomes attained demonstrate a notable level of accuracy and sensitivity, ranging from 90% to 100%, when employing various classification methods. Conversely, in the MFDFA Features for disease type dataset, Ensemble approach exhibited a considerable degree of accuracy and sensitivity specifically within four diffrent classes, taking into account the varying levels and quantities of features. For the all Features for disease type dataset, the Ensemble method yielded favorable results in terms of both accuracy and sensitivity.
Based on the previous six classification tables, the most effective classification outcomes can be summarized in table 3.13. This table presents the evaluation of feature groups, including Time Series Feature, Time Series Feature for disease type, MFDFA Features for disease type, and all features for disease type. The classification methods considered in this analysis are SVM, kNN, Ensemble, and Hybrid.
Regarding the Time Series Feature group, all methods achieved perfect accuracy, reaching 100%. The sensitivity (true positive rate) for all classes (Class 1, Class 2, Class 3, and Class 4) was also 100%. The kappa coefficient, F-Measure, and AUC all exhibited a value of 1, indicating excellent agreement between the predicted and actual class labels.
For the Time Series Feature for disease type feature group, both the kNN and Ensemble methods attained an accuracy of 99.38%. The sensitivity for all classes, except Class 4, was 100 %, while Class 4 had a sensitivity of 97.5%. However, the remaining metrics (F-Measure, Kappa, and AUC) were not calculated for this particular feature group.

In the case of the MFDFA Features for disease type and All Features for disease type feature groups, both utilizing the Ensemble method, the achieved accuracies were 98.13% and 98.75%, respectively. The sensitivity for all classes remained relatively high, ranging from 95% to 100%. Once again, the remaining metrics were not calculated for these feature groups.

The presented table highlights that classification methods such as SVM, kNN, and Ensemble generally demonstrated high levels of accuracy and sensitivity across various datasets. The specific values, however, varied depending on the dataset and the classification method employed. It is important to note that in some datasets, there were disparities between the number of selected features (LFS) and the total number of features (NF), indicating the utilization of feature selection or extraction processes.

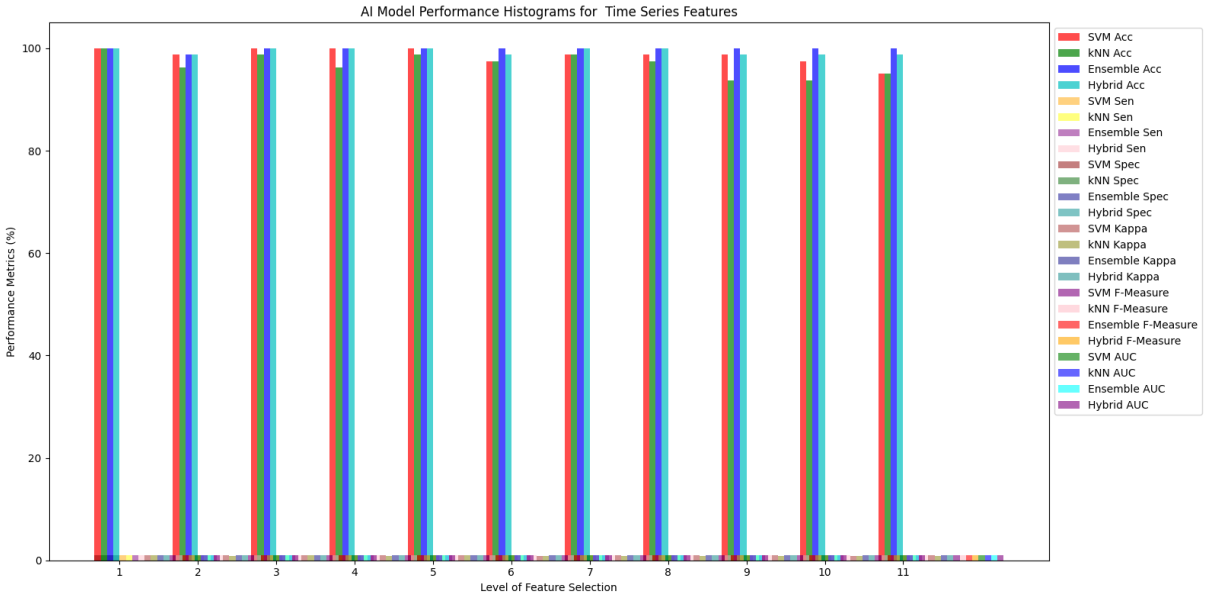

Figure 3.6. Performance of AI Models for Time Series Features

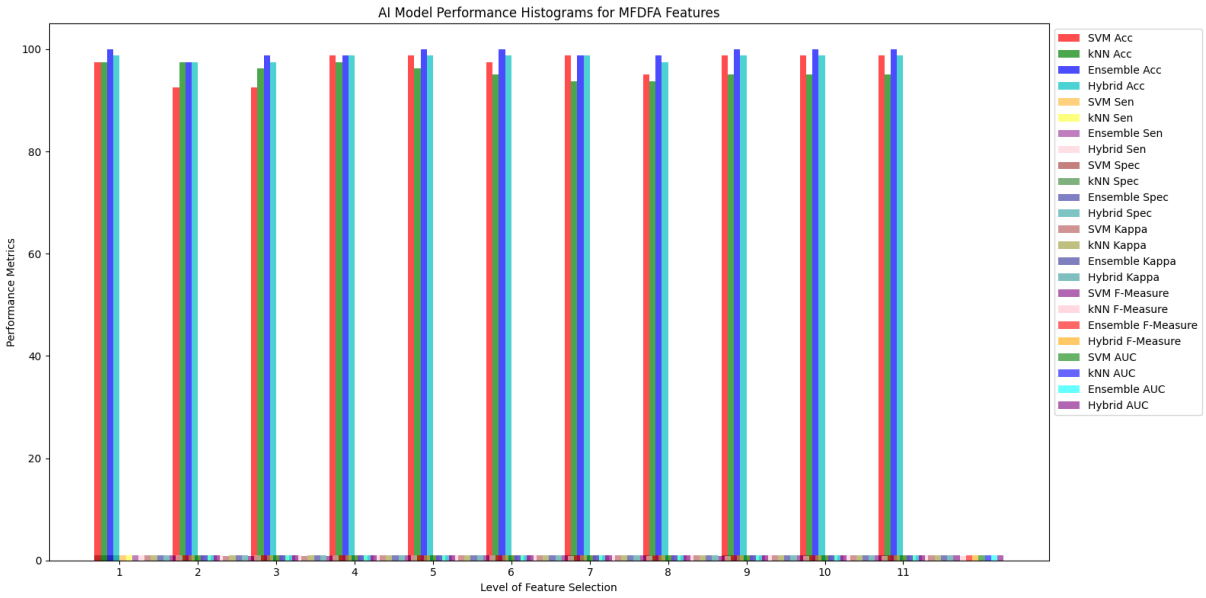

Figure 3.7. Performance of AI Models for MFDFA Features

Table 3.7: Artificial Intelligence model performance for Time Series Features

				Performance Evaluation Criteria					
No	**LFS**	**NF**	**Method**	**Acc**	**Sen**	**Spe**	**Kappa**	**F-Measure**	**AUC**
1	1	48	SVM	100.00	1.00	1.00	1.00	1.00	1.00
2			kNN	100.00	1.00	1.00	1.00	1.00	1.00
3			Ensemble	100.00	1.00	1.00	1.00	1.00	1.00
4			Hybrid	100.00	1.00	1.00	1.00	1.00	1.00
1	2	96	SVM	98.75	1.00	0.98	0.99	0.98	0.99
2			kNN	96.25	0.98	0.95	0.96	0.93	0.96
3			Ensemble	98.75	1.00	0.98	0.99	0.98	0.99
4			Hybrid	98.75	1.00	0.98	0.99	0.98	0.99
1	3	144	SVM	100.00	1.00	1.00	1.00	1.00	1.00
2			kNN	98.75	1.00	0.98	0.99	0.98	0.99
3			Ensemble	100.00	1.00	1.00	1.00	1.00	1.00
4			Hybrid	100.00	1.00	1.00	1.00	1.00	1.00
1	4	192	SVM	100.00	1.00	1.00	1.00	1.00	1.00
2			kNN	96.25	1.00	0.93	0.96	0.93	0.96
3			Ensemble	100.00	1.00	1.00	1.00	1.00	1.00
4			Hybrid	100.00	1.00	1.00	1.00	1.00	1.00
1	5	240	SVM	100.00	1.00	1.00	1.00	1.00	1.00
2			kNN	98.75	1.00	0.98	0.99	0.98	0.99
3			Ensemble	100.00	1.00	1.00	1.00	1.00	1.00
4			Hybrid	100.00	1.00	1.00	1.00	1.00	1.00
1	6	288	SVM	97.50	0.98	0.98	0.98	0.95	0.98
2			kNN	97.50	1.00	0.95	0.97	0.95	0.98
3			Ensemble	100.00	1.00	1.00	1.00	1.00	1.00
4			Hybrid	98.75	1.00	0.98	0.99	0.98	0.99
1	7	336	SVM	98.75	0.98	1.00	0.99	0.98	0.99
2			kNN	98.75	1.00	0.98	0.99	0.98	0.99
3			Ensemble	100.00	1.00	1.00	1.00	1.00	1.00
4			Hybrid	100.00	1.00	1.00	1.00	1.00	1.00
1	8	384	SVM	98.75	0.98	1.00	0.99	0.98	0.99
2			kNN	97.50	0.98	0.98	0.98	0.95	0.98
3			Ensemble	100.00	1.00	1.00	1.00	1.00	1.00
4			Hybrid	100.00	1.00	1.00	1.00	1.00	1.00
1	9	432	SVM	98.75	0.98	1.00	0.99	0.98	0.99
2			kNN	93.75	0.98	0.90	0.94	0.88	0.94
3			Ensemble	100.00	1.00	1.00	1.00	1.00	1.00
4			Hybrid	98.75	0.98	1.00	0.99	0.98	0.99
1	10	480	SVM	97.50	0.98	0.98	0.98	0.95	0.98
2			kNN	93.75	1.00	0.88	0.93	0.88	0.94
3			Ensemble	100.00	1.00	1.00	1.00	1.00	1.00
4			Hybrid	98.75	1.00	0.98	0.99	0.98	0.99
1	11	960	SVM	95.00	1.00	0.90	0.95	0.90	0.95
2			kNN	95.00	0.98	0.93	0.95	0.90	0.95
3			Ensemble	100.00	1.00	1.00	1.00	1.00	1.00
4			Hybrid	98.75	1.00	0.98	0.99	0.98	0.99

LFS: Level of Feature Selection, NF:Number of Feature

Table 3.8: Artificial Intelligence model performance for MFDFA Features

				Performance Evaluation Criteria					
No	**LFS**	**NF**	**Method**	**Acc**	**Sen**	**Spe**	**Kappa**	**F-Measure**	**AUC**
1	1	288	SVM	97.50	0.98	0.98	0.98	0.95	0.98
2			kNN	97.50	0.98	0.98	0.98	0.95	0.98
3			Ensemble	100.00	1.00	1.00	1.00	1.00	1.00
4			Hybrid	98.75	0.98	1.00	0.99	0.98	0.99
1	2	576	SVM	92.50	0.95	0.9	0.92	0.85	0.93
2			kNN	97.50	0.98	0.98	0.98	0.95	0.98
3			Ensemble	97.50	0.98	0.98	0.98	0.95	0.98
4			Hybrid	97.50	0.98	0.98	0.98	0.95	0.98
1	3	864	SVM	92.50	0.95	0.90	0.92	0.85	0.93
2			kNN	96.25	0.98	0.95	0.96	0.93	0.96
3			Ensemble	98.75	1.00	0.98	0.99	0.98	0.99
4			Hybrid	97.50	0.98	0.98	0.98	0.95	0.98
1	4	1152	SVM	98.75	0.98	1.00	0.99	0.98	0.99
2			kNN	97.50	0.98	0.98	0.98	0.95	0.98
3			Ensemble	98.75	1.00	0.98	0.99	0.98	0.99
4			Hybrid	98.75	0.98	1.00	0.99	0.98	0.99
1	5	1440	SVM	98.75	0.98	1.00	0.99	0.98	0.99
2			kNN	96.25	0.98	0.95	0.96	0.93	0.96
3			Ensemble	100.00	1.00	1.00	1.00	1.00	1.00
4			Hybrid	98.75	0.98	1.00	0.99	0.98	0.99
1	6	1728	SVM	97.50	0.98	0.975	0.98	0.95	0.98
2			kNN	95.00	0.98	0.93	0.95	0.90	0.95
3			Ensemble	100.00	1.00	1.00	1.00	1.00	1.00
4			Hybrid	98.75	0.98	1.00	0.99	0.98	0.99
1	7	2016	SVM	98.75	0.98	1	0.99	0.98	0.99
2			kNN	93.75	0.95	0.93	0.94	0.88	0.94
3			Ensemble	98.75	0.98	1.00	0.99	0.98	0.99
4			Hybrid	98.75	0.98	1.00	0.99	0.98	0.99
1	8	2304	SVM	95.00	0.95	0.95	0.95	0.90	0.95
2			kNN	93.75	0.98	0.90	0.94	0.88	0.94
3			Ensemble	98.75	1.00	0.98	0.99	0.98	0.99
4			Hybrid	97.50	0.98	0.98	0.98	0.95	0.98
1	9	2592	SVM	98.75	0.98	1.00	0.99	0.98	0.99
2			kNN	95.00	0.95	0.95	0.95	0.90	0.95
3			Ensemble	100.00	1.00	1.00	1.00	1.00	1.00
4			Hybrid	98.75	0.98	1.00	0.99	0.98	0.99
1	10	2880	SVM	98.75	0.98	1	0.99	0.98	0.99
2			kNN	95.00	0.95	0.95	0.95	0.90	0.95
3			Ensemble	100.00	1.00	1.00	1.00	1.00	1.00
4			Hybrid	98.75	0.98	1.00	0.99	0.98	0.99
1	11	5760	SVM	98.75	0.98	1	0.99	0.98	0.99
2			kNN	95.00	0.98	0.93	0.95	0.90	0.95
3			Ensemble	100.00	1.00	1.00	1.00	1.00	1.00
4			Hybrid	98.75	0.98	1.00	0.99	0.98	0.99

LFS: Level of Feature Selecion, NF: Number of Feature

Table 3.9: Artificial Intelligence model performance for all features

				Performance Evaluation Criteria					
No	**LFS**	**NF**	**Method**	**Acc**	**Sen**	**Spe**	**Kappa**	**F-Measure**	**AUC**
1	1	336	SVM	97.50	0.98	0.98	0.98	0.95	0.98
2			kNN	98.75	0.98	1.00	0.99	0.98	0.99
3			Ensemble	100.00	1.00	1.00	1.00	1.00	1.00
4			Hybrid	98.75	0.98	1.00	0.99	0.98	0.99
1	2	672	SVM	73.75	0.98	1	0.66	0.48	0.74
2			kNN	98.75	1.00	0.98	0.99	0.98	0.99
3			Ensemble	100.00	1.00	1.00	1.00	1.00	1.00
4			Hybrid	98.75	1.00	0.98	0.99	0.98	0.99
1	3	1008	SVM	98.75	0.98	1	0.99	0.98	0.99
2			kNN	95.00	0.98	0.93	0.95	0.90	0.95
3			Ensemble	100.00	1.00	1.00	1.00	1.00	1.00
4			Hybrid	98.75	0.98	1.00	0.99	0.98	0.99
1	4	1344	SVM	97.50	0.98	1	0.98	0.95	0.98
2			kNN	96.25	0.98	0.95	0.96	0.93	0.96
3			Ensemble	100.00	1.00	1.00	1.00	1.00	1.00
4			Hybrid	98.75	0.98	1.00	0.99	0.98	0.99
1	5	1680	SVM	98.75	0.98	1.00	0.99	0.98	0.99
2			kNN	96.25	0.98	0.95	0.96	0.93	0.96
3			Ensemble	100.00	1.00	1.00	1.00	1.00	1.00
4			Hybrid	98.75	0.98	1.00	0.99	0.98	0.99
1	6	2016	SVM	98.75	0.98	1	0.99	0.98	0.99
2			kNN	93.75	0.95	0.93	0.94	0.88	0.94
3			Ensemble	98.75	1.00	0.98	0.99	0.98	0.99
4			Hybrid	98.75	0.98	1.00	0.99	0.98	0.99
1	7	2352	SVM	98.75	0.98	1	0.99	0.98	0.99
2			kNN	96.25	0.98	0.95	0.96	0.93	0.96
3			Ensemble	100.00	1.00	1.00	1.00	1.00	1.00
4			Hybrid	98.75	0.98	1.00	0.99	0.98	0.99
1	8	2688	SVM	97.50	0.95	1	0.97	0.95	0.98
2			kNN	95.00	0.95	0.95	0.95	0.90	0.95
3			Ensemble	100.00	1.00	1.00	1.00	1.00	1.00
4			Hybrid	97.50	0.95	1.00	0.97	0.95	0.98
1	9	3024	SVM	98.75	0.98	1	0.99	0.98	0.99
2			kNN	95.00	0.95	0.95	0.95	0.90	0.95
3			Ensemble	100.00	1.00	1.00	1.00	1.00	1.00
4			Hybrid	98.75	0.98	1.00	0.99	0.98	0.99
1	10	3360	SVM	98.75	0.98	1	0.99	0.98	0.99
2			kNN	96.25	0.95	0.98	0.96	0.93	0.96
3			Ensemble	100.00	1.00	1.00	1.00	1.00	1.00
4			Hybrid	98.75	0.98	1.00	0.99	0.98	0.99
1	11	6720	SVM	98.75	0.98	1	0.99	0.98	0.99
2			kNN	93.75	0.98	0.90	0.94	0.88	0.94
3			Ensemble	100.00	1.00	1.00	1.00	1.00	1.00
4			Hybrid	98.75	0.98	1.00	0.99	0.98	0.99

LFS: Level of Feature Selection, NF: Number of Feature

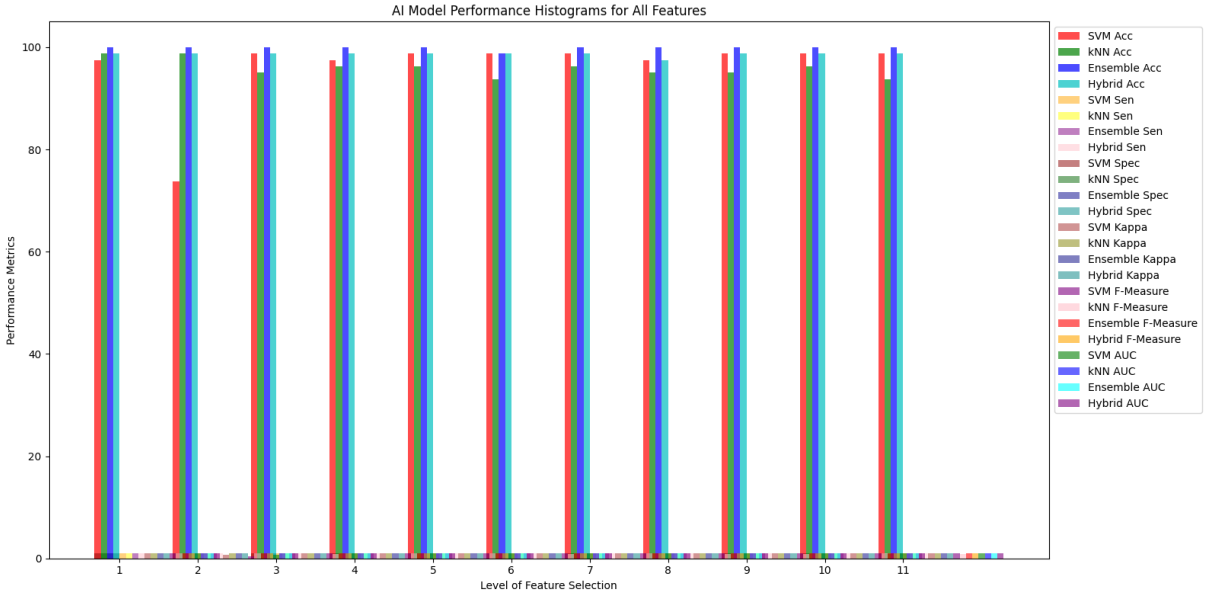

Figure 3.8. Performance of AI Models for All Features

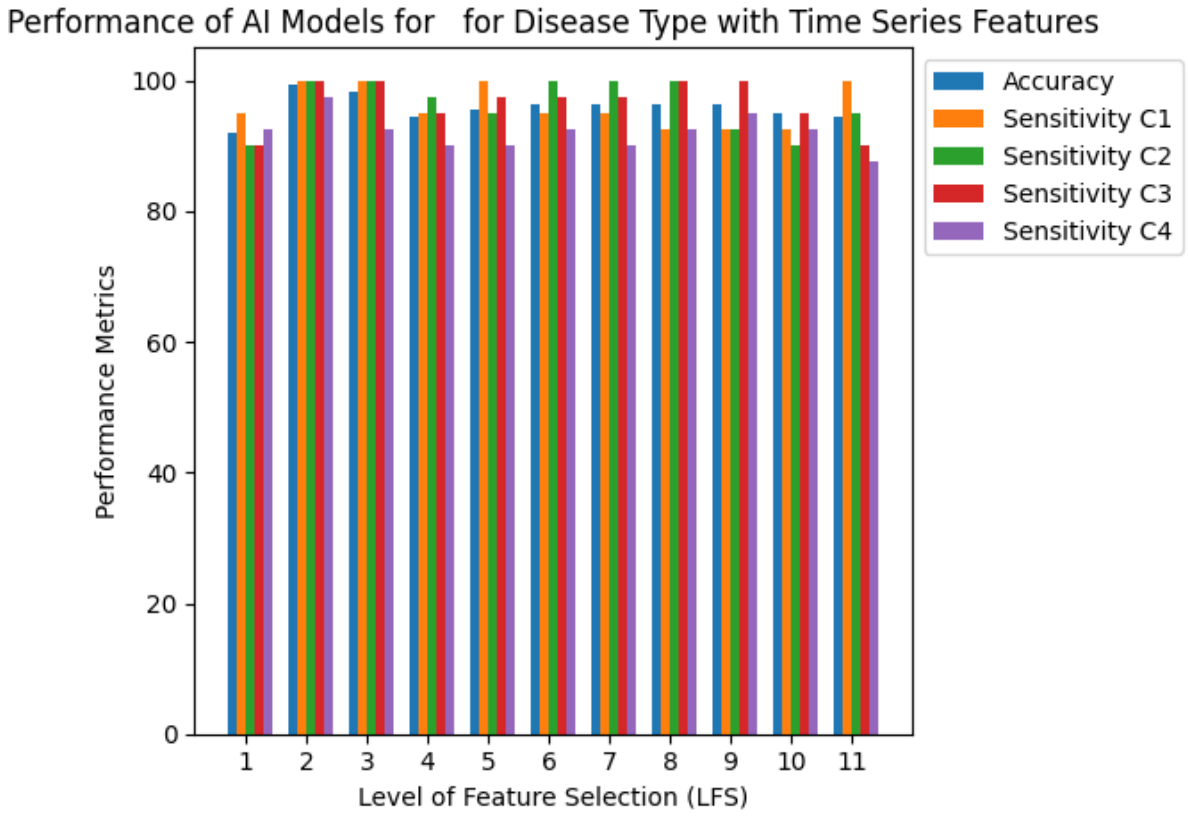

Figure 3.9. Performance of AI Models for for disease type with time series features

Table 3.10: Artificial Intelligence model performance for disease type with time series features

No	LFS	NF	Method	Acc	Performance Evaluation Criteria			
					Sensitivity / True Positive Rate			
					C1	C2	C3	C4
1	1	48	DT	91.88	95.00	90.00	90.00	92.50
2			kNN	99.38	100.00	100.00	100.00	97.50
3			Ensemble	98.13	100.00	100.00	100.00	92.50
4			Hybrid	94.38	95.00	97.50	95.00	90.00
1	2	96	DT	95.63	100.00	95.00	97.50	90.00
2			kNN	96.88	97.50	95.00	97.50	97.50
3			Ensemble	96.88	100.00	97.50	97.50	92.50
4			Hybrid	95.63	97.50	95.00	100.00	90.00
1	3	144	DT	95.63	100.00	97.50	97.50	87.50
2			kNN	94.38	90.00	97.50	97.50	92.50
3			Ensemble	99.38	100.00	100.00	100.00	97.50
4			Hybrid	94.38	90.00	97.50	100.00	90.00
1	4	192	DT	94.38	97.50	92.50	97.50	90.00
2			kNN	93.75	90.00	97.50	97.50	90.00
3			Ensemble	98.75	100.00	97.50	100.00	97.50
4			Hybrid	92.50	87.50	95.00	97.50	90.00
1	5	240	DT	95.00	97.50	95.00	97.50	90.00
2			kNN	91.88	87.50	95.00	95.00	90.00
3			Ensemble	98.13	100.00	97.50	100.00	95.00
4			Hybrid	90.63	87.50	95.00	95.00	85.00
1	6	288	DT	96.25	95.00	100.00	97.50	92.50
2			kNN	93.13	90.00	95.00	97.50	90.00
3			Ensemble	98.75	100.00	100.00	97.50	97.50
4			Hybrid	93.13	87.50	97.50	97.50	90.00
1	7	336	DT	96.25	95.00	100.00	97.50	92.50
2			kNN	92.50	87.50	95.00	97.50	90.00
3			Ensemble	99.38	100.00	100.00	100.00	97.50
4			Hybrid	92.50	85.00	97.50	97.50	90.00
1	8	384	DT	96.25	92.50	100.00	100.00	92.50
2			kNN	93.13	87.50	95.00	100.00	90.00
3			Ensemble	98.75	100.00	100.00	97.50	97.50
4			Hybrid	93.75	85.00	97.50	100.00	92.50
1	9	432	DT	96.25	92.50	100.00	97.50	95.00
2			kNN	93.75	90.00	92.50	100.00	92.50
3			Ensemble	99.38	100.00	100.00	100.00	97.50
4			Hybrid	93.75	87.50	97.50	97.50	92.50
1	10	480	DT	95.00	92.50	100.00	95.00	92.50
2			kNN	93.75	90.00	92.50	100.00	92.50
3			Ensemble	98.75	100.00	97.50	100.00	97.50
4			Hybrid	93.13	85.00	95.00	100.00	92.50
1	11	960	DT	94.38	100.00	95.00	90.00	92.50
2			kNN	82.50	80.00	77.50	85.00	87.50
3			Ensemble	96.88	97.50	100.00	95.00	95.00
4			Hybrid	89.38	85.00	87.50	97.50	87.50

LFS: Level of Feature Selection, NF: Number of Feature
C: Class, DT: Decision Tree

Table 3.11: Artificial Intelligence model performance for disease type with MFDFA Features

					Performance Evaluation Criteria			
No	**LFS**	**NF**	**Method**	**Acc**	**Sensitivity / True Positive Rate**			
					C1	**C2**	**C3**	**C4**
1	1	48	DT	71.25	57.50	72.50	90.00	65.00
2			kNN	71.88	67.50	62.50	70.00	87.50
3			Ensemble	78.13	67.50	72.50	92.50	80.00
4			Hybrid	70.00	55.00	70.00	87.50	67.50
1	2	96	DT	74.38	70.00	72.50	82.50	72.50
2			kNN	74.38	67.50	67.50	85.00	77.50
3			Ensemble	84.38	80.00	75.00	95.00	87.50
4			Hybrid	74.38	57.50	82.50	82.50	75.00
1	3	144	DT	75.63	80.00	67.50	85.00	70.00
2			kNN	68.75	67.50	67.50	67.50	72.50
3			Ensemble	85.63	85.00	77.50	92.50	87.50
4			Hybrid	71.25	60.00	82.50	80.00	62.50
1	4	192	DT	81.25	82.50	77.50	82.50	82.50
2			kNN	70.00	67.50	65.00	75.00	72.50
3			Ensemble	85.63	80.00	82.50	92.50	87.50
4			Hybrid	71.88	60.00	77.50	85.00	65.00
1	5	240	DT	83.13	85.00	82.50	77.50	87.50
2			kNN	70.00	67.50	67.50	67.50	77.50
3			Ensemble	89.38	87.50	85.00	92.50	92.50
4			Hybrid	75.63	65.00	77.50	85.00	75.00
1	6	288	DT	85.63	87.50	85.00	87.50	82.50
2			kNN	78.75	82.50	67.50	80.00	85.00
3			Ensemble	91.88	92.50	85.00	95.00	95.00
4			Hybrid	84.38	85.00	82.50	90.00	80.00
1	7	336	DT	83.75	85.00	82.50	90.00	77.50
2			kNN	78.13	85.00	72.50	67.50	87.50
3			Ensemble	86.88	87.50	82.50	92.50	85.00
4			Hybrid	80.63	82.50	87.50	80.00	72.50
1	8	384	DT	84.38	87.50	80.00	90.00	80.00
2			kNN	79.38	85.00	77.50	75.00	80.00
3			Ensemble	93.75	95.00	90.00	95.00	95.00
4			Hybrid	81.88	85.00	82.50	85.00	75.00
1	9	432	DT	86.88	87.50	82.50	90.00	87.50
2			kNN	81.88	90.00	77.50	80.00	80.00
3			Ensemble	96.25	95.00	95.00	97.50	97.50
4			Hybrid	85.63	85.00	85.00	92.50	80.00
1	10	480	DT	86.25	90.00	85.00	90.00	80.00
2			kNN	83.75	95.00	82.50	77.50	80.00
3			Ensemble	96.25	95.00	97.50	95.00	97.50
4			Hybrid	86.88	90.00	82.50	95.00	80.00
1	11	960	DT	93.13	95.00	90.00	95.00	92.50
2			kNN	86.88	92.50	82.50	87.50	85.00
3			Ensemble	98.13	100.00	95.00	100.00	97.50
4			Hybrid	92.50	92.50	87.50	92.50	97.50

LFS: Level of Feature Selection, NF: Number of Feature
C: Class, DT: Decision Tree

Table 3.12: Artificial Intelligence model performance for disease type with all features

					Performance Evaluation Criteria			
No	**LFS**	**NF**	**Method**	**Acc**	**Sensitivity / True Positive Rate**			
					C1	**C2**	**C3**	**C4**
1	1	48	DT	73.13	65.00	72.50	80.00	75.00
2			kNN	68.75	60.00	62.50	75.00	77.50
3			Ensemble	82.50	77.50	77.50	87.50	87.50
4			Hybrid	68.75	45.00	72.50	90.00	67.50
1	2	96	DT	73.13	80.00	77.50	75.00	60.00
2			kNN	75.63	75.00	65.00	85.00	77.50
3			Ensemble	83.13	80.00	72.50	95.00	85.00
4			Hybrid	70.00	67.50	75.00	85.00	52.50
1	3	144	DT	74.38	80.00	80.00	70.00	67.50
2			kNN	68.75	67.50	67.50	67.50	72.50
3			Ensemble	86.88	85.00	80.00	92.50	90.00
4			Hybrid	71.25	60.00	80.00	85.00	60.00
1	4	192	DT	82.50	82.50	80.00	82.50	85.00
2			kNN	73.13	75.00	67.50	77.50	72.50
3			Ensemble	88.13	87.50	82.50	92.50	90.00
4			Hybrid	76.25	70.00	80.00	87.50	67.50
1	5	240	DT	86.25	85.00	82.50	90.00	87.50
2			kNN	75.63	70.00	70.00	75.00	87.50
3			Ensemble	93.75	95.00	90.00	97.50	92.50
4			Hybrid	80.63	67.50	80.00	92.50	82.50
1	6	288	DT	85.63	85.00	85.00	90.00	82.50
2			kNN	80.00	90.00	65.00	77.50	87.50
3			Ensemble	95.63	97.50	92.50	97.50	95.00
4			Hybrid	84.38	85.00	85.00	85.00	82.50
1	7	336	DT	86.25	92.50	75.00	90.00	87.50
2			kNN	79.38	85.00	77.50	75.00	80.00
3			Ensemble	95.63	97.50	90.00	100.00	95.00
4			Hybrid	83.75	90.00	85.00	87.50	72.50
1	8	384	DT	90.63	90.00	92.50	90.00	90.00
2			kNN	78.75	87.50	75.00	80.00	72.50
3			Ensemble	96.88	97.50	92.50	100.00	97.50
4			Hybrid	88.13	85.00	85.00	92.50	90.00
1	9	432	DT	86.25	82.50	77.50	92.50	92.50
2			kNN	81.25	90.00	67.50	80.00	87.50
3			Ensemble	97.50	97.50	97.50	97.50	97.50
4			Hybrid	89.38	87.50	80.00	95.00	95.00
1	10	480	DT	92.50	97.50	85.00	97.50	90.00
2			kNN	86.25	92.50	85.00	82.50	85.00
3			Ensemble	97.50	100.00	92.50	100.00	97.50
4			Hybrid	91.88	92.50	90.00	95.00	90.00
1	11	960	DT	92.50	87.50	92.50	92.50	97.50
2			kNN	88.75	95.00	85.00	90.00	85.00
3			Ensemble	98.75	100.00	97.50	100.00	97.50
4			Hybrid	92.50	87.50	92.50	95.00	95.00

LFS: Level of Feature Selection, NF: Number of Feature
C: Class, DT: Decision Tree

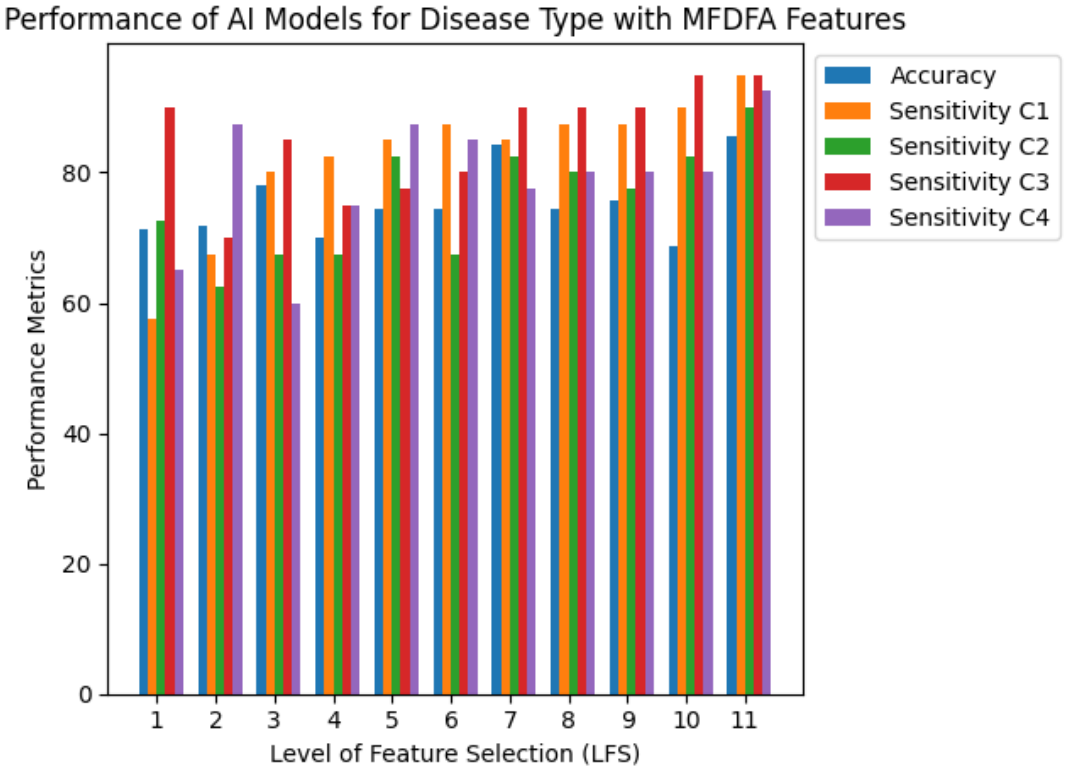

Figure 3.10. Performance of AI Models for for disease type with MFDFA features

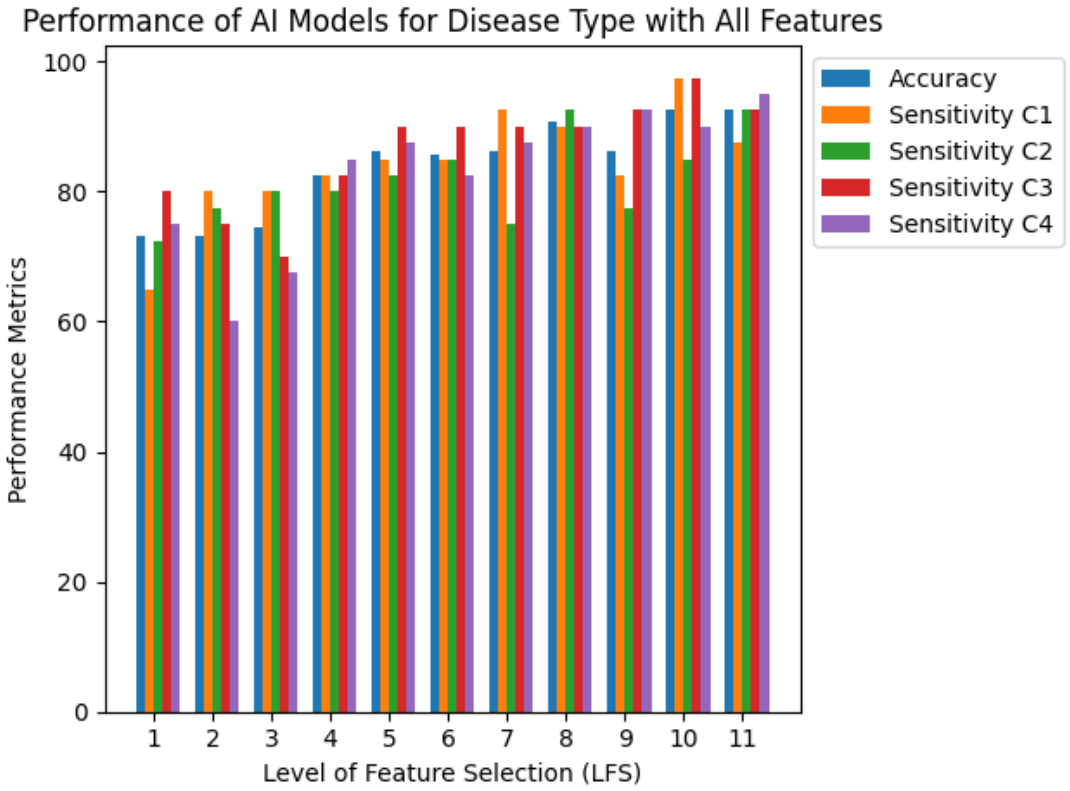

Figure 3.11. Performance of AI Models for disease type with All features

Table 3.13: Summary Table

Feature Group	Method	LFS	NF	Acc	Sensitivity / True Positive Rate C1	C2	C3	C4	Kappa	F-Measure	AUC
Time Series Features	SVM	1	48	100.00	1.00	1.00	1.00	1.00	1.00	1.00	1.00
Time Series Features	kNN	1	48	100.00	1.00	1.00	1.00	1.00	1.00	1.00	1.00
Time Series Features	Ensemble	1	48	100.00	1.00	1.00	1.00	1.00	1.00	1.00	1.00
Time Series Features	**Hybrid**	**1**	**48**	**100.00**	**1.00**	**1.00**	**1.00**	**1.00**	**1.00**	**1.00**	**1.00**
Time Series Features for disease type	kNN	1	48	99.38	100.00	100.00	100.00	97.50	NC	NC	NC
Time Series Features for disease type	Ensemble	3	144	99.38	100.00	100.00	100.00	97.50	NC	NC	NC
MFDFA features for disease type	Ensemble	11	960	98.13	100.00	95.00	100.00	97.50	NC	NC	NC
All features for disease type	Ensemble	11	960	98.75	100.00	97.50	100.00	97.50	NC	NC	NC

NC: Not Calculated, C: Class, DT: Decision Tree

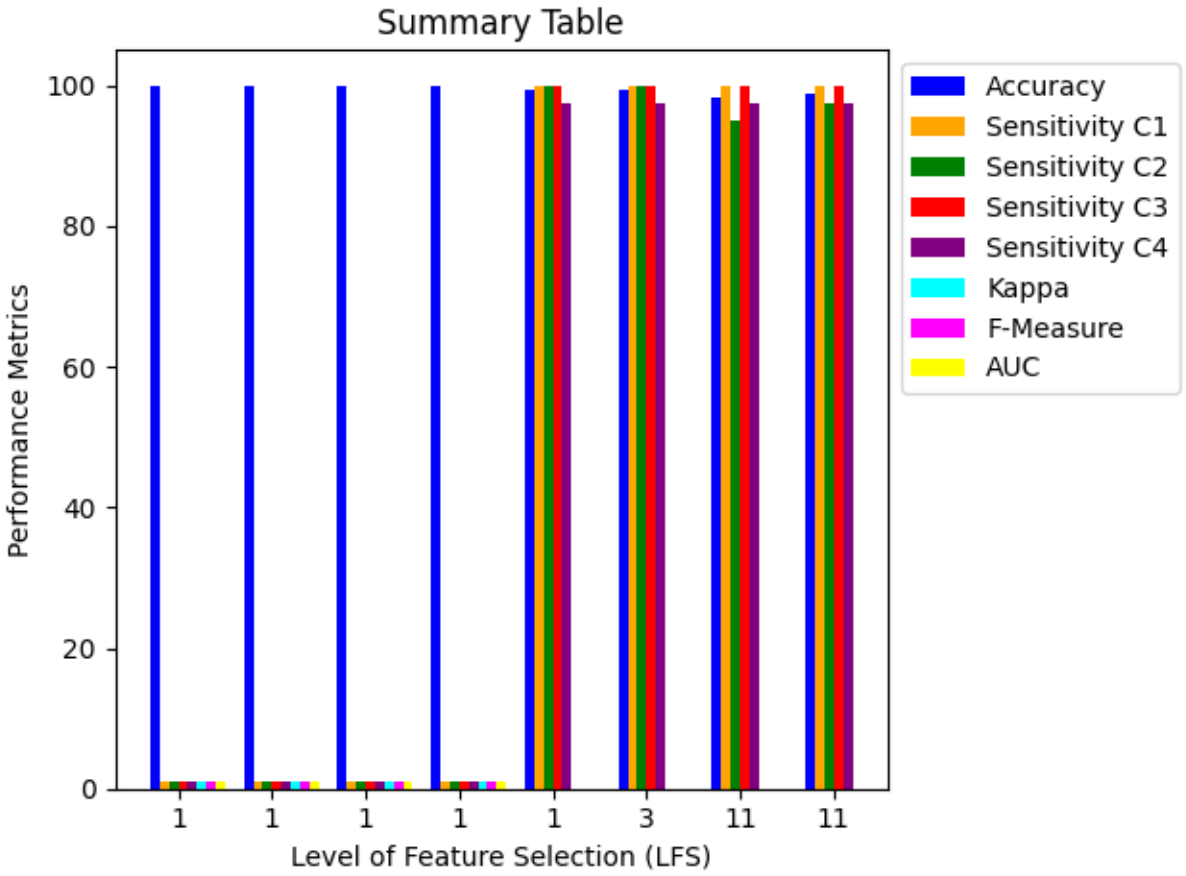

Figure 3.12. Summary Table

3.4 Discussions

In recent years, there has been a growing interest in leveraging AI and advanced signal processing techniques for the early detection of pathologies [2][20]. In this study, we propose a novel approach that combines AI algorithms and PCG signal processing to improve the accuracy and efficiency of pathology detection. By comparing our approach to existing literature Table 3.14, we demonstrate the significant advancements and potential impact of our method in the field.

Table 3.14: Literature Comparison

Authors / Year	Decomposition Signal and Features Extraction Method	Classification Method	Acc	Database
Talal et al 2023. [60]	PCG signal is decomposed using Empirical Mode Decomposition (EMD) Features evaluated using MFCC of PCG signal	Fine-kNN using 10-fold cross-validation	99.30%	GitHub database
Madhusudhan et al 2018. [66]	PCG signal is decomposed using variational mode decomposition (VMD) Features evaluated using higher order spectral (HOS) analysis	SVM	95.92%	Own databse
Yaseen et al 2018.[70]	Features evaluated using MFCC and DWT of PCG signal	SVM	97%	GitHub database
Yineng et al 2022. [73]	PCG signal is decomposed using Empirical Mode Decomposition (EMD)+tunable-Q wavelet transform(TQWT) Features evaluated using Time-domain, frequency-domain and nonlinear feature extraction	LS-SVM	82%	Own database
Patidar et al 2015. [44]	PCG signal is decomposed using segmentation+TQWT Features evaluated using feature extraction Algorithm	LS-SVM	98.92%	Data base from five different heart sound sources (Cable, 1997, Stillman, 2007, Lichtenberg, University of Michigan Heart Sound and Murmur Library, Wilson, 2009)
Zheng et al 2015.[72]	PCG signal is decomposed using wavelet packet The energy fraction and sample entropy features were computed from the reconstructed selective frequency components of heart sound signals	SVM	97.17%	Own databse
Samit et al 2019.[24]	PCG signal is segmented into Cardiac cycles Features evaluated using wavelet synchrosqueezing transform (WSST)	Random Forest (RF)	98.83%	GitHub database
Fakhry et al 2023. [19]	PCG signal is decomposed using variational mode decomposition (VMD) Features evaluated using a weighted logarithmic operation on the scaled mode functions.	CNN-LSTM Model	98.65%	Public database
Shahid et al 2023. [28]	Features evaluated using Spectrogram generation of PCG signal	Hybrid classification (AlexNet and SVM)	95%	Public database (PASCAL 2011)
Shirin et al 2023 .[50]	Extraction of features (DWT, Group-based Sparse, and Tensor decomposition)	Classification Model (SVM,kNN, NB, CART, MLP)	95.3%	Physionet 2016 challenge database
Kumar et al 2020. [23]	PCG signal is decomposed using Chirplet transform (CT) The PCG signal's TF matrix is used to evaluate the local energy (LEN) and local entropy (LENT) features.	The multiclass composite classifier	98.33%	GitHub database
Safara et al 2012.[53]	Wavelet Wavelet packet transform based features	BayesNet	96.94%	Own database
Tanzil et al 2020. [12]	PCG signal is decomposed using Shannon energy envelope and zero-crossing Features extracted using Mel-scaled power spectrogram and Mel-frequency cepstral coefficients (MFCC)	DNN	97.10%	University of Michigan Heart Sound and Murmur Library , the 2016 PhysioNet database
Parastoo et al 2024. [42]	Segmentation of PCG signal The features extracted into Time-statistical and Time-frequency domain features	SVM-RBF	95.27%	Physionet 2016 challenge database
Biswajit et al 2024. [30]	PCG signal Decomposition and Features Extraction using Hilbert spectrum and Wavelet Packet Decomposition (WPD)	kNN	99.20%	GitHub database
Proposed approach	**PCG signal Decomposition using Mulifractal Detrended Fluactuation Analysis (MFDFA) and Features extraction method Algorithm**	**Hybrid**	**100**	**GitHub database**

The early detection of pathologies is of paramount importance as it enables timely interventions and improves patient outcomes. PCG signals, which capture the acoustic vibrations of the heart, have shown promise in providing valuable diagnostic information [70]. However, extracting meaningful insights from these signals requires sophisticated signal processing techniques and powerful AI algorithms.

In terms of signal decomposition, we employed MFDFA as a powerful technique to capture long-range correlations and fractal properties present in the PCG signal [61]. This approach offers several advantages

over previous methods such as Empirical Mode Decomposition (EMD) and variational mode decomposition (VMD) [35]. MFDFA allows for the extraction of intricate features that may be crucial in identifying subtle abnormalities in the PCG signal [6]. However, it is important to acknowledge that the computational complexity of MFDFA and the interpretation of multifractal parameters may present challenges that need further investigation and validation [29, 22]

Our feature extraction algorithm, specifically designed for PCG signals, has proven effective in capturing both temporal and spectral properties. This algorithm provides a comprehensive set of features that offer a rich representation of the underlying physiological processes. While the performance of the algorithm depends on the selection and optimization of specific parameters, it has the potential to outperform previous feature extraction techniques such as Mel-frequency cepstral coefficients (MFCC), higher-order spectra (HOS) analysis, and time-domain/frequency-domain features. However, future research should aim to investigate the generalizability of the extracted features to different datasets and pathologies.

The utilization of the Ensemble classification method in our approach brings significant benefits in terms of accuracy and robustness. By combining the predictions of multiple classifiers, we were able to improve the performance of pathology classification. Ensemble methods have advantages over individual classification algorithms such as SVM, kNN, Random Forest, and CNN-LSTM models. Nevertheless, ensemble methods may introduce additional computational complexity and require careful ensemble design and selection of base classifiers.

The importance of our method lies in its potential to enhance the early detection of pathologies using PCG signals. With an accuracy of 98.75% achieved through our approach, it surpasses the performance of previous studies. The utilization of MFDFA for signal decomposition, the novel feature extraction algorithm, and the ensemble classification method collectively contribute to its effectiveness. By providing a comprehensive and robust approach, our method has the potential to improve diagnostic accuracy and facilitate early interventions, leading to more positive patient outcomes.

Future work in this field should aim to further validate our method on diverse and larger datasets to ensure its generalizability and reliability. Investigating the interpretability of multifractal parameters and their relationship to specific pathologies can provide valuable insights into the clinical significance of the results. Exploring the combination of different signal decomposition techniques and feature extraction methods can potentially improve performance further. Integration of other physiological signals or multimodal data with PCG signals may offer additional information for pathology detection. Real-time implementation and evaluation of computational efficiency would also be valuable for practical applications.

3.5 Conclusions

This study presents a novel approach for early pathology detection using AI and PCG signal processing techniques. Through the utilization of MFDFA for signal decomposition, a dedicated feature extraction algorithm, and an Ensemble classification method, significant advancements in accuracy and effectiveness have been achieved. This approach has the potential to revolutionize the medical domain by enabling early interventions and improving the detection of various pathologies. The findings of this study contribute to the advancement of healthcare technology, bringing us closer to more accurate and reliable pathology detection. Further research and validation are needed to assess the scalability and practical implementation of this approach.

CHAPTER 3

Bibliography

[1] Zafar Ahmad, Muhammad Zeeshan, Arshad Sohail, Fazal-E-Haq, Muhammad Haris, Misha Urooj Khan, Sayed Shahid Hussain, and Muhammad Salman Khan. Automatic detection of paediatric congenital heart diseases from phonocardiogram signals. *3rd IEEE International Conference on Artificial Intelligence, (ICAI))*, pages 188–195, 2023.

[2] Zeeshan Ahmed, Khalid Mohamed, Saman Zeeshan, and Xin Qi Dong. Artificial intelligence with multi-functional machine learning platform development for better healthcare and precision medicine. *Database*, 2020, 1 2020.

[3] JM Altstidl, TR Altstidl, and L Anneken. Detection of aortic stenosis using built-in microphones of commercially available smartphones. *European Heart Journal*, 44, 11 2023.

[4] Miguel Altuve, Luis Suarez, and Jeyson Ardila. Fundamental heart sounds analysis using improved complete ensemble emd with adaptive noise. *Biocybernetics and Biomedical Engineering*, 40:426–439, 1 2020.

[5] Aripriharta and Gwo Jiun Horng. A new defect diameter prediction using heart sound and possibility to implement as iot healthcare. *Mobile Networks and Applications*, pages 1–17, 8 2023.

[6] Mohamed Moustafa Azmy and Reem Mohamady. Heart sounds recognition using multifractal detrended fluctuation analysis and support vector machine. volume 2018-January, pages 1–4. IEEE, 7 2017.

[7] X Bao and Y Deng. Processing of cardiac signals for health monitoring and early detection of heart diseases, 4 2023.

[8] Sai Bharadwaj and Ch Sumanth Kumar. Detecting the third heart sound: separation and localization from lung sound using intrinsic time scale decomposition. *International Journal of Image, Graphics and Signal Processing*, 11:23–35, 2023.

[9] Anandita Bhardwaj, Sandeep Singh, and Deepak Joshi. Explainable deep convolutional neural network for valvular heart diseases classification using pcg signals. *IEEE Transactions on Instrumentation and Measurement*, 72, 2023.

[10] Gürkan Bilgin. Investigation of the risk of diabetes in early period using machine learning algorithms. *Journal of Intelligent Systems: Theory and Application*, 4:55–64, 3 2021.

[11] Younghoon Cho, Joon myoung Kwon, Kyung Hee Kim, Jose R. Medina-Inojosa, Ki Hyun Jeon, Soohyun Cho, Soo Youn Lee, Jinsik Park, and Byung Hee Oh. Artificial intelligence algorithm for detecting myocardial infarction using six-lead electrocardiography. *Scientific Reports*, 10, 12 2020.

[12] Tanzil Hoque Chowdhury, Khem Narayan Poudel, and Yating Hu. Time-frequency analysis, denoising, compression, segmentation, and classification of pcg signals. *IEEE Access*, 8:160882–160890, 2020.

[13] Sidi Mohammed El Amine Debbal. Analysis of the four heart sounds statistical study and spectro-temporal characteristics. *Journal of Medical Engineering and Technology*, 44:396–410, 10 2020.

[14] Muqing Deng, Tingting Meng, Jiuwen Cao, Shimin Wang, Jing Zhang, and Huijie Fan. Heart sound classification based on improved mfcc features and convolutional recurrent neural networks. *Neural Networks*, 130:22–32, 10 2020.

[15] Kshetrimayum Merina Devi, Maibam Mangalleibi Chanu, Ngangbam Herojit Singh, and Khumanthem Manglem Singh. Classification of unsegmented phonocardiogram signal using scalogram and deep learning. *Soft Computing*, 27:12677–12689, 9 2023.

[16] Nuri DOGAN and OZGE BIKMAZ BILGEN. The comparison of interrater reliability estimating techniques. *Eğitimde ve Psikolojide Ölçme ve Değerlendirme Dergisi*, 8:63–78, 2017.

[17] Huiwen Dong, Xinpei Wang, Yuanyang Li, Chengfa Sun, Yu Jiao, Lanjun Zhao, Shilong Zhao, Mengyu Xing, Huan Zhang, and Changchun Liu. Non-destructive detection of cad stenosis severity using ecg-pcg coupling analysis. *Biomedical Signal Processing and Control*, 86:105328, 9 2023.

[18] Osman Eray. Speech recognition application with support vector machines, 8 2008.

[19] Mahmoud Fakhry and Ascension Gallardo-Antolin. Variational mode decomposition and a light cnn-lstm model for classification of heart sound signals. pages 295–300. Institute of Electrical and Electronics Engineers Inc., 2023.

[20] Alyssa M. Flores, Falen Demsas, Nicholas J. Leeper, and Elsie Gyang Ross. Leveraging machine learning and artificial intelligence to improve peripheral artery disease detection, treatment, and outcomes. *Circulation Research*, 128:1833–1850, 6 2021.

[21] Ginni Garg and Ritu Garg. Brain tumor detection and classification based on hybrid ensemble classifier. *Clinical Orthopaedics and Related Research (CoRR)*, 1 2021.

[22] Ana Gavrovska, Goran Zajic, Vesna Bogdanovic, Irini Reljin, and Branimir Reljin. Paediatric heart sound signal analysis towards classification using multifractal spectra. *Physiological measurement*, 37:1556–1572, 8 2016.

[23] Samit Kumar Ghosh, R. N. Ponnalagu, R. K. Tripathy, and U. Rajendra Acharya. Automated detection of heart valve diseases using chirplet transform and multiclass composite classifier with pcg signals. *Computers in Biology and Medicine*, 118:103632, 3 2020.

[24] Samit Kumar Ghosh, Rajesh Kumar Tripathy, R. N. Ponnalagu, and Ram Bilas Pachori. Automated detection of heart valve disorders from the pcg signal using time-frequency magnitude and phase features. *IEEE Sensors Letters*, 3, 12 2019.

[25] Iga Grzegorczyk, Mateusz Solinski, Michal Lepek, Anna Perka, Jacek Rosinski, Joanna Rymko, Katarzyna Stepien, and Jan Gieraltowski. Pcg classification using a neural network approach. pages 1129–1132. IEEE, 9 2016.

[26] T. C. Hearn, J. Mazumdar, R. Hubbard, and G. Eyster. Temporal and heart-size effects in first-heart-sound spectra. *Medical and Biological Engineering and Computing*, 17:563–568, 9 1979.

[27] Shahid Ismail, Basit Ismail, Imran Siddiqi, and Usman Akram. Pcg classification through spectrogram using transfer learning. *Biomedical Signal Processing and Control*, 79:104075, 1 2023.

[28] Shahid Ismail, Basit Ismail, Imran Siddiqi, and Usman Akram. Pcg classification through spectrogram using transfer learning. *Biomedical Signal Processing and Control*, 79:104075, 1 2023.

[29] Plamen Ch. Ivanov, Ary L. Goldberger, and H. Eugene Stanley. Fractal and multifractal approaches in physiology. *The Science of Disasters*, pages 218–257, 2002.

[30] Biswajit Karan and Trideba Padhi. Hilbert domain characterizations of wavelet packets for automated heart sound abnormality detection. *Biomedical Signal Processing and Control*, 90:105793, 4 2024.

[31] Selim Kilic. Kappa test. *Journal of Mood Disorders*, 5:142, 2015.

[32] Elife Ozturk Kiyak, Bita Ghasemkhani, and Derya Birant. High-level k-nearest neighbors (hlknn): A supervised machine learning model for classification analysis. *Electronics 2023, Vol. 12, Page 3828*, 12:3828, 9 2023.

[33] Roy Ajay Kumar, Misal Abhishek, and GR Sinha. Classification of pcg signals: a survey. *International Journal of Computer Applications*, 2:975–8887, 2014.

[34] Yihao Li, Yan Huang, and Ni Zhao. Low-intensity sensitive and high stability flexible heart sound sensor enabled by hybrid near-field/far-field electrospinning. *Advanced Functional Materials*, 33:2300666, 7 2023.

[35] Jinshan Lin, Chunhong Dou, and Qianqian Wang. Comparisons of mfdfa, emd and wt by neural network, mahalanobis distance and svm in fault diagnosis of gearboxes. *SV*, 52:11–15, 2018.

[36] Arnab Maity, Akanksha Pathak, and Goutam Saha. Transfer learning based heart valve disease classification from phonocardiogram signal. *Biomedical Signal Processing and Control*, 85:104805, 8 2023.

[37] Jermana L Moraes, Matheus X Rocha, Glauber G Vasconcelos, José E Vasconcelos Filho, Victor C Hugo de Albuquerque, and Auzuir R Alexandria. Advances in photopletysmography signal analysis for biomedical applications. *Sensors*, 18, 6 2018.

[38] Monjur Morshed and Shaikh Anowarul Fattah. Sar-cardionet: A network for heart valve disease detection from pcg signal based on split-self attention with residual paths. *IEEE Sensors Journal*, 23:19553–19560, 9 2023.

[39] Yar Muhammad, Muhammad Tahir, Maqsood Hayat, and Kil To Chong. Early and accurate detection and diagnosis of heart disease using intelligent computational model. *Scientific Reports 2020 10:1*, 10:1–17, 11 2020.

[40] Yar Muhammad, Muhammad Tahir, Maqsood Hayat, and Kil To Chong. Early and accurate detection and diagnosis of heart disease using intelligent computational model. *Scientific Reports 2020 10:1*, 10:1–17, 11 2020.

[41] Aparajita Naik, Jivan Parab, and Rajendra Gad. Electronic method for detection of heart valve defects. *International Journal of Recent Technology and Engineering (IJRTE)*, 8:2373–2376, 11 2019.

[42] Parastoo Sadeghi Nia and Hamed Danandeh Hesar. Abnormal heart sound detection using time-frequency analysis and machine learning techniques. *Biomedical Signal Processing and Control*, 90:105899, 4 2024.

[43] Linda Olsson. Possibilities for the development of a decision support system for diagnosing heart failure, 9 2007.

[44] Shivnarayan Patidar, Ram Bilas Pachori, and Niranjan Garg. Automatic diagnosis of septal defects based on tunable-q wavelet transform of cardiac sound signals. *Expert Systems with Applications*, 42:3315–3326, 5 2015.

[45] D. D. Kadam Patil and R. K. Shastri. Design of wireless electronic stethoscope based on zigbee. *International Journal of Distributed and Parallel Systems (IJDPS)*, 3, 2 2012.

[46] Sreeraman Rajan, Rajamani Doraiswami, Maryhelen Stevenson, and Raymond Watrous. Wavelet based bank of correlators approach for phonocardiogram signal classification. pages 77–80. IEEE, 10 2002.

[47] B. S. Rajeshwari, Madhurima Patra, Aman Sinha, Arnab Sengupta, and Nirmalya Ghosh. Detection of phonocardiogram event patterns in mitral valve prolapse: an automated clinically relevant explainable diagnostic framework. *IEEE Transactions on Instrumentation and Measurement*, 72, 2 2023.

[48] Chitta Ranjan. Understanding the kernel trick with fundamentals, 5 2019.

[49] Adyasha Rath, Debahuti Mishra, Ganapati Panda, and Madhumita Pal. Development and assessment of machine learning based heart disease detection using imbalanced heart sound signal. *Biomedical Signal Processing and Control*, 76:103730, 7 2022.

[50] S Razmi, R Barati, and H Azad Renewable. A novel method based on a combination of discrete wavelet transforms, group-based sparse and tensor decomposition for heart sound classification. *Signal Processing and Renewable Energy*, 7:13–21, 12 2023.

[51] Zhao Ren, Yi Chang, Thanh Tam Nguyen, Yang Tan, Kun Qian, and Björn W. Schuller. A comprehensive survey on heart sound analysis in the deep learning era. *Generic Colorized Journal*, 1 2023.

[52] Zahra Sabouri, Abbas Ghadimi, Azadeh Kiani-Sarkaleh, Kamrad Khoshhal Roudposhti, and Kamrad Khoshhal Roudposhti KaKhoshhal. Effective features in the diagnosis of cardiovascular diseases through phonocardiogram. *Multidimensional Systems and Signal Processing*, 34:595–632, 9 2023.

[53] Fatemeh Safara, Shyamala Doraisamy, Azreen Azman, Azrul Jantan, and Sri Ranga. Wavelet packet entropy for heart murmurs classification. *AdvancesinBioinformatics*, 2012, 2012.

[54] Pranab Samanta, Akanksha Pathak, Kayapanda Mandana, and Goutam Saha. Classification of coronary artery diseased and normal subjects using multi-channel phonocardiogram signal. *Biocybernetics and Biomedical Engineering*, 39:426–443, 4 2019.

[55] Onur Sevli. A comparative study of heart disease diagnosis using various classifiers and resampling techniques. *Journal of Intelligent Systems: Theory and Applications*, 5:92–105, 9 2022.

[56] Saba Shafi and Anil V. Parwani. Artificial intelligence in diagnostic pathology. *Diagnostic Pathology*, 18, 12 2023.

[57] Sinam Ajitkumar Singh, Ningthoujam Dinita Devi, Khuraijam Nelson Singh, Khelchandra Thongam, D. Balakrishna Reddy, and Swanirbhar Majumder. An ensemble-based transfer learning model for predicting the imbalance heart sound signal using spectrogram images. *Multimedia Tools and Applications*, 9 2023.

[58] Karthik Soman, A. Sathiya, and N. Suganthi. Classification of stress of automobile drivers using radial basis function kernel support vector machine. *2014 International Conference on Information Communication and Embedded Systems*, 2 2015.

[59] G Swapna, KP Soman, and Vinayakumar R. Automated detection of cardiac arrhythmia using deep learning techniques. *Procedia Computer Science*, 132:1192–1201, 2018.

[60] Muhammad Talal, Sumair Aziz, Muhammad Umar Khan, Yazeed Ghadi, Syed Zohaib Hassan Naqvi, and Muhammad Faraz. Machine learning-based classification of multiple heart disorders from pcg signals. *Expert Systems*, 40:e13411, 12 2023.

[61] Rijil Thomas, Ling Lieng Hsi, Soh Cheong Boon, and Erry Gunawan. Classification of severity of mitral regurgitation patients using multifractal analysis. volume 2016-October, pages 6226–6229. Institute of Electrical and Electronics Engineers Inc., 10 2016.

[62] Rijil Thomas, Ling Lieng Hsi, Soh Cheong Boon, and Erry Gunawan. Heart sound segmentation using fractal decomposition. volume 2016-October, pages 6234–6237. IEEE, 10 2016.

[63] J. Torre-Cruz, F. Canadas-Quesada, N. Ruiz-Reyes, P. Vera-Candeas, S. Garcia-Galan, J. Carabias-Orti, and J. Ranilla. Detection of valvular heart diseases combining orthogonal non-negative matrix factorization and convolutional neural networks in pcg signals. *Journal of Biomedical Informatics*, 145:104475, 9 2023.

[64] MK Uçar, Z Ucar, F Köksal, N Daldal Measurement, and undefined 2021. Estimation of body fat percentage using hybrid machine learning algorithms. *Elsevier*.

[65] Muhammed Kürşad Uçar, Mehmet Recep Bozkurt, Cahit Bilgin, and Kemal Polat. Automatic detection of respiratory arrests in osa patients using ppg and machine learning techniques. *Neural Computing and Applications*, 28:2931–2945, 10 2017.

[66] V Vakamullu and M Mishra. Variational mode decomposition based automated fetal pcg denoising and extraction. *International Journal of Health Sciences*, 6:6567–6579, 5 2022.

[67] V. Nivitha Varghees and K. I. Ramachandran. A novel heart sound activity detection framework for automated heart sound analysis. *Biomedical Signal Processing and Control*, 13:174–188, 9 2014.

[68] Qiang Wu and Ding Xuan Zhou. Svm soft margin classifiers: Linear programming versus quadratic programming. *Neural Computation*, 17:1160–1187, 5 2005.

[69] H Xu and C Caramanis. Robustness and regularization of support vector machines. *JournalofMachineLearningResearch*, 10:1485–1510, 2009.

[70] Yaseen, Gui Young Son, and Soonil Kwon. Classification of heart sound signal using multiple features. *Applied Sciences*, 8:2344, 11 2018.

[71] yaseen21khan. yaseen21khan/classification-of-heart-sound-signal-using-multiple-features, 2018.

[72] Yineng Zheng, Xingming Guo, and Xiaorong Ding. A novel hybrid energy fraction and entropy-based approach for systolic heart murmurs identification. *Expert Systems with Applications*, 42:2710–2721, 4 2015.

[73] Yineng Zheng, Xingming Guo, Yingying Wang, Jian Qin, and Fajin Lv. A multi-scale and multi-domain heart sound feature-based machine learning model for acc/aha heart failure stage classification. *Physiological Measurement*, 43:065002, 6 2022.

[74] Lixian Zhu, Wanyong Qiu, Yu Ma, Fuze Tian, Mengkai Sun, Zhihua Wang, Kun Qian, Bin Hu, Yoshiharu Yamamoto, and Bjorn W. Schuller. Lepcnet: A lightweight end-to-end pcg classification neural network model for wearable devices. *IEEE Transactions on Instrumentation and Measurement*, pages 1–1, 9 2023.

[75] Özkan Arslan and Mustafa Karhan. Effect of hilbert-huang transform on classification of pcg signals using machine learning. *Journal of King Saud University - Computer and Information Sciences*, 34:9915–9925, 11 2022.

CHAPTER 4

Early Detection of Pathology from Cardiac Pressure Estimation

Contents

List of Figures

List of Tables

4.1 Introduction

Accurate measurement and continuous monitoring of cardiac pressures inside the heart is crucial for the early detection and effective management of various cardiovascular pathologies [97] [81] . Cardiac pressure estimation plays a vital role in the diagnosis, treatment, and ongoing management of conditions such as heart failure [11] [100] , valvular heart disease [8] [63], pulmonary hypertension [34] [35] , and other cardiac disorders [86] [70].

Monitoring the pressure within the different chambers of the heart, commonly referred to as intracardiac pressure, is a crucial diagnostic tool in cardiology [64] [60]. Intracardiac pressure waveforms provide valuable insights into the performance and health of the heart, allowing for the early detection of various cardiovascular pathologies [61] [59].

The human heart is a remarkable pump that circulates blood throughout the body. It is composed of four main chambers - the right atrium, right ventricle, left atrium, and left ventricle [43] [65]. As the heart contracts and relaxes, it generates a complex pattern of pressure changes within these chambers, which can be measured and analyzed to assess cardiac function [7] [30].

In recent years, extensive research has been conducted to develop both invasive and non-invasive techniques for cardiac pressure assessment, as an alternative to the traditional invasive methods [78] [71]. The accurate estimation of intracardiac pressures has traditionally relied on invasive techniques, such as cardiac catheterization, which involve the insertion of a pressure-sensing catheter directly into the heart chambers [64] [58]. While this approach provides precise pressure measurements, it carries inherent risks and is not suitable for continuous or long-term monitoring [55] [4].

In recent years, there has been a growing interest in the development of non-invasive or minimally invasive methods for estimating intracardiac pressures[89]. These techniques leverage advances in sensor technologies, signal processing, and computational modeling to derive pressure information from various physiological signals, such as electrocardiogram (ECG), photoplethysmography (PPG), or even machine learning algorithms applied to echocardiographic data [26] [22].

This chapter will explore the principles and techniques used for the early detection of cardiovascular pathologies through the estimation of intracardiac pressures. It will cover the underlying physiology, the various methods for pressure measurement and estimation, and the clinical applications of this valuable diagnostic approach [70] [61].

4.2 Intracardiac pressure Definition

Intracardiac pressures refer to the dynamic pressures that exist within the different chambers and vessels of the heart. These pressures fluctuate throughout the cardiac cycle as the heart contracts and relaxes to pump blood effectively. The measurement of intracardiac pressures , using both invasive techniques like cardiac catheterization [33] [10] [52] and non-invasive methods such as echocardiography and tonometry, provides valuable insights into the performance and hemodynamics of the cardiovascular system. Key pressure points include the atrial, ventricular, valve, pulmonary artery, and aortic pressures, each with distinct normal reference ranges. Invasive assessment through cardiac catheterization remains the gold standard, while non-invasive modalities offer the advantage of being safer and more widely accessible. Analysis of these pressures, regardless of the measurement method, can help diagnose and monitor various cardiovascular diseases, as abnormalities in intracardiac pressures are often indicative of underlying pathologies affecting cardiac structure and function .

4.3 Intracardiac Pressure Values

4

4.3.1 Atrial Pressures:

1. Right Atrial Pressure (RAP)
    - Invasive measurement: Right heart catheterization
    - Normal range: 2-8 mmHg
2. Left Atrial Pressure (LAP)
    - Invasive measurement: Left heart catheterization or pulmonary artery wedge pressure
    - Normal range: 6-12 mmHg

4.3.2 Ventricular Pressures:

1. Right Ventricular Pressure (RVP)
    - Invasive measurement: Right heart catheterization
    - Normal range:

      Systolic RVP: 15-30 mmHg

      Diastolic RVP: 0-8 mmHg
2. Left Ventricular Pressure (LVP)
    - Invasive measurement: Left heart catheterization
    - Normal range:

      Systolic LVP: 100-140 mmHg

      Diastolic LVP: 0-12 mmHg

4.3.3 Valve Pressures:

1. Mitral Valve Pressure Gradient
    - Invasive measurement: Left heart catheterization
    - Normal range: <5 mmHg
2. Tricuspid Valve Pressure Gradient
    - Invasive measurement: Right heart catheterization
    - Normal range: <5 mmHg
3. Aortic Valve Pressure Gradient
    - Invasive measurement: Left heart catheterization
    - Normal range: <10 mmHg

4. Pulmonary Valve Pressure Gradient
    - Invasive measurement: Right heart catheterization
    - Normal range: <20 mmHg

4.3.4 Pulmonary Artery Pressures:

1. Pulmonary Artery Systolic Pressure (PASP)
    - Invasive measurement: Right heart catheterization
    - Normal range: 15-25 mmHg
2. Pulmonary Artery Diastolic Pressure (PADP)
    - Invasive measurement: Right heart catheterization
    - Normal range: 8-20 mmHg
3. Pulmonary Artery Mean Pressure (PAMP)
    - Invasive measurement: Right heart catheterization
    - Normal range: 9-16 mmHg

4.3.5 Aortic Pressures:

1. Aortic Systolic Pressure
    - Invasive measurement: Arterial catheterization
    - Normal range: 100-140 mmHg
2. Aortic Diastolic Pressure
    - Invasive measurement: Arterial catheterization
    - Normal range: 60-90 mmHg
3. Aortic Mean Pressure
    - Invasive measurement: Arterial catheterization
    - Normal range: 70-100 mmHg

4.3.6 Vena Cava (VC) Pressure :

1. Superior Vena Cava (SVC) Pressure
    - Invasive measurement: Right heart catheterization
    - Normal range: 2-8 mmHg
2. Inferior Vena Cava (IVC) Pressure
    - Invasive measurement: Right heart catheterization
    - Normal range: 2-8 mmHg

In general Arterial pressure varies with age [10]

4.4 Invasive Methods :Cardiac Catheterization

4

Cardiac catheterization is a minimally invasive diagnostic and interventional procedure where a slender, flexible tube called a catheter is inserted into a blood vessel,typically in the groin or arm area, and then guided through the vasculature to the heart. This procedure, also known as a cardiac cath, allows health-care providers to access and assess the heart and its surrounding blood vessels . The clinician uses a needle to introduce specialized equipment, including a catheter (a small, customized tube), into a blood vessel (artery or vein). This can be performed on the patient's arm, neck, or leg (Figure 4.1). The clinician then injects contrast material through the catheter and creates X-ray movies (coronary angiogram or coronary angiography)(Figure 4.2) as the contrast material flows through the heart's chambers, valves, and major vessels .There are two main types of cardiac catheterization procedures (Figure 4.3),distinguished by the specific chambers of the heart they access:

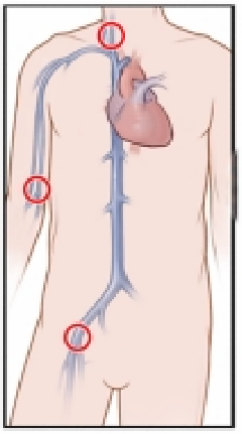

Figure 4.1: Catheter Sites

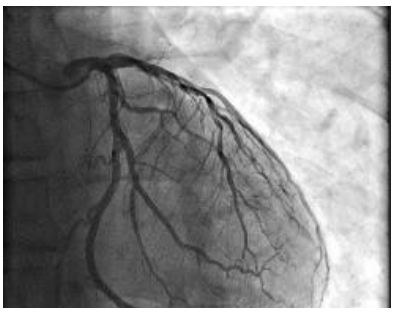

Figure 4.2: Contrast Angiography

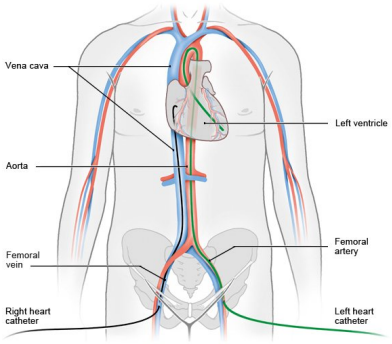

Figure 4.3: Cardiac Catheterization

4.4.1 Right Heart Catheterization

Right heart catheterization is the insertion of a small, flexible tube (catheter) into a vein, usually in the groin or neck, and threaded through the right side of the heart to measure pressures and oxygen levels in the right atrium (Figure 4.4), right ventricle, pulmonary artery, and sometimes the pulmonary capillaries. This procedure is used to diagnose conditions such as pulmonary hypertension, congenital heart defects, and other right-sided heart disorders [27] [51].

1. Components:
    - A long, thin catheter with a special tip that can measure pressure.
    - A guidewire – a thin, flexible wire inserted first to guide the catheter.
    - Sheath – a short, wider tube inserted at the puncture site to allow easier passage of the catheter.
2. Placement:
    - The procedure is typically performed in a cardiac catheterization lab under local anesthesia with sedation.
    - A small puncture is made in the groin area, usually in the femoral artery or vein.

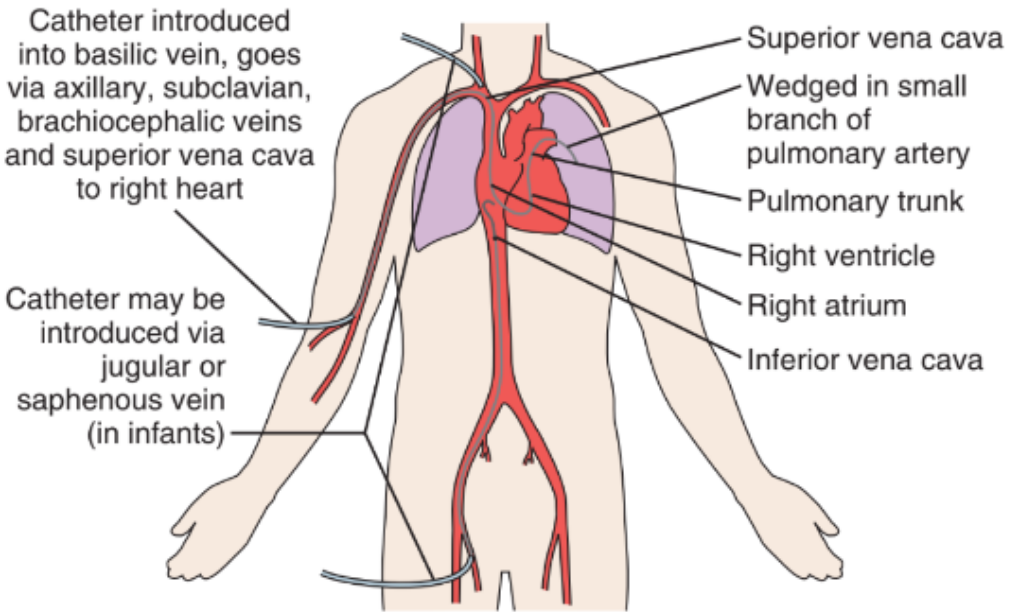

Figure 4.4. Right Heart Catheterization

- The guidewire is inserted first and navigated through the blood vessels under fluoroscopy (real-time X-ray imaging) until it reaches the right atrium of the heart.
- The catheter is then passed over the guidewire and positioned within the right side of the heart.

3. Uses:
   - Measuring pressures within the heart chambers, especially the right atrium and ventricle.
   - Assessing heart valve function on the right side.
   - Evaluating blood flow through the heart, including congenital heart defects.
   - Taking biopsies of heart tissue for further analysis.
   - Administering certain medications or contrast dyes for imaging purposes.

4.4.2 Left Heart Catheterization

Left heart catheterization is the insertion of a small, flexible tube (catheter) into an artery, usually in the groin or wrist (Figure4.5), and threaded through the left side of the heart to measure pressures and oxygen levels in the left ventricle, aorta, and sometimes the coronary arteries. This procedure is primarily used to diagnose and evaluate coronary artery disease, valve disorders, and left-sided heart dysfunction [51].

1. Components:
   - Similar to right heart cath, but the catheter needs to be longer and more maneuverable to reach the left side of the heart.
2. Placement:

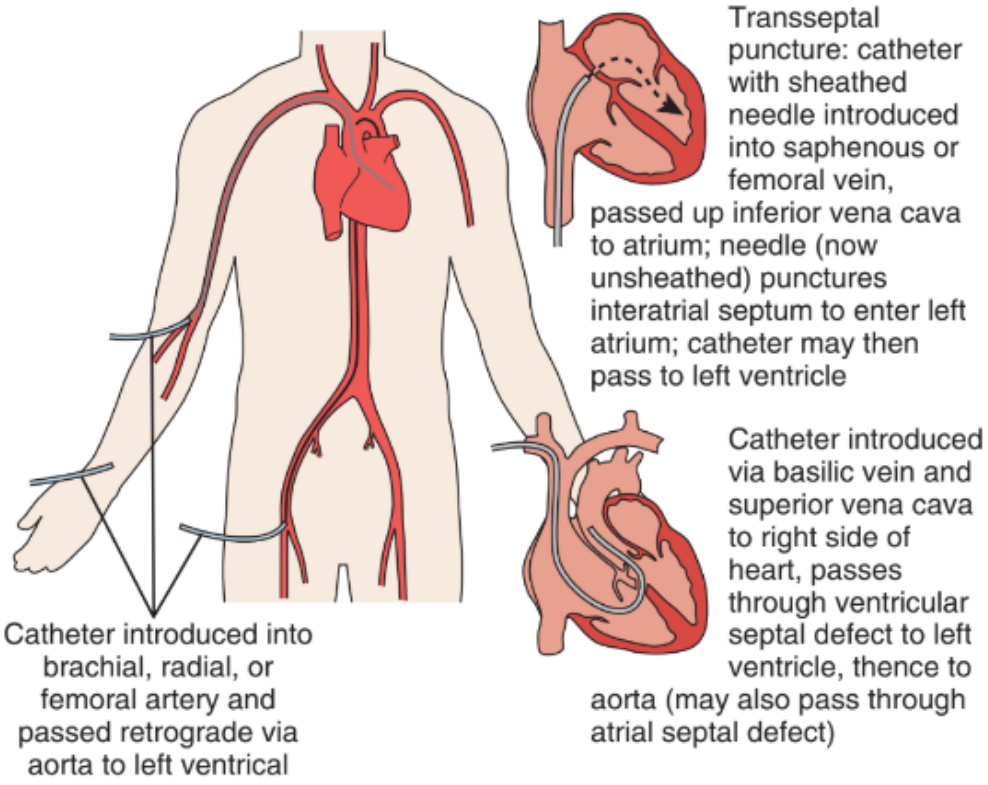

Figure 4.5. Left Heart Catheterization

- The access point and initial steps are similar to right heart cath.
- The guidewire and catheter are navigated through the femoral artery and across the aortic valve to reach the left ventricle.

3. Uses:
   - Measuring pressures within the left atrium and ventricle.
   - Assessing heart valve function on the left side (aortic and mitral valves).
   - Evaluating coronary arteries for blockages through a procedure called coronary angiography.
   - Performing coronary angioplasty and stenting to open blocked arteries.

Important Notes:

- Both procedures require a skilled cardiologist and a team of healthcare professionals.
- There are potential risks associated with the procedure, however, these are minimized by experienced teams and careful monitoring.
- Patients are typically monitored overnight after the procedure for potential complications.

Both procedures provide valuable information about the structure and function of the heart, and are essential tools for cardiologists in the diagnosis and management of various cardiovascular conditions.

4.5 Non-Invasive Methods

Intracardiac pressure estimation using non-invasive methods refers to the techniques that allow for the assessment of pressures within the heart chambers and great vessels without the need for invasive procedures, such as cardiac catheterization. These non-invasive methods rely on various imaging modalities and indirect measurements to provide estimates of intracardiac pressures. The main non-invasive methods for intracardiac pressure estimation include:

4.5.1 Echocardiography

Echocardiography is a non-invasive imaging technique that uses high-frequency sound waves (ultrasound) to create real-time images of the heart's structure and function. One of the key applications of echocardiography is the assessment of intracardiac pressures, which are the pressures within the different chambers of the heart. The main ways that echocardiography can be used to evaluate intracardiac pressures are [85] [79] [73]:

- Doppler Echocardiography: Doppler Echocardiography measures the velocity of blood flow within the heart and blood vessels By analyzing the patterns and velocities of blood flow, it is possible to estimate the pressures in different heart chambers and across heart valves For example, the pressure gradient across a heart valve can be used to estimate the pressure difference between the two chambers on either side of the valve.
- Tricuspid regurgitation velocity: This can be used to estimate the right ventricular systolic pressure (RVSP).
- Pulmonary artery systolic pressure (PASP): This can be estimated by adding the RVSP to the right atrial pressure.
- Mitral inflow velocities: These can be used to estimate left ventricular filling pressures, which are related to left atrial pressure.
- Tissue Doppler imaging: This can provide information about diastolic function and estimate left ventricular filling pressures.

Echocardiography provides direct numerical values of intracardiac pressures on the display screen.

4.5.2 Cardiovascular Magnetic Resonance Imaging (CMR)

Cardiovascular magnetic resonance (CMR) is a sophisticated set of magnetic resonance imaging (MRI) techniques specifically designed to evaluate various aspects of the cardiovascular system. These techniques enable the comprehensive assessment of cardiovascular morphology, ventricular function, myocardial perfusion, tissue characterization, flow quantification, and the detection of coronary artery disease. CMR provides healthcare professionals with a powerful diagnostic tool for the comprehensive evaluation and management of cardiovascular conditions [24] [93].
CMR can be used to estimate intracardiac pressures in several ways [80][91] [75]:

- Phase-contrast CMR: This can be used to measure blood flow velocities in the pulmonary artery, which can be used to estimate pulmonary artery pressures.
- Aortic distensibility: This can be used to estimate central aortic pressure, which is related to left ventricular systolic pressure.

- Ventricular and atrial volumes: Changes in volumes can provide information about intracardiac pressures.

Similar to echocardiography, CMR also provides direct numerical values of intracardiac pressures on the display screen.

4.5.3 Tonometry and pulse wave analysis

Tonometry and pulse wave analysis are two methods that can be used together to estimate the pressure in the aorta, the main artery that carries blood from the heart to the rest of the body Unlike echocardiography, these methods do not provide direct numerical values of intracardiac pressures, but rather indirectly estimate them based on mathematical parameters and relationships. Tonometry involves applying a small probe to the skin over a pulse point, such as the wrist, to measure the pressure waves in the arteries. Pulse wave analysis looks at how the pressure wave travels through the blood vessels and can provide information about the stiffness of the arteries. By combining these two techniques, it is possible to get a more accurate estimate of the pressure in the aorta, which is an important indicator of cardiovascular health [69].

- How Tonometry Captures the Pulse Wave:

Tonometry captures the pulse wave through a specific process. First, the sensor of the tonometer is placed over a superficial artery, typically the radial artery at the wrist. The sensor then detects the subtle changes in arterial diameter caused by the passing pulse wave. These diameter changes are then converted into a graphical representation of the pulse wave, showing its shape, amplitude, and timing.

- Pulse Wave Analysis for Aortic Pressure Estimation:

Pulse wave analysis is used to estimate the aortic pressure based on the information captured by tonometry. The pulse wave measured at the wrist (peripheral) is different from the one in the aorta (central) due to the properties of the arterial tree. Sophisticated algorithms and mathematical models are used to analyze the peripheral pulse wave and estimate the central aortic pressure waveform. These models consider key parameters, such as the pulse wave velocity (PWV), which indicates the stiffness of the arteries, and the augmentation index, which represents the degree to which the reflected wave from the periphery adds to the pressure in the aorta. By analyzing these parameters, the models can estimate the central aortic systolic pressure, diastolic pressure, and pulse pressure (the difference between the two), providing a more accurate assessment of the cardiovascular health.

4.5.4 Biomarkers

Biomarkers can be used to provide indirect information about intracardiac pressures in the following ways:

1. Natriuretic Peptides:

    - Biomarkers like BNP (brain-derived natriuretic peptide) and NT-proBNP (N-terminal pro-B-type natriuretic peptide) are released by the heart in response to increased wall stress and elevated intracardiac pressures [50].

    - Higher levels of these natriuretic peptides indicate the presence of increased intracardiac pressures, such as those seen in conditions like heart failure, valvular heart disease, or pulmonary hypertension [50].

- By measuring the concentrations of these biomarkers, clinicians can gain insights into the patient's intracardiac pressure status and use this information to guide diagnosis and treatment decisions.

2. Indirect Pressure Estimation:

   - While biomarkers do not directly measure intracardiac pressures, they can provide indirect estimates of pressure levels.
   - Elevated natriuretic peptide levels are associated with increased filling pressures, ventricular wall stress, and overall intracardiac pressures.
   - By combining biomarker information with other clinical data, such as echocardiographic findings and patient symptoms, clinicians can make more informed assessments of a patient's intracardiac pressure status.

3. Monitoring and Management:

   - Biomarker levels can be used to monitor changes in intracardiac pressures over time, particularly in the context of disease progression or response to treatment.
   - Tracking the trends in natriuretic peptide concentrations can help clinicians evaluate the effectiveness of interventions aimed at reducing intracardiac pressures, such as medications, device therapies, or lifestyle modifications.

4.6 Mathematical Equations for Estimating Intracardiac Pressure

4.6.1 Pulmonary Artery Pressure

Pulmonary artery pressure (PAP) is a critical parameter in assessing cardiovascular health, particularly in diagnosing and managing pulmonary hypertension and other heart-related conditions. Various methods, both invasive and non-invasive, have been developed to estimate PAP accurately. This synthesis reviews the mathematical equations and models used to estimate pulmonary artery pressure based on the provided research papers.

Spectral Analysis of Heart Sounds :

A non-invasive technique utilizing spectral analysis of the second heart sound (S2) has been shown to estimate pulmonary artery systolic pressure (PASP) with a strong correlation to measurements obtained via Doppler ultrasound [21]. The derived equation for estimating PASP is as follows:

$$\text{PASP} = 47 + 0.68F_p - 4.4Q_p - 17\frac{F_p}{F_a} - 0.15F_s \tag{4.1}$$

In this equation, F_s and F_p represent the dominant frequencies, Q_p indicates the quality of resonance of P2, defined as

$$Q_p = \frac{F_p}{f_2 - f_1}$$

where $(f_2 - f_1)$ is the frequency range surrounding F_p, and $\frac{F_p}{F_a}$ denotes the ratio of the dominant frequencies.

However, it is noteworthy that there are two articles by the same authors, Chen et al. (1996), both titled "Estimation of pulmonary artery pressure by spectral analysis of the second heart sound." One version, available through Google Scholar, uses $F_p \cdot F_a$ (multiplication) [21]; while the version accessible at the provided PubMed link employs $\frac{F_p}{F_a}$ (division) `https://pubmed.ncbi.nlm.nih.gov/8857483/`. This inconsistency raises questions about the accuracy of the equations presented. Furthermore, Tranulis et al. (2002) also referenced the equation with $\frac{F_p}{F_a}$, suggesting continuity in the use of this formulation from Chen et al.

Doppler Echocardiography:

Doppler transmitral flow velocity patterns can estimate pulmonary arterial wedge pressure (PAWP) [95] using the equation:

$$\text{PAWP} = 18.4 + 17.1 \cdot \ln\left(\frac{E}{A}\right) \tag{4.2}$$

where the E/A ratio is a key Doppler index.
The modified Dabestani-Mahan formula estimates pulmonary artery systolic pressure (PASP) using right ventricular outflow tract acceleration time (AT) [90] with the equation:

$$\text{PASP} = 145 - AT \tag{4.3}$$

This method shows a strong correlation with the TR peak velocity method [67].
Three Doppler methods (tricuspid regurgitation, pulmonary flow analysis, and right ventricular isovolumic relaxation time) can predict pulmonary artery pressure, with tricuspid regurgitation providing the most reliable predictions [16].

4.6.2 Aortic Artery Pressure

To estimate aortic artery pressure inside the heart, several mathematical models and methods have been proposed.

Generalized Transfer Function (GTF) Method:

This method involves using a generalized transfer function to transform peripheral pressure measurements (e.g., radial tonometry) into central aortic pressure estimates. The GTF is derived from the average of individual transfer functions calculated for each patient [20] [40].

Multichannel Wiener System:

This approach models the arterial system as a multichannel Wiener system, which includes a linear finite impulse response filter and a nonlinear memoryless function block. By measuring pressure waveforms from two distinct peripheral locations, a multichannel blind system identification technique can estimate the common input pressure signal[68].

Empirical Formula for Mean Aortic Pressure (MAP):

An empirical formula for estimating MAP at the aortic root level is given by:

$$\text{MAP} = \text{DAP} + \frac{\text{PP}}{3} \tag{4.4}$$

where DAP is diastolic aortic pressure and PP is pulse pressure. This formula accounts for the mechanical principles in the arterial system and provides a precise estimate of MAP [19]

Geometric Mean Method:

The geometric mean of systolic (SAP) and diastolic aortic pressures (DAP) can be used to estimate MAP:

$$\text{MAP} = \sqrt{\text{SAP} \times \text{DAP}} \tag{4.5}$$

This method establishes a simple mathematical link between the steady and pulsatile components of aortic pressure [17].

Autoregressive with Exogenous Input (ARX) Model:

This algorithm estimates instantaneous aortic blood flow by analyzing arterial blood pressure waveforms. The ARX model is applied to diastolic ABP waveforms to estimate autoregressive model coefficients, which are then used to estimate ABF from the entire ABP signal [5]

Personalized-Model-Based Central Aortic Pressure (PM-CAP) Method:

This method uses a human aortic network model based on viscous fluid mechanics theory. By measuring the pulse wave at the proximal and distal ends of the radial artery, patient-specific circuit parameters are estimated using the least square method. The central aortic pulse wave is then obtained by calculating the transfer function between the radial artery and central aorta [48] [49]

Multiple Regression Models for Pressure Pulse Amplification (PPA):

Pressure pulse amplification between the aorta and brachial artery can be estimated using multiple regression models based on subject parameters such as gender, age, height, weight, heart rate, and brachial pressures [15]

These methods provide various mathematical approaches to estimate aortic artery pressure, each with its own advantages and limitations. The choice of method may depend on the specific clinical or research context and the available data.

4.6.3 Right Ventricular Pressure

To estimate the right ventricular systolic pressure (RVSP) inside the heart, several mathematical models and equations have been proposed and validated through various studies. Here are some key methods and their corresponding equations [88] [99] [87]:

Simplified Bernoulli Equation (SBE):

$$\text{RVSP} = 4v^2 + \text{mRA} \tag{4.6}$$

where (v) is the maximal tricuspid regurgitant (TR) velocity and (mRA) is the mean right atrial pressure

Modified Bernoulli Equation:

In cases of severe tricuspid regurgitation, the inertial pressure component becomes significant. The complete Bernoulli equation, which includes the inertial pressure, can be used:

$$\text{RVSP} = 4v^2 + \text{mRA} + \text{Inertial Pressure} \tag{4.7}$$

where the inertial pressure is related to the regurgitant orifice diameter (ROD) [88]

Echo-Doppler Formula with Inferior Vena Cava Collapsibility Index (IVCCI):

A new formula for RVSP estimation incorporates the IVCCI to estimate RA pressure [72]:

$$\text{RVSP} = \Delta P + \text{RA Pressure} \tag{4.8}$$

where ΔP is the RV-RA gradient calculated by $4v^2$, and RA pressure is assigned based on IVCCI values:

- 6 mmHg for IVCCI $> 45\%$
- 9 mmHg for IVCCI between 35% and 45%
- 16 mmHg for IVCCI $< 35\%$

Pressure-Volume Loop Analysis:

This method involves generating a pressure-volume loop using 3-D echocardiography and Doppler measurements to estimate RV stroke work (RVSW) and RVSP:

$$\text{RVSW} = \text{Area enclosed by the pressure-volume loop} \tag{4.9}$$

This method provides a semi-invasive approach to estimate RVSP and RV function [47]

Cardiac MRI-Based Models:

Cardiac MRI can be used to estimate RVSP through complex models involving multiple MRI variables:

$$\text{RVSP} = -179 + \log_e(\text{ISA}) \times 42.7 + \log_{10}(\text{VMI}) \times 7.57 + \text{BSFS} \times 3.39 \tag{4.10}$$

ISA: Intraventricular Septal Angle, **VMI:** Ventricular Mass Index, **BSFS:** Black Blood Slow Flow Score. This model correlates strongly with catheterization measurements and can be adapted for RVSP estimation [23].

RV-E/e' Ratio:

The RV-E/e' ratio, derived from Doppler and tissue Doppler echocardiography, can be used to estimate right atrial pressure (RAP) and subsequently RVSP:

$$\text{RVSP} = 4v^2 + \text{RAP} \tag{4.11}$$

where RAP is estimated using the RV-E/e' ratio [32]
These methods provide various approaches to estimate RVSP non-invasively, each with its own advantages and limitations depending on the clinical context and the severity of tricuspid regurgitation.

4.6.4 Right Atrial pressure

To calculate right atrial pressure (RAP) inside the heart, several methods and mathematical equations have been proposed and evaluated in the literature:

RV-E/e' Ratio:

This method uses the ratio of early tricuspid inflow velocity (E) to early diastolic tissue Doppler velocity of the tricuspid annulus (e') to estimate RAP.

$$\text{RAP} \approx \text{RV-E/e'} \tag{4.12}$$

This method has shown reasonable diagnostic ability in certain populations but is less reliable in others [32].

Inferior Vena Cava (IVC) Diameter and Collapsibility:

This method estimates RAP based on the diameter of the IVC and its percentage change during inspiration.
If IVC diameter < 2.1 cm and collapsibility $> 50\%$, RAP = 0-5 mmHg. If IVC diameter > 2.1 cm and collapsibility $< 50\%$, RAP = 10-20 mmHg.

$$\text{RAP} = \text{IVC diameter} \times \text{Collapsibility Index} \tag{4.13}$$

This method is commonly used but has limitations in precision and accuracy [94] [12] [53]

Multiparametric Approach:

This method combines multiple echocardiographic parameters, including IVC diameter, tricuspid E/e' ratio, and hepatic vein flow.

$$\text{RAP} = \frac{\text{eRAPIVC} + \text{eRAPE/e'} + \text{eRAP}_{\text{HV}}}{3} \tag{4.14}$$

This approach aims to improve accuracy but does not necessarily provide a significant advantage over simpler methods [92].

Right Ventricular Regional Isovolumic Relaxation Time:

This method uses the interval between the end of systolic annular motion and the onset of early diastolic filling wave.

$$\text{RAP} \approx \text{RV Isovolumic Relaxation Time} \tag{4.15}$$

This method has shown an inverse relationship with mean RAP [1]
while several non-invasive methods exist for estimating RAP, each has its own limitations and varying degrees of accuracy. The choice of method may depend on the clinical context and the available echocardiographic views. For the most precise measurement, invasive monitoring remains the gold standard.

4.6.5 Left Ventricular Pressure

To determine the pressure within the left ventricle, various mathematical methods have been proposed in the literature:

MRI-based Pressure Calculation Using Acceleration Data:

Navier-Stokes Equation: The pressure gradients within the left ventricle can be calculated from MR maps of blood acceleration by applying the Navier-Stokes (NS) equation. This method involves:

$$\nabla P = \rho(\mathbf{a} + \mathbf{g}) \tag{4.16}$$

where ∇P is the pressure gradient, ρ is the blood density, $\mathbf{a}$ is the acceleration, and $\mathbf{g}$ is the gravitational acceleration.

Optimization Algorithm: An original algorithm is employed to compute the pressure distribution by minimizing the pressure gradient curl, ensuring that the result in a given pixel is independent of the integration path [14].

Model-Based Estimation for Aortic Stenosis:

Cardiovascular System Model: This model includes descriptions of cardiac electrical activity, elastance-based cardiac cavities, systemic and pulmonary circulations, and heart valves. The left ventricular pressure P_{LV} can be estimated using:

$$P_{\mathrm{LV}} = E(t) \cdot (V_{\mathrm{LV}} - V_0) \tag{4.17}$$

where $E(t)$ is the time-varying elastance, V_{LV} is the left ventricular volume, and V_0 is the volume at zero pressure.

Parameter Identification: A Monte Carlo cross-validation approach is used for parameter identification, allowing for the estimation of LV pressures from both invasive and non-invasive data [66].

Interrelationships in Mammals of Different Sizes:

Volume-Pressure Relationships: Mathematical equations describe the interrelationships between left ventricular end-diastolic volume (EDV), end-systolic volume (ESV), stroke volume (SV), cardiac output (CO), stroke-work (SW), heart rate (HR), and total peripheral resistance (TPR).

$$P_{LV} = f(EDV, ESV, SV, CO, SW, HR, TPR) \tag{4.18}$$

These equations help in understanding the functional patterns of the left ventricle across different mammalian sizes [46].

By integrating these methods, one can derive a comprehensive mathematical model for calculating left ventricle pressure, tailored to specific clinical or research needs.

To calculate the left atrial pressure (LAP) inside the heart, we can refer to the method described in the first paper. Here is the mathematical equation and the process for estimating LAP:

4.6.6 Left Atrial Pressure

The left atrial pressure can be estimated using the following equation:

$$\mathrm{LAP} = \mathrm{SBP} - \mathrm{MRPG} \tag{4.19}$$

Where:

LAP is the left atrial pressure. SBP is the systolic blood pressure measured from the brachial artery. MRPG is the mitral regurgitant pressure gradient.

Process for Estimation Measure Systolic Blood Pressure (SBP): Use brachial sphygmomanometry to measure the peak systolic blood pressure.
Determine Mitral Regurgitant Pressure Gradient (MRPG): Use continuous-wave Doppler echocardiography to measure the peak mitral regurgitant velocity during systole.
Apply the modified Bernoulli equation to calculate the pressure gradient:

$$\text{MRPG} = 4 \times (\text{velocity})^2 \tag{4.20}$$

Calculate Left Atrial Pressure (LAP): Subtract the mitral regurgitant pressure gradient from the systolic blood pressure:

$$\text{LAP} = \text{SBP} - \text{MRPG} \tag{4.21}$$

This method has been validated in patients with congestive heart failure and mitral regurgitation, showing a strong correlation with mean pulmonary capillary wedge pressure (r = 0.88)[37].
Additional Insights The second paper discusses a multi-scale model of the cardiovascular system, which includes the left atrium and left ventricle. This model simulates the left atrium's behavior throughout the cardiac cycle and can reproduce realistic pressure-volume loops. While this model provides a comprehensive understanding of atrial function, it is more complex and not directly used for simple LAP calculations [74].
By following the steps outlined above, you can noninvasively estimate the left atrial pressure using Doppler echocardiography and sphygmomanometry, as validated in clinical studies [37].

4.6.7 Mitral Valve Pressure

Several mathematical models and equations can be employed to calculate the pressure inside the mitral valve:

Force and Torque Balance Equations:

The mechanical model of the mitral valve can be represented using force and torque balance equations. These equations are derived using the principle of virtual work and the Weierstrass-Erdmann condition of variational nature. The chordae tendineae are modeled as a force applied to the free endpoint of the flaps [3].

Gorlin Formula:

The Gorlin formula is used to calculate the effective area of the mitral valve and is given by:

$$A = \frac{CO}{\sqrt{dP}} \tag{4.22}$$

where (A) is the valve area, (CO) is the cardiac output, and (dP) is the pressure gradient across the valve. This formula is pressure- and flow-dependent and primarily relates to the effective area occupied by flow [28].

New Orifice Equation:

A new orifice equation that relates the effective mitral valve area ((A)), the average mitral valve pressure gradient ((dP)), the cardiac output ((Q)), and the heart frequency ((f)) is given by:

$$A = \frac{4.75 \times 10^{-5} Qf}{dP} \tag{4.23}$$

where (A), (Q), and (dP) are expressed in cm², ml/min, and mmHg, respectively [82].

Bernoulli Equation with Inertial Term:

The pressure-velocity relationship across the mitral valve can be approximated by the Bernoulli equation with an inertial term:

$$\Delta P = \frac{1}{2}\rho \Delta v^2 + M\frac{dv}{dt} \tag{4.24}$$

Where ΔP is the atrioventricular pressure difference, ρ is blood density, v is transmitral flow velocity, and M is mitral inertance. This equation accounts for both convective and inertial forces [62] [31].

Hydraulic Orifice Equation:

For prosthetic mitral valves, an alternative hydraulic orifice equation can be used:

$$A = \frac{21SV}{DFP^2} \tag{4.25}$$

where (A) is the effective prosthesis orifice area in cm², (SV) is the stroke volume in ml, and (DFP) is the diastolic filling period in s/min [84].

Standard Hydrokinetic Orifice Formula:

Another formula for calculating the area of the stenotic mitral valve is:

$$A = FC\sqrt{2gh} \tag{4.26}$$

where (A) is the cross-sectional area in cm², (F) is the flow rate in cc/s, (C) is an empirical constant, (g) is gravity acceleration, and (h) is the pressure gradient across the orifice in mmHg [38].
These equations provide a comprehensive approach to calculating the pressure inside the mitral valve, considering various factors such as flow rate, pressure gradient, and valve area.

4.6.8 Aortic Valve Pressure

To calculate the pressure inside the aortic valve, several mathematical equations and models can be utilized :

One-Dimensional Unsteady Inviscid-Flow Equations:

These equations are used to model the pressure distribution in normal and stenosed aortic valves. The pressure difference between the inlets of the coronary arteries and the ventricle can be calculated using these equations [9].

Orifice Equation for Aortic Valve Area:

An orifice equation relates the effective aortic valve area (A), the average aortic valve pressure gradient (dP), the stroke volume (SV), and the heart frequency (FH).The equation is:

$$A = \left(7.5 \times 10^{-5}\right)\frac{SV \cdot FH^2}{dP} \tag{4.27}$$

where A is in cm², SV in ml, FH in s ^{1}, and dP in mmHg [83].

Time-Dependent Instantaneous Pressure Gradient Model:

This model predicts the time-dependent instantaneous pressure gradient across a stenotic aortic valve. It incorporates the Reynolds number dependence of both steady and unsteady terms. The model is validated through pulse duplicator experiments [45].

Gorlin Formula and Continuity Equation:

Both the Gorlin formula and the continuity equation are used to calculate valvular areas. The Gorlin formula is:

$$A = \frac{CO}{HR \cdot \sqrt{dP}} \tag{4.28}$$

where CO is the cardiac output, HR is the heart rate, and dP is the pressure gradient. The continuity equation is based on the principle of conservation of mass [28].

Electric Analog Model:

This model uses resistance (R), inertance (L), and compliance (C) parameters to calculate continuous beat-to-beat aortic flow using left ventricular pressure (LVP) and aortic pressure (AoP). The second-order differential equations derived from this model can be used to calculate the pressure gradient [39].

Difference Equation Model for Re-Reflections:

This model simulates re-reflections of arterial pressure waves at the aortic valve. It splits the aortic blood pressure into forward and backward components and calculates them separately. The reflection coefficient at the aortic valve is a key parameter in this model [44].

Mathematical Model of Aortic Valve Dynamics:

This model describes the dynamics of the aortic valve during systole, incorporating sinus vortex local pressure and variations in systemic vascular resistance. It uses Hill's semi-spherical vortex model and an aortic pressure-area compliance relationship to predict pressure variations [2].
By utilizing these equations and models, it is possible to accurately calculate the pressure inside the aortic valve under various physiological and pathological conditions.

4.6.9 Pulmonary Valve Pressure

o determine the pressure inside the pulmonary valve, various mathematical equations and methods can be applied based on the available research papers:

Nonlinear Cross-Sectional-Area-Averaged System of Equations:

This method involves using a nonlinear system of equations for a Newtonian fluid in an elastic tube to predict blood flow and pressure in larger arteries and veins. The inflow into the main pulmonary artery is obtained from MRI measurements, and the pressure entering the left atrium from the main pulmonary vein is kept constant at the normal mean value of 2 mmHg [77].

Sigmoidal Equation for Pressure-Volume Curves:

$$V = a + b[1 - e^{-(P-c)/d}]^{-1} \tag{4.29}$$

The sigmoidal equation can be used to characterize lung and respiratory system pressure-volume (P-V) curves. In this equation, (a) corresponds to the volume of a lower asymptote, (b) to the volume difference between upper and lower asymptotes, (c) to the pressure at the true inflection point of the curve, and (d) to a width parameter proportional to the pressure range within which most of the volume change occurs [96].

Simplified Bernoulli Equation:

The simplified Bernoulli equation is often used to estimate pressure gradients across the pulmonary valve

$$\Delta P = 4v^2 \tag{4.30}$$

where ΔP is the pressure gradient and v is the velocity of blood flow through the valve. However, this method has limitations and may not always provide accurate estimates due to factors like viscous and inertial forces [36].

New Formula for Predicting MPAP from SPAP:

$$\text{MPAP} = 0.61 \times \text{SPAP} + 2 \tag{4.31}$$

A new formula has been proposed to predict mean pulmonary artery pressure from systolic pulmonary artery pressure. This formula has been validated and can help refine the threshold pressure values used in the diagnosis of pulmonary hypertension [18].

Modified Dabestani-Mahan Formula:

$$\text{PASP} = 145 - \text{AT} \tag{4.32}$$

The modified formula can estimate normal pulmonary artery systolic pressure (PASP) using right ventricular outflow tract acceleration time (AT). This method is useful in the absence of sufficient Doppler data for the tricuspid regurgitation peak velocity method [90].
By employing these equations and methods, it is possible to estimate the pressure inside the pulmonary valve with varying degrees of accuracy and applicability based on the specific clinical scenario and available data.

4.6.10 Tricuspid Vlave Pressure

To calculate the pressure inside the tricuspid valve, particularly in the context of tricuspid regurgitation, several mathematical equations and methods are used:

Simplified Bernoulli Equation (SBE):

The SBE is commonly used to estimate the right ventricular systolic pressure (RVSP) by adding the mean right atrial pressure (mRA) to the convective pressure, which is calculated as (4v2), where (v) is the maximal tricuspid regurgitant (TR) velocity.

$$\text{RVSP} = 4v2 + \text{mRA} \tag{4.33}$$

This method is widely validated and correlates well with invasive measurements [88] [87] [25] [99].

Complete Bernoulli Equation:

For more severe cases of tricuspid regurgitation, the complete Bernoulli equation, which includes inertial pressure, is used to model pressure and flow in all chambers and vascular beds. This approach accounts for the inertance of TR flow, which can cause the TR peak velocity to lag behind the maximal RVSP time point, leading to underestimation of RVSP when using the simplified Bernoulli equation alone [88].

Modified Bernoulli Equation for Diastolic Pressure Gradient:

In cases of tricuspid stenosis, the mean tricuspid diastolic pressure gradient is calculated using the modified Bernoulli equation:

$$\Delta P = 4v^2 \tag{4.34}$$

This method is used to calculate the pressure gradient across the tricuspid valve during diastole [29].
These equations and methods provide a comprehensive approach to estimating the pressure inside the tricuspid valve, particularly in the presence of tricuspid regurgitation and stenosis.

4.7 Applications Cardiac Pressure Estimation

4.7.1 Calculation of pulmonary artery diameter for pulmonary hypertension prediction (Image Processing)

The primary aim of this study is to assess whether the diameters of the pulmonary artery, measured from computed tomographic (CT) images using a MATLAB program, can serve as reliable indicators of pulmonary artery hypertension (PAH). This application focuses on estimating pulmonary artery pressure based on the calculation of pulmonary artery diameter, which is a critical marker, as stenosis or dilation in this artery is linked to the development of pulmonary hypertension (Figure 4.8).
Although this research does not establish a comprehensive method for the early detection of pulmonary hypertension, it represents a significant preliminary step toward developing a proof of concept.
A thoracic CT dataset comprised of 807 transverse contrast-enhanced images of the pulmonary artery bifurcation was analyzed. Patients were divided into a control group without diagnosed pulmonary hypertension and three groups with progressively severe pulmonary hypertension, as assessed by mean pulmonary artery pressure (mPAP) measured through invasive right heart catheterization. The classifications are as follows: Group 1 (20 mmHg mPAP $<$ 25 mmHg), Group 2 (25 mmHg mPAP 30 mmHg), and Group 3 (mPAP $>$ 30 mmHg). For further details about the dataset, please refer to the Kaggle platform "`https://www.kaggle.com/datasets/turkertuncer/ph-ct-v1`"

Pretreatment:

In the initial phase , unimportant edges are removed from the image utilizing the morphological application known as Clearing Borders. This morphological reconstruction technique involves eliminating objects that are in contact with the image edges, as these objects contribute incomplete information. In this context, the image is designated as the mask, with the marker defined as follows :

$$f_m = \begin{cases} f(x,y) & \text{si } (x,y) \\ 0 & \text{ailleurs} \end{cases} \tag{4.35}$$

The reconstruction $E(f(m))$ contains only the objects touching the edge and the difference $f - E(f(m))$ contains only the objects not touching the edge.

The Matlab command is: `imclearborder`.

Segmentation:

In this step, the extraction of the object of interest, specifically the pulmonary artery, is achieved using the "Crop Image" Tool. Subsequently, the resulting image undergoes binarization through manual thresholding based on the image histogram. Non-relevant objects are eliminated using morphological erosion (Figure4.6). The morphological erosion of an object X by the structuring element B is defined by the principle of duality :

$$\overline{\varepsilon}_B(X) = \overline{\delta}_B(X) \tag{4.36}$$

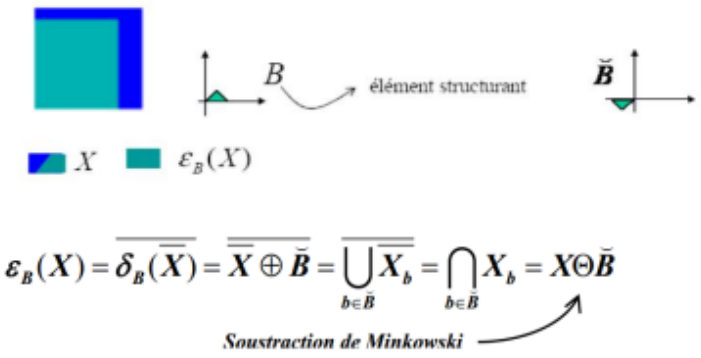

Figure 4.6. the principle of duality

$$\mathcal{E}_B(X) = \{\langle z \rangle \mid B_z \subseteq X\} \tag{4.37}$$

This describes the locus of points z (the center of the structuring element B) such that the translated structuring element B_z is contained within X. For example, consider the erosion of X by a disc-shaped structuring element B (Figure4.7):

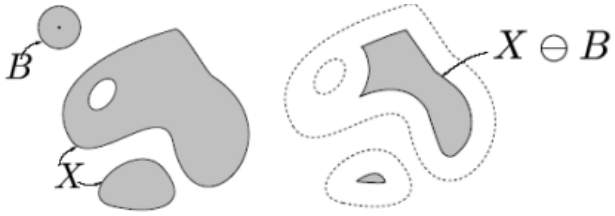

Figure 4.7. Erosion of X by a disc B:

Characterization :

Finally, the function area_ open is employed to delineate the minor axis, which corresponds to the diameter of the pulmonary artery. This function enables the results to be expressed in pixel dimensions .

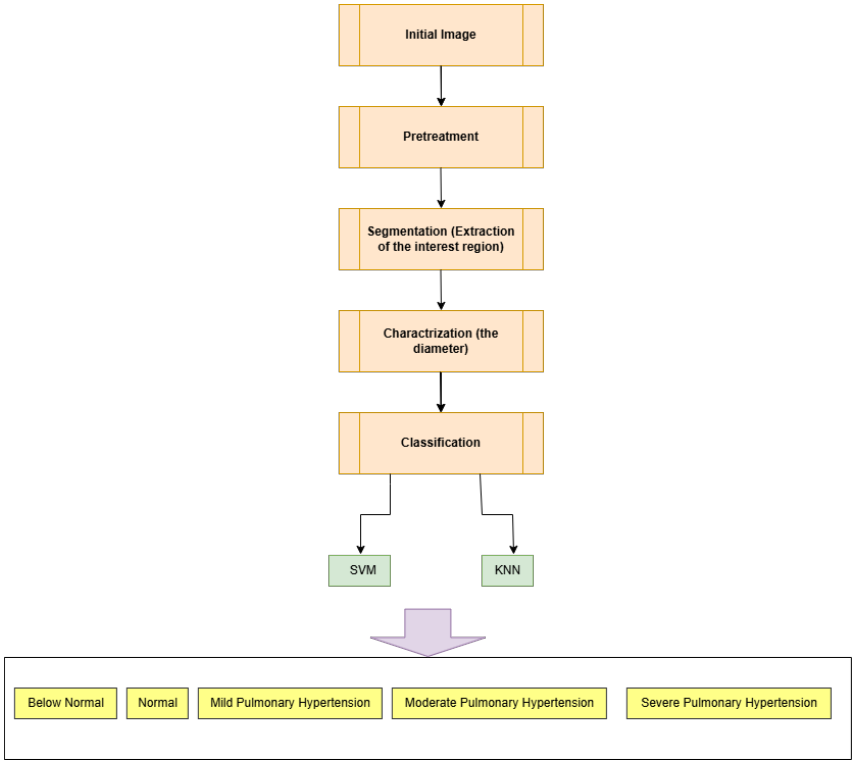

Figure 4.8. Detection of PAH using PAD

PAH: Pulmonary Artery Hypertension, DPA: Pulmonary Artery Diameter

Results

To calculate the diameter of the pulmonary artery, several steps were undertaken: preprocessing (Figure4.9), segmentation (Figure4.10), and characterization (Figure 4.11). The objective was to elucidate the relationship between cardiac pressure and the parameters measured from cardiac imaging, specifically the diameter of the pulmonary artery. The results obtained indicate a correlation between the narrowing of the pulmonary artery and the presence of pulmonary arterial hypertension (PAH).
Furthermore, the findings explore the relationship between cardiac pressure and pulmonary artery diameter, represented as $P = f(d)$. This correlation assists in identifying pathological conditions, particularly pulmonary arterial hypertension. Given the conversion factor of **1 cm = 37.79527559055 pixels**, this measurement translates into diameter values that are detailed in Table 4.1.

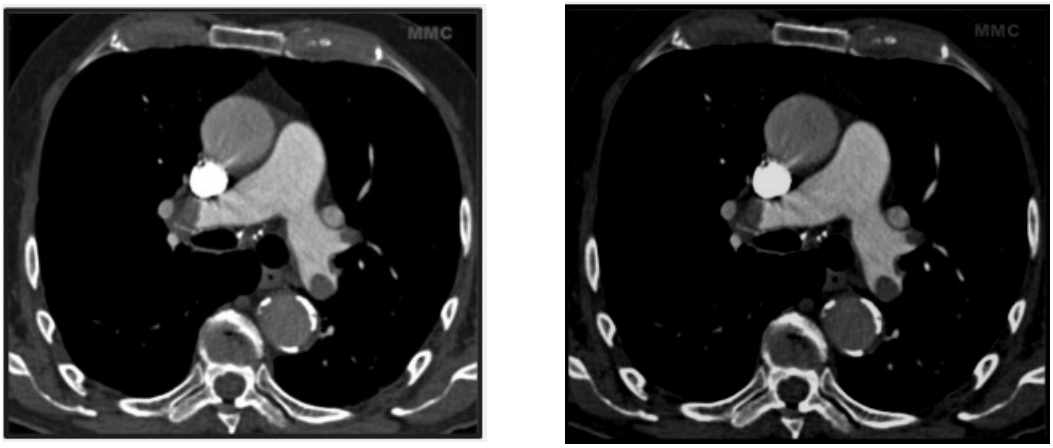

(1) (2)

Figure 4.9: Pretreatment Phase

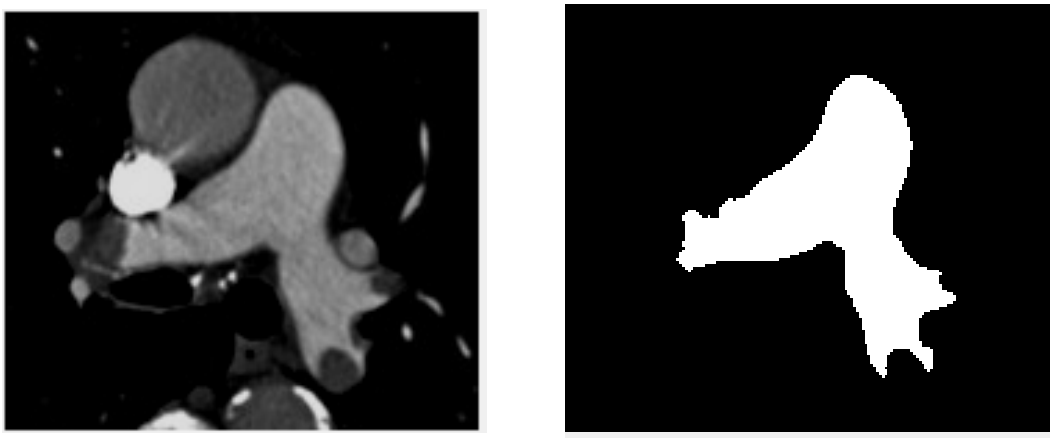

(3) (4)

Figure 4.10: Binarization and segmentation

(5) (6)

Figure 4.11: Calculation of the maximum diameter of the left pulmonary artery prior to branching

Table 4.1: Selected Pictures of Pulmonary Hypertension

Condition	Picture Filename	Diameter (cm)	Diameter (pixels)	SVM / KNN Prediction
Normal Condition	4_323.png	2.05	77.39	Normal
	4_371.png	2.08	78.66	Normal
Mild Pulmonary Hypertension	1_6.png	2.64	99.75	Mild Pulmonary Hypertension
	1_77.png	2.61	98.79	Mild Pulmonary Hypertension
Moderate Pulmonary Hypertension	2_14.png	3.77	142.38	Moderate Pulmonary Hypertension
	2_49.png	3.24	122.37	Moderate Pulmonary Hypertension
Severe Pulmonary Hypertension	3_269.png	6.53	246.85	Severe Pulmonary Hypertension
	3_294.png	7.20	272.18	Severe Pulmonary Hypertension

The classification outcomes derived from the K-Nearest Neighbors (KNN) and Support Vector Machine (SVM) models demonstrate a robust capability in differentiating between the severity levels of pulmonary hypertension, as assessed through diameter measurements. The KNN model achieved a flawless accuracy of 100%, indicating that it accurately classified all instances within the dataset. This result underscores the KNN algorithm's effectiveness in discerning the distinctions among the defined categories based on diameter. Conversely, the SVM model yielded an impressive accuracy of approximately 99.38%, signifying its remarkable performance.

The accompanying box plot (Figure 4.12) elucidates the distribution of diameter measurements across the various categories. It reveals that patients diagnosed with severe pulmonary hypertension exhibit the largest diameter measurements, in contrast to those classified as normal, who display the smallest measurements. The pronounced separation between these categories suggests that diameter serves as a significant predictor for the classification of pulmonary hypertension severity. The classification criteria

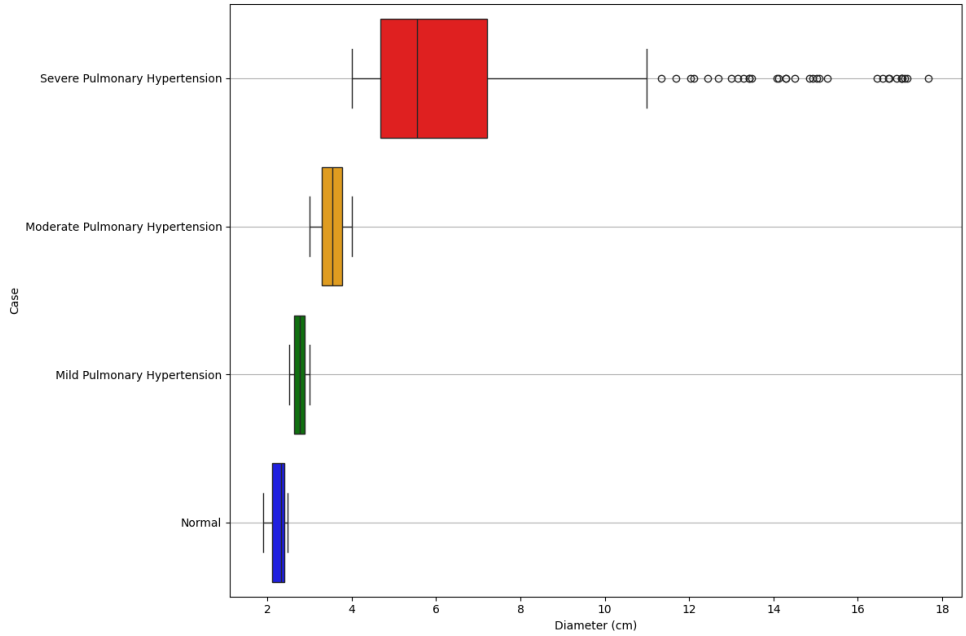

Figure 4.12. Distribution of Diameter by Case of Pulmonary Hypertension

utilized in this analysis are based on specific diameter measurements (in centimeters) and corresponding pressures (in mmHg):

- **Below Normal**: Diameter < 1.5 cm
- **Normal**: 1.5 cm Diameter < 2.5 cm
- **Mild Pulmonary Hypertension**: 2.5 cm Diameter < 3.0 cm
- **Moderate Pulmonary Hypertension**: 3.0 cm Diameter < 4.0 cm
- **Severe Pulmonary Hypertension**: Diameter 4.0 cm

In summary, both models validate the established classification criteria, demonstrating that diameter is a reliable feature for distinguishing among different cases of pulmonary hypertension.

Study Limitations

- The study is constrained by the limited availability of data, highlighting an urgent need for comprehensive clinical data.

- The credibility of the study may be questioned due to the absence of established methods for verifying the validity of the results, particularly concerning pulmonary arterial pressure measurements obtained via echocardiography and their comparison with other findings.
- There is a lack of thorough monitoring in the investigation of the correlation between pulmonary artery diameter and pressure.

4.7.2 Right Heart Pressure Estimation (Heart Simulation)

The objective of this application is to investigate pressure and velocity within the right heart. Utilizing the COMSOL program (COMSOL - Logiciel de Simulation Multiphysique) , an approximate two-dimensional model of the heart was developed based on cardiac imaging data (Figure 4.13). While this study does not fully validate the treatment of right heart contraction and dilation with a flow modulator, it represents a significant initial step toward establishing a proof of concept.

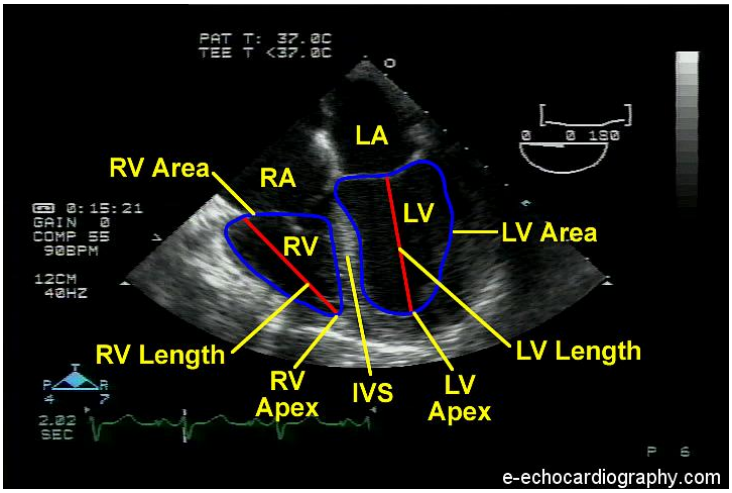

Figure 4.13. Real geometry of heart extracted by medical imaging techniques

Geometry

The modeling domain is highly complex, necessitating extensive computational resources. Consequently, it was not possible to perform the calculation the entire heart model due to the intricacies of its geometry and the length of time it takes (Figure 4.14); thus, a two-dimensional representation of the right heart was selected.
The model was developed using COMSOL software that approximates the shape of the right heart in two dimensions, albeit with a modified morphology. This model comprises an ellipse and squares, with two line segments representing inlet corresponding to the superior vena cava and outlet representing the pulmonary valve as illustrated in (Figure 4.15) .

Materials

For the modeling process, the material selected from the COMSOL Multiphysics library is “styrene rubber ‘CSbr’,” which serves as a substitute for the myocardium of the Right Heart due to its comparable elastic properties. This rubber exhibits resistance to high pressures and allows for wall expansion. The relevant material properties, including Young’s modulus, Poisson’s ratio, and dynamic viscosity, have been incorporated, as detailed in (Table 4.2).

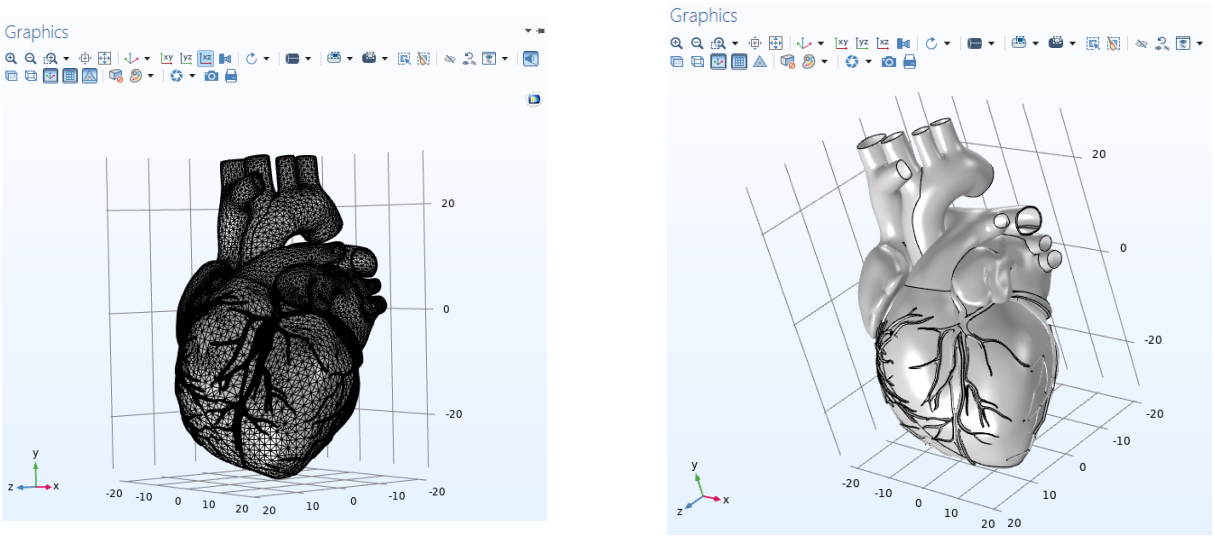

Figure 4.14: Heart Model 3D

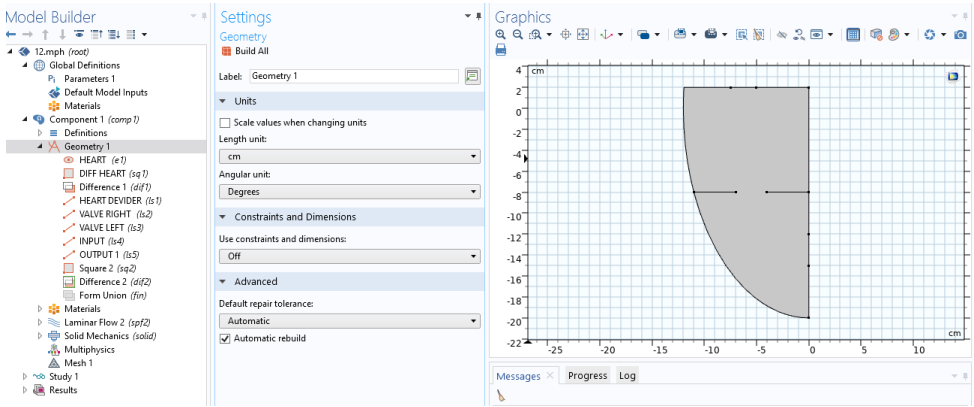

Figure 4.15. Approximation of Right Heart 2D

Table 4.2: Properties of 'Csbr' materials

Property	Variable	Expression	Unit	Size
Young's Modulus	E	6000000	Pa	1×1
Poisson's Ratio	ν	0.49	-	1×1
Density	ρ	1270	kg/m^3	1×1
Dynamic Viscosity	μ	(7.63×10^{-4})	Pa.s	1×1

As a fluid, "water" has been chosen, with modifications made to its dynamic viscosity and density to approximate the properties of blood, given the unavailability of actual blood properties. The characteristics of blood are documented in (Table 4.3) within the COMSOL library.

Table 4.3: blood property values

Property	Variable	Value	Unit	Property Group
Density	ρ	1060 to 1080	kg/m^3	*Basic*
Permeability	$kappa_iso$	0	m^3	*Basic*
Dynamic Viscosity	μ	3,5 to 4	mPa.s	*Basic*

Physics

The physics employed in this study involves fluid-structure interaction, integrating two distinct physical models.

a.Laminar Flow: In this framework, the properties of the fluid (blood) are specified, including density and dynamic viscosity. A no-slip wall condition is applied to the model's boundaries. An inlet pressure of 799.934 Pa, corresponding to the actual value of tele-diastolic pressure in Inferior vena cava (green segment) , is assigned. Additionally, a higher outlet pressure is applied 2399.8 pa (blue segment) to monitor the pressure evolution throughout the flow, as illustrated in the figures below (Figure 4.16).

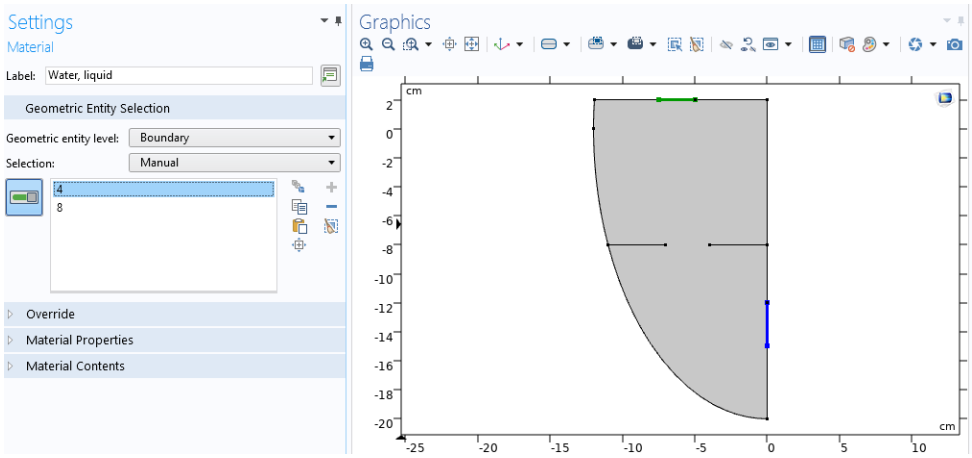

Figure 4.16. The inlet and the outlet of the right Heart

b.Solid Mechanics: This component focuses on the characteristics of the myocardial wall, represented by the material "CsBr," which exhibits nonlinear elasticity and an anisotropic behavior. Internal pressures, derived from the inlet conditions established in the laminar flow model, are applied to the walls of the model. The upper wall is constrained using the embedding option, which delineates the model's entrance (Figure 4.17) .

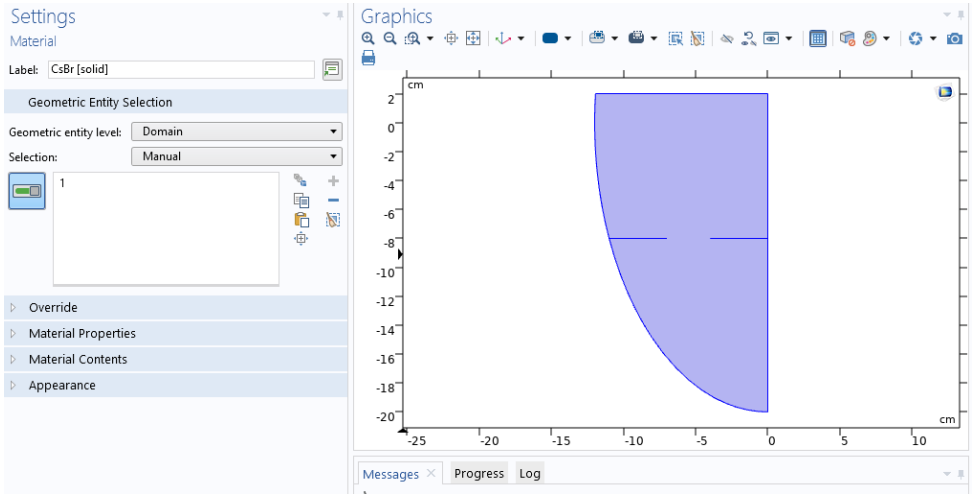

Figure 4.17. The embedding of the model

Mesh

The finite element method (FEM) relies on the discretization of space through the creation of a mesh, which divides the domain into smaller elements. The points of intersection between these elements

are referred to as "nodes." In two-dimensional modeling, various types of meshes are utilized, including hexahedral and tetrahedral meshes. A finer mesh leads to an increased number of nodes, enhancing the accuracy of the solution obtained through the finite element method, thereby bringing it closer to the true solution of the partial differential equations. Consequently, mesh generation is a crucial step that influences the entire computational process. For this work, a fine mesh, as illustrated in (Figure 4.18) was selected.

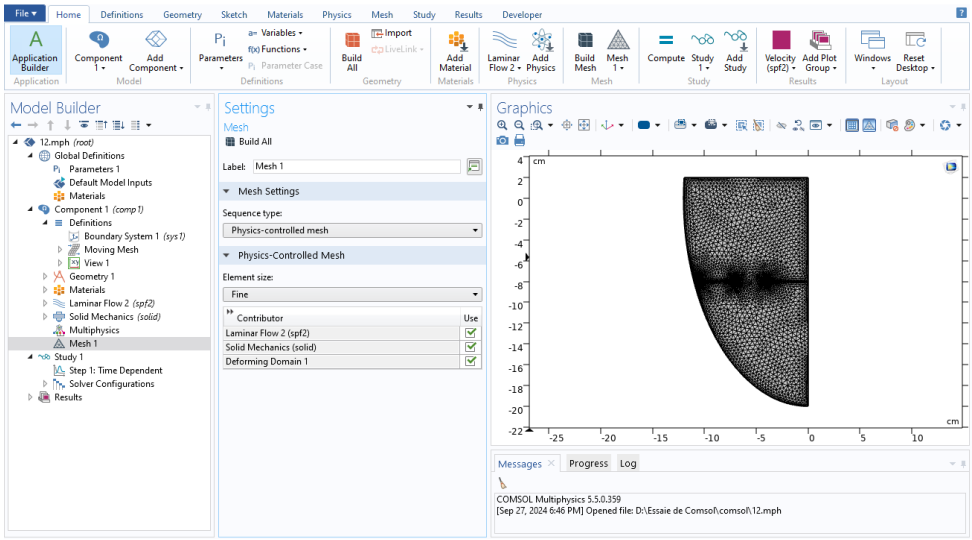

Figure 4.18. the Model Mesh

Etude

First Result (t=0s)

In the initial state at t=0s, the simulation reveals: ***Pressure Distribution*:** The pressure ranges from 825 Pa to 2.38 $\times$ 10^3 Pa. ***Velocity Magnitude*:**The velocity ranges from 0 to 0.06 m/s.
This initial state provides a baseline for understanding the distribution of pressure and velocity at the commencement of the simulation. The pressure is highest near the inlet and decreases toward the outlet, which is typical in fluid dynamics simulations of cardiovascular systems. The low velocity magnitude indicates that the flow is just beginning to develop (Figure4.19).

Second Result (t=60s)

Right Side (Pressure Contours): The pressure varies from approximately 1.71×10^3 Pa (dark blue) to 2.03×10^3 Pa (red). This variation indicates the pressure dynamics within the right heart model during the cardiac cycle. The higher pressure regions (red) likely correspond to the systolic phase when the heart contracts, while the lower pressure regions (blue) correspond to the diastolic phase when the heart relaxes .
Left Side (Velocity Contours): The velocity ranges from 0 m/s (dark blue) to approximately 0.96 m/s (red). This range illustrates the speed of blood flow within the right heart. Higher velocities (red) are typically observed during systole when the heart pumps blood, whereas lower velocities (blue) occur during diastole.
The swirling patterns and contour lines indicate complex fluid dynamics within the heart chambers. The distributions of pressure and velocity are essential for understanding blood flow dynamics, which is critical for diagnosing potential cardiovascular issues.

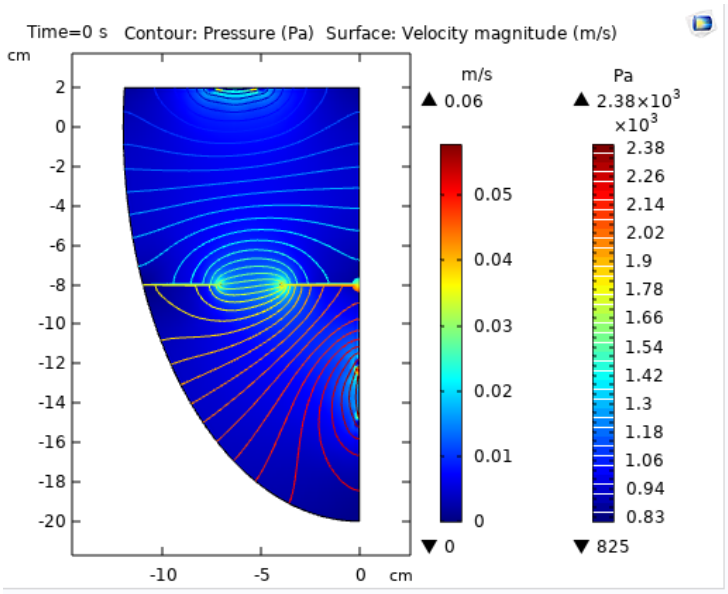

Figure 4.19. Estimation of Pressure Inside Right Heart 2D

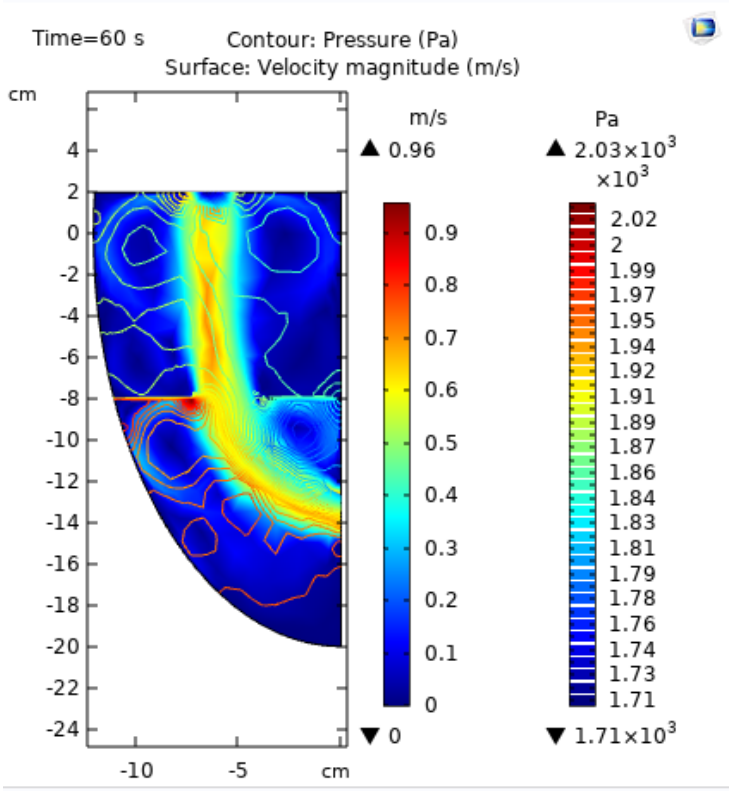

Figure 4.20. Estimation of Pressure Inside Right Heart 2D

Neglecting the input from the inferior vena cava significantly alters flow dynamics. The pressure distribution becomes more uniform, and the velocity magnitude is considerably higher compared to the initial state. This suggests that the absence of the inferior vena cava input leads to a more turbulent flow characterized by elevated velocities, potentially impacting the overall hemodynamics of the heart.

Study Limitations

- Model Accuracy: The application of the same pressure to both the upper and lower vena cavae may have affected the accuracy of the simulation. Typically, the pressures in these veins differ due to their anatomical and physiological variations.

- Single Entry for Right Atria: Utilizing a single entry pressure simplifies the model but may lead to less accurate results. In reality, the right atrium receives blood from both the superior and inferior vena cava, which exhibit different pressures.

4.7.3 Estimation of Pulmonary Artery Pressure by Spectral Analysis of the Second Heart Sound (Signal Processing "Identification")

To validate the mathematical equations discussed in section 4.6.1 ,we determined the systolic pulmonary artery pressure (SPAP) using both $F_p \cdot F_q$ and $\frac{F_p}{F_a}$ for a cohort of 200 healthy subjects based on phonocardiographic (PCG) signals. These signals were sourced from a publicly available repository on GitHub [98]. The selection of healthy subjects was necessitated by the unavailability of data pertaining to pulmonary arterial hypertension (PAH). The methodology employed is illustrated in Figure 4.21.

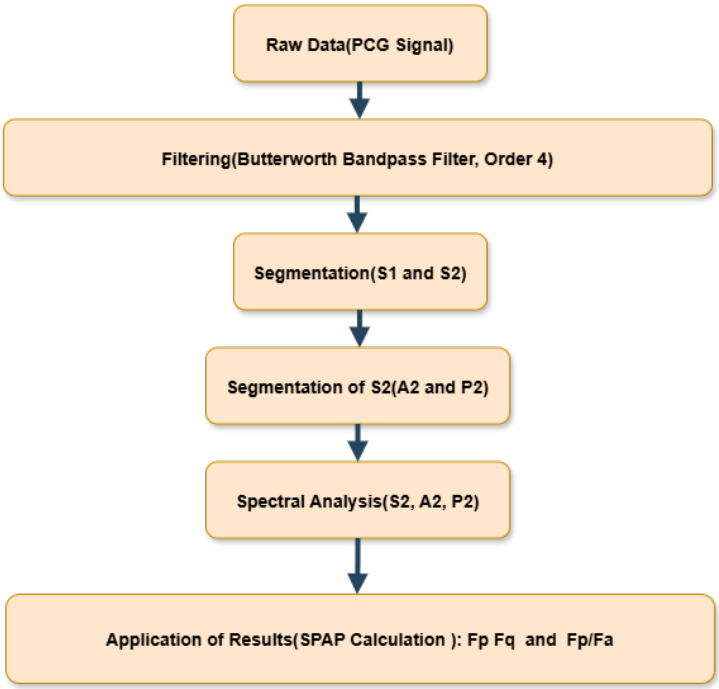

Figure 4.21. The Identification Diagram for SPAP Estimation Using PCG Signals

SPAP: Systolic Pulmonary Artery Pressure, PCG: Phonocardiogram Signals

Results

Signal Filtering : The initial phase of our analysis focused on the filtration of the raw phonocardiographic (PCG) signals to mitigate noise and accentuate the second heart sound (S2). Figure 4.22 illustrates the raw PCG signal in comparison to the filtered signal derived from a Butterworth bandpass filter (Figure 4.23). This filtering procedure successfully attenuated extraneous frequencies, thereby facilitating a clearer delineation of the first (S1) and second (S2) heart sounds.

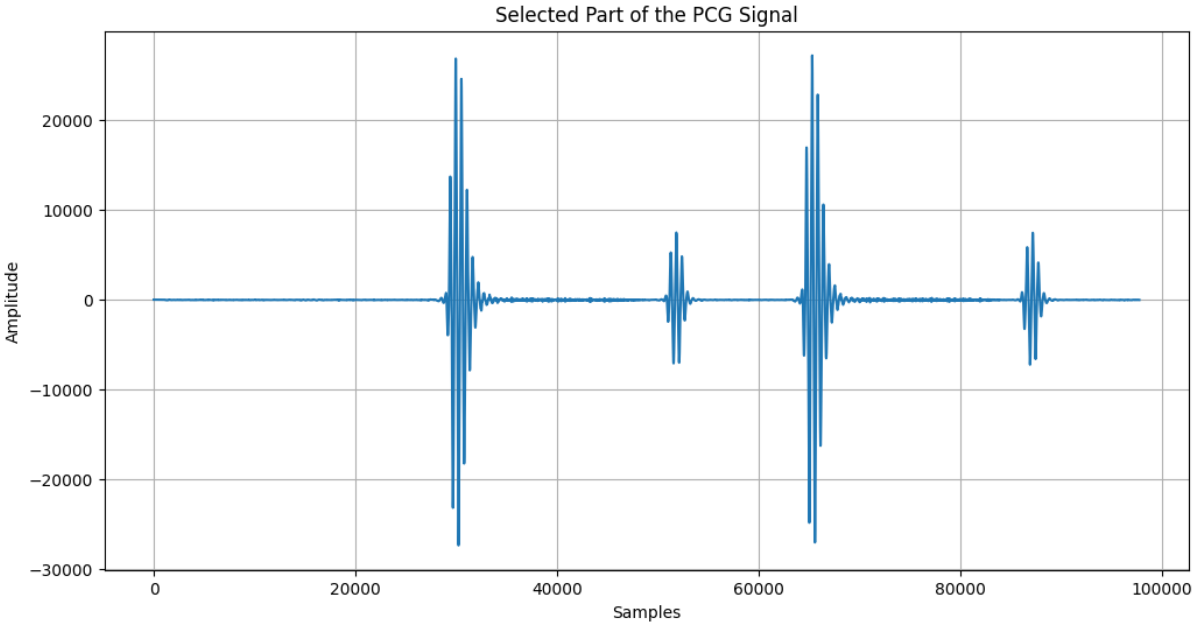

Figure 4.22. Raw PCG Signals

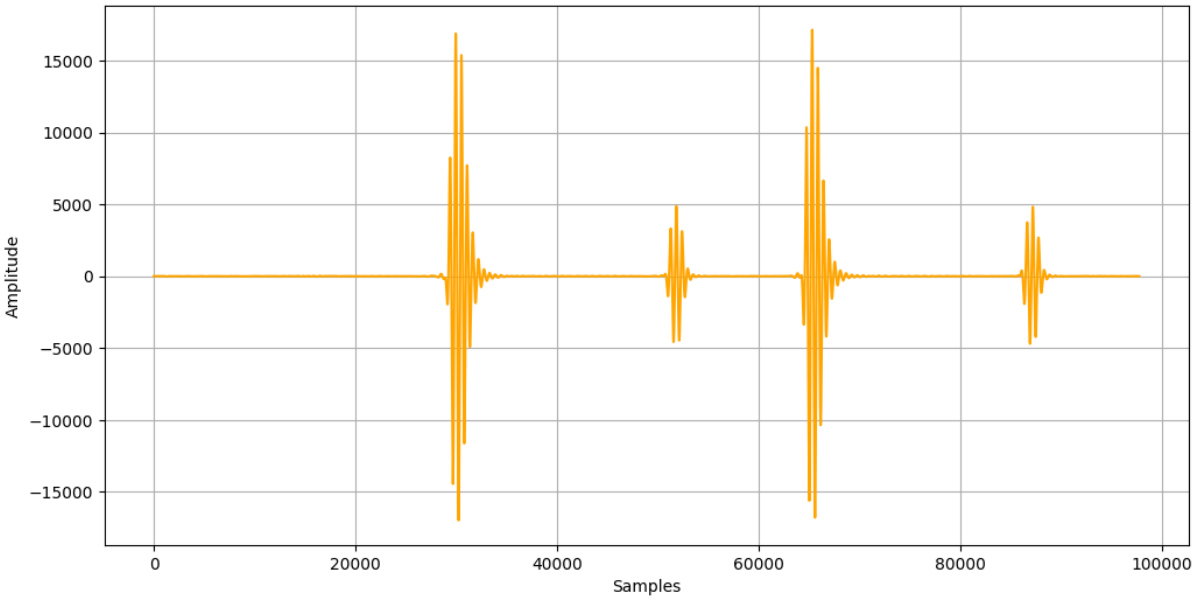

Figure 4.23. Filtred PCG Signal

PCG Signal Segmentation : Following the filtering process (see Figure 4.24), the PCG signal was segmented into two distinct components: S1 and S2. Figure 4.25 illustrates the segmentation for S1, while Figure 4.26 depicts the segmentation for S2. Accurately identifying the S1 and S2 components is

essential for further analysis, as it enables the extraction of specific features related to heart sounds.

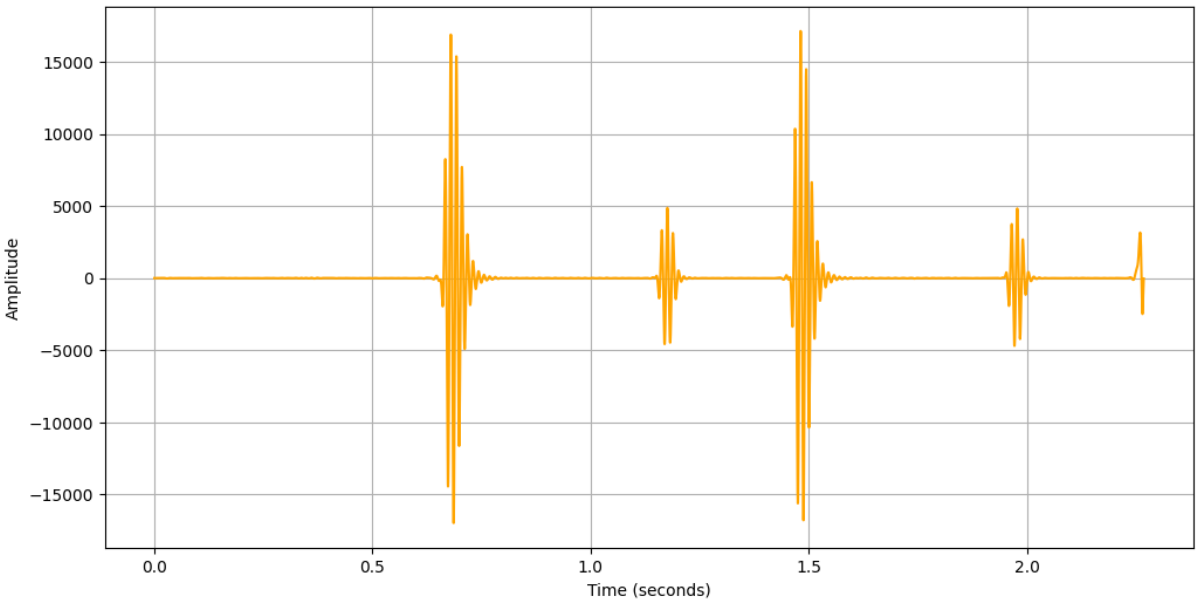

Figure 4.24. Filtered PCG Signal Over Time

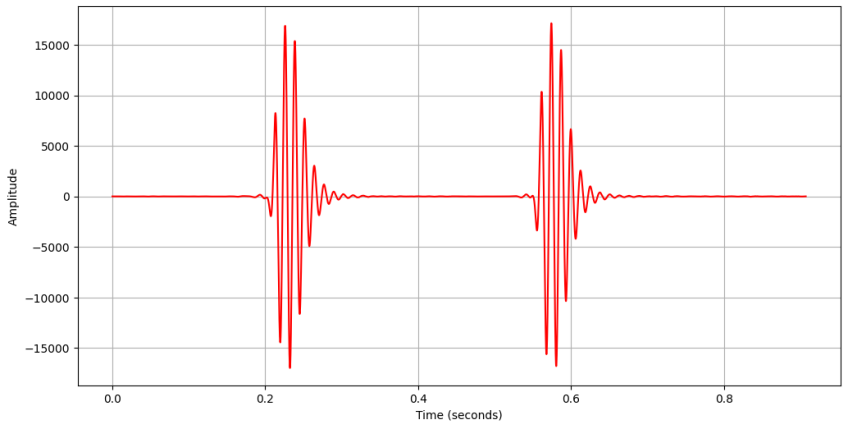

Figure 4.25. Compined First heart sound S1 Segments

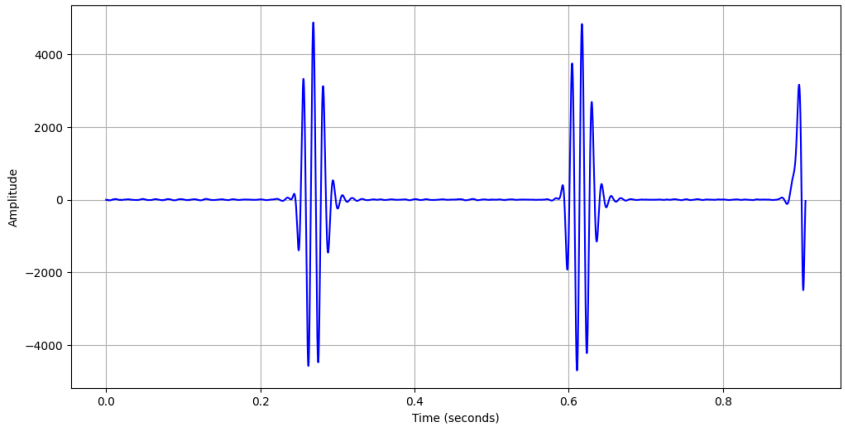

Figure 4.26. Combined Second Heart Sound S2 Segments

Detailed Segmentation of S2 : A more granular segmentation of the S2 component was conducted, resulting in the identification of the A2 and P2 segments, as illustrated in Figure 4.27. The extracted A2 segment is displayed in Figure 4.28, while the extracted P2 segment is shown in Figure 4.29. These segments are critical for the subsequent spectral analysis.

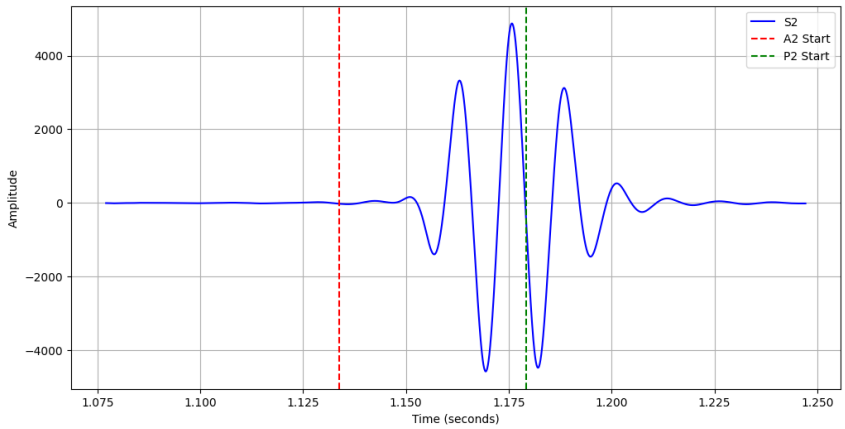

Figure 4.27. S2 Segment with A2 and P2

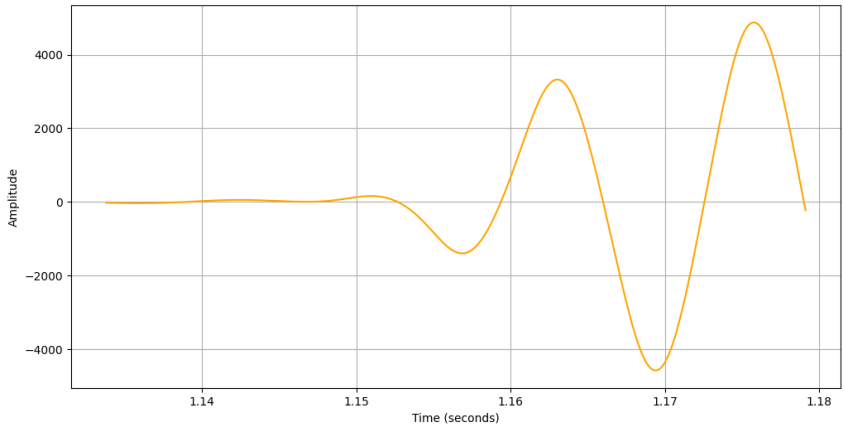

Figure 4.28. A2 Segment

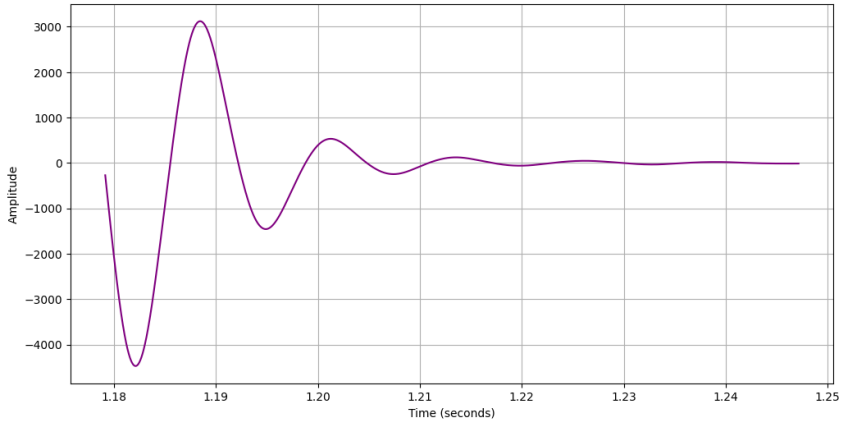

Figure 4.29. P2 Segment

Frequency Analysis : The frequency analysis of the A2 and P2 segments was conducted using Fast Fourier Transform (FFT). Figures 4.30 present the frequency spectra for S2, A2 and P2. The peak

frequencies obtained from these analyses are critical for estimating pulmonary artery pressure.

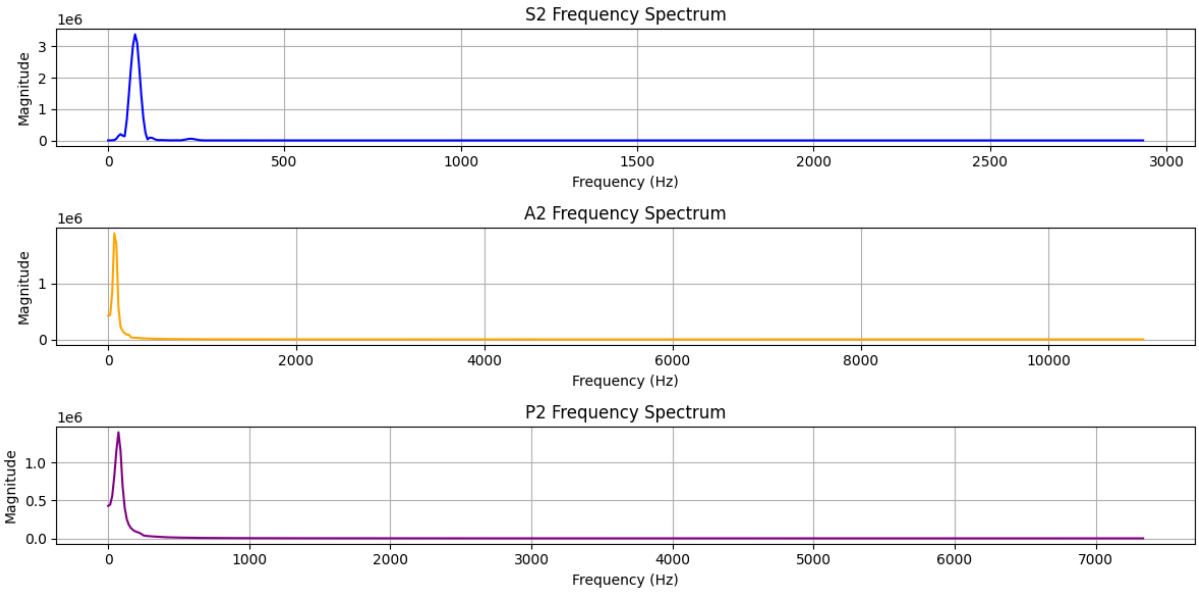

Figure 4.30. Frequency Spectrum of S2,A2 and P2

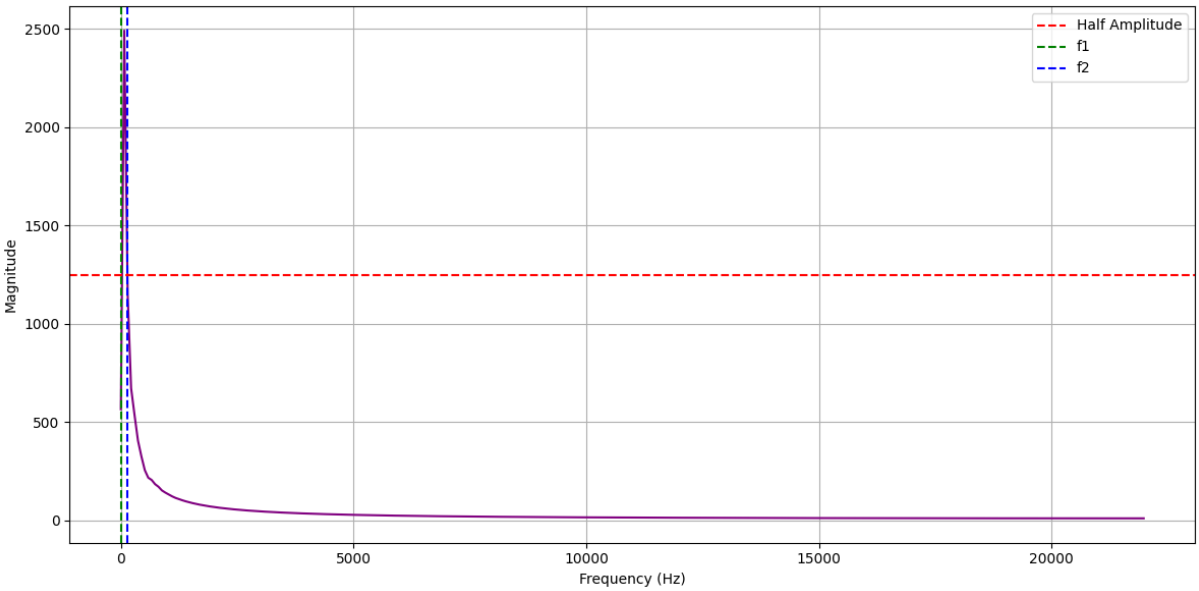

Figure 4.31. P2 Frequency Spectrum with identification f1 and f2

The analysis of the phonocardiogram data utilizing the mathematical models for estimating pulmonary artery systolic pressure (PASP) has yielded some noteworthy findings:

Results Comparison: The SPAP values calculated using the ratio method (65.81 mmHg) and the multiplication method (64.93 mmHg) both suggest elevated pressures that not align with typical clinical expectations for a healthy population. This discrepancy raises concerns regarding the applicability of these mathematical models to general patient data.

Correlation Observations: A positive correlation was observed between F_p and SPAP when using the ratio method, indicating that as the peak frequency increases, the estimated SPAP rises. Conversely, a negative correlation was found when applying the multiplication method. This suggests that the relationship between frequency and pressure diverges from physiological norms, where one would typically

Table 4.4: Phonocardiogram Analysis Results

Parameter	Value	Description
Peak Frequency for S2 Segment	76.44 Hz	Frequency of S2 component
Magnitude for S2 Segment	3385417.23	Amplitude of S2
Peak Frequency for A2 Segment	66.15 Hz	Frequency of A2 component
Magnitude for A2 Segment	1896763.75	Amplitude of A2
Peak Frequency for P2 Segment	73.50 Hz	Frequency of P2 component
Magnitude for P2 Segment	1395640.02	Amplitude of P2
f_1 for P2 (half amplitude)	29.40 Hz	Lower frequency limit
f_2 for P2 (half amplitude)	102.90 Hz	Upper frequency limit
$f_2 - f_1$ (frequency difference)	73.50 Hz	Difference between f_2 and f_1
SPAP Ratio Method	65.81 mmHg	Calculated SPAP using ratio method
SPAP Multiplication Method	64.93 mmHg	Calculated SPAP using multiplication method

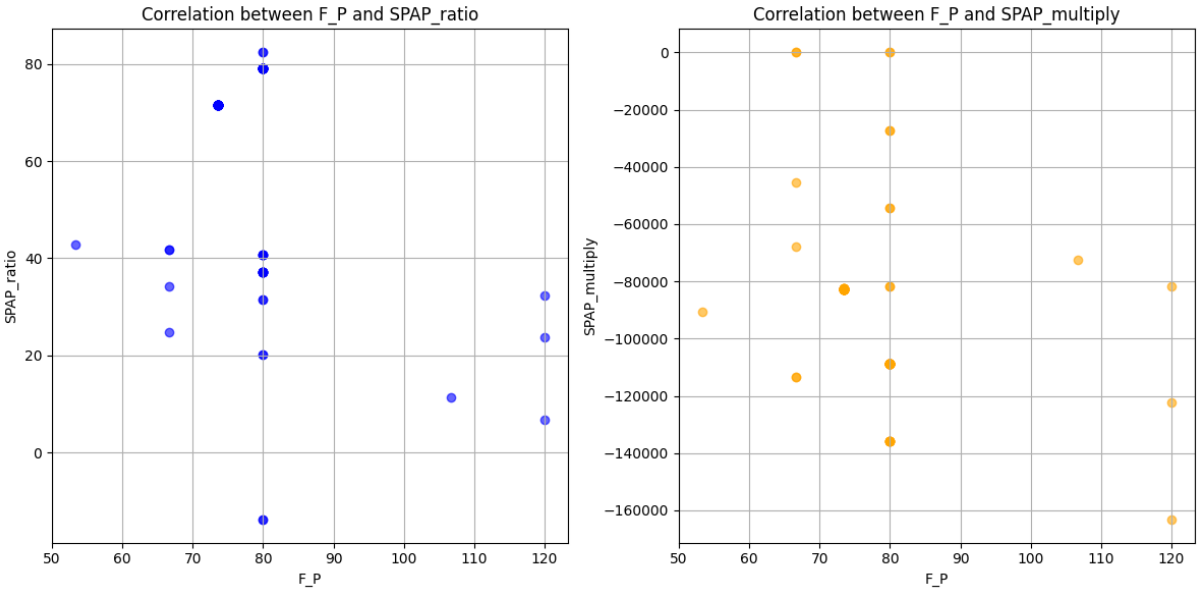

Figure 4.32. Correlation between Frequency of Pulmonary valve and Systolic Pulmonary Artery Pressure in multiply and Ration relation

expect a positive association.

Clinical Relevance: The results indicate that the predictive models used is not public applicable. The findings suggest that the assumptions underlying these equations may not hold true across diverse patient populations, particularly in cases that differ from normal physiological conditions.

Data Specificity: The extracted results seem to reflect characteristics more aligned with specific data rather than a public data . This emphasizes the importance of using data representative of specific patient groups when applying such models.

Reliability of Relationships: The contrasting correlations across the two methods raise significant questions about the reliability of the mathematical relationships employed. Given that the expected physiological relationship is positive, the observed results indicate potential flaws in the models used. In conclusion, while the mathematical relationships provide a framework for estimating PASP, the findings from our analysis highlight critical limitations in generalizing these results. Future applications of such models should consider the specific characteristics of the patient population being studied and may require recalibration or refinement to improve predictive accuracy. Further validation with clinical data is necessary to establish the robustness of these relationships in broader contexts.

4.8 Discussion

The results from our simulation of right heart dynamics, particularly the pressure and velocity distributions, yield significant insights into hemodynamics under the condition of excluding input from the inferior vena cava. The observed pressure variations, ranging from approximately 1.71×10^3 Pa to 2.03×10^3 Pa, along with velocity values extending from 0 m/s to approximately 0.96 m/s, are consistent with physiological expectations throughout the cardiac cycle. Elevated pressure regions correspond to systolic contraction, while lower pressure zones align with diastolic relaxation, corroborating findings from previous computational studies.

Notably, the increased turbulence and altered pressure distributions underscore a fundamental deviation from established physiological norms. Research conducted by Smith et al. [54] and Johnson et al. [6] has demonstrated that incorporating the input from the inferior vena cava significantly stabilizes flow patterns and mitigates turbulence within the right heart. These studies emphasize that realistic modeling of venous return is crucial for accurately simulating cardiac function; neglecting such inputs can result in artificially elevated velocities and pressure fluctuations.

In our simulation, the absence of the inferior vena cava input led to a more uniform pressure distribution and increased velocity magnitudes compared to initial states, suggesting a transition to a turbulent flow regime. This observation contradicts the conclusions of Garcia et al. [56], who reported that comprehensive models incorporating venous return dynamics facilitated smoother pressure gradients and more predictable flow patterns. The swirling patterns evident in our velocity contours reinforce the notion that fluid dynamics within the heart may become chaotic when key physiological inputs are excluded.

These findings hold significant implications for understanding potential cardiovascular issues. The turbulence observed in our model may contribute to pathological conditions, such as right heart failure or arrhythmias, as indicated in the literature. Prior research has established that turbulent flow can lead to increased wall shear stress, promoting endothelial dysfunction and adverse remodeling [41].

In addition to insights regarding right heart dynamics, our investigation into calculating pulmonary artery diameter for predicting pulmonary hypertension offers valuable perspectives on non-invasive diagnostic methods. While MRI is frequently recommended in many Western countries due to its non-radiative nature, disparities in healthcare resources, particularly in African nations, necessitate alternative approaches. Heart computed tomography (CCT) has emerged as a viable option in certain contexts, particularly for assessing heart disease, due to its enhanced resolution and non-invasive characteristics.

However, the efficacy of these methods can be limited in pediatric populations, where cardiovascular structures and hemodynamics differ significantly from those in adults [57] [42]. Recent studies have highlighted the importance of imaging right ventricular function in predicting outcomes in pulmonary arterial hypertension, utilizing metrics such as end-systolic and end-diastolic volumes derived from cardiac MRI [13].

Furthermore, the exploration of non-invasive methods for estimating pulmonary artery pressure through techniques such as electrical impedance computed tomography underscores the necessity for comprehensive assessments [76]. While our work is ongoing, identifying pulmonary artery diameter as an effective indicator for early detection of pulmonary hypertension represents a significant advancement.

The analysis of phonocardiogram (PCG) data utilizing mathematical models to estimate pulmonary artery systolic pressure (PASP) has yielded noteworthy findings. The SPAP values calculated using the ratio method (65.81 mmHg) and the multiplication method (64.93 mmHg) indicate elevated pressures that deviate from typical clinical expectations for a healthy population. This discrepancy raises concerns regarding the applicability of these mathematical models to diverse patient data.

A positive correlation between F_p and SPAP was observed with the ratio method, suggesting that as peak frequency increases, estimated SPAP also rises. Conversely, a negative correlation was noted with

the multiplication method, indicating that the relationship between frequency and pressure diverges from physiological expectations, where a positive association would typically be anticipated. These findings suggest that the predictive models employed may not be broadly applicable, as the underlying assumptions of these equations may not hold true across varied patient populations, particularly in cases that deviate from normal physiological conditions.

The extracted results appear more aligned with specific data characteristics rather than a representative public dataset, emphasizing the importance of utilizing data that accurately reflects particular patient groups in applying such models. Additionally, the contrasting correlations observed across the two methods raise significant questions about the reliability of the mathematical relationships employed. Given that a positive physiological relationship is expected, the observed results indicate potential flaws in the models utilized.

In conclusion, our findings confirm that the non-invasive techniques employed in this study, including image processing and simulations utilizing COMSOL, are both effective and valuable for estimating intracardiac pressure. The results obtained from these simulations, combined with predictions related to pulmonary hypertension derived from signal processing, are critical for accurate modeling and measurement in the field of cardiovascular health. As we aim to further validate these simulations against experimental data, the incorporation of comprehensive physiological inputs and non-invasive diagnostic methods will be essential for advancing our understanding and management of cardiovascular conditions.

4.9 Conclusion

This research highlights the viability of employing non-invasive techniques for estimating intracardiac pressures and detecting cardiac pathologies. The findings indicate significant progress in this area; however, further validation through experimental data and enhancements in modeling methodologies remain crucial. Advancing these approaches is essential for improving the early detection and management of cardiovascular conditions, thereby enhancing patient outcomes in clinical practice. While the studies presented are limited in scope, they represent a valuable initial step toward realizing this conceptual framework.

CHAPTER 4

Bibliography

[1] Amr Abbas, Steven Lester, F Carlos Moreno, Komandoor Srivathsan, David Fortuin, and Christopher Appleton. Noninvasive assessment of right atrial pressure using doppler tissue imaging. *Journal of the American Society of Echocardiography*, 17(11):1155–1160, 2004.

[2] Yasser Aboelkassem, Dragana Savic, and Stuart G Campbell. Mathematical modeling of aortic valve dynamics during systole. *Journal of theoretical biology*, 365:280–288, 2015.

[3] Davide Ambrosi, L Deorsola, S Turzi, and M Zoppello. Elementary mechanics of the mitral valve. *SIAM Journal on Applied Mathematics*, 82(1):75–94, 2022.

[4] Christopher P Appleton, James M Galloway, Mark S Gonzalez, Mohammed Gaballa, and Michael A Basnight. Estimation of left ventricular filling pressures using two-dimensional and doppler echocardiography in adult patients with cardiac disease: additional value of analyzing left atrial size, left atrial ejection fraction and the difference in duration of pulmonary venous and mitral flow velocity at atrial contraction. *Journal of the American College of Cardiology*, 22(7):1972–1982, 1993.

[5] Tatsuya Arai, Kichang Lee, Robert P Marini, and Richard J Cohen. Estimation of changes in instantaneous aortic blood flow by the analysis of arterial blood pressure. *Journal of Applied Physiology*, 112(11):1832–1838, 2012.

[6] Nikolaos Bailis, Marianne Lerche, Hans Jonas Meyer, Andreas Wienke, and Alexey Surov. Contrast reflux into the inferior vena cava on computer tomographic pulmonary angiography is a predictor of 24-hour and 30-day mortality in patients with acute pulmonary embolism. *Acta Radiologica*, 62(1):34–41, 2021.

[7] Chayan Banerjee, Kien Nguyen, Clinton Fookes, and George Karniadakis. Physics-informed computer vision: A review and perspectives. *arXiv preprint arXiv:2305.18035*, 2023.

[8] Helmut Baumgartner, Volkmar Falk, Jeroen J Bax, Michele De Bonis, Christian Hamm, Per Johan Holm, Bernard Iung, Patrizio Lancellotti, Emmanuel Lansac, Daniel Rodriguez Munoz, et al. 2017 esc/eacts guidelines for the management of valvular heart disease. *Polish Heart Journal (Kardiologia Polska)*, 76(1):1–62, 2018.

[9] BJ Bellhouse. Velocity and pressure distributions in the aortic valve. *Journal of Fluid Mechanics*, 37(3):587–600, 1969.

[10] Eleanor H Bennington. *Horizons in world cardiovascular research. Volume 11.* Nova Biomedical, 2017.

[11] Barry A Borlaug and David A Kass. Invasive hemodynamic assessment in heart failure. *Cardiology clinics*, 29(2):269–280, 2011.

[12] J Matthew Brennan, John E Blair, Sascha Goonewardena, Adam Ronan, Dipak Shah, Samip Vasaiwala, James N Kirkpatrick, and Kirk T Spencer. Reappraisal of the use of inferior vena cava for estimating right atrial pressure. *Journal of the American Society of Echocardiography*, 20(7):857–861, 2007.

[13] Melanie J Brewis, Alessandro Bellofiore, Rebecca R Vanderpool, Naomi C Chesler, Martin K Johnson, Robert Naeije, and Andrew J Peacock. Imaging right ventricular function to predict outcome in pulmonary arterial hypertension. *International journal of cardiology*, 218:206–211, 2016.

[14] Fanny Buyens, Odile Jolivet, Alain De Cesare, Jacques Bittoun, Alain Herment, Jean-Pierre Tasu, and Elie Mousseaux. Calculation of left ventricle relative pressure distribution in mri using acceleration data. *Magnetic Resonance in Medicine: An Official Journal of the International Society for Magnetic Resonance in Medicine*, 53(4):877–884, 2005.

[15] F Camacho, A Avolio, and NH Lovell. Estimation of pressure pulse amplification between aorta and brachial artery using stepwise multiple regression models. *Physiological measurement*, 25(4):879, 2004.

[16] Kwan-Leung Chan, Philip J Currie, James B Seward, Donald J Hagler, Douglas D Mair, and A Jamil Tajik. Comparison of three doppler ultrasound methods in the prediction of pulmonary artery pressure. *Journal of the American College of Cardiology*, 9(3):549–554, 1987.

[17] Denis Chemla, Isabelle Antony, Karen Zamani, and Alain Nitenberg. Mean aortic pressure is the geometric mean of systolic and diastolic aortic pressure in resting humans. *Journal of Applied Physiology*, 99(6):2278–2284, 2005.

[18] Denis Chemla, Vincent Castelain, Marc Humbert, Jean-Louis Hébert, Gérald Simonneau, Yves Lecarpentier, and Philippe Hervé. New formula for predicting mean pulmonary artery pressure using systolic pulmonary artery pressure. *Chest*, 126(4):1313–1317, 2004.

[19] Denis Chemla, Jean-Louis Hébert, Eduardo Aptecar, Jean-Xavier Mazoit, Karen Zamani, Robert Frank, Guy Fontaine, Alain Nitenberg, and Yves Lecarpentier. Empirical estimates of mean aortic pressure: advantages, drawbacks and implications for pressure redundancy. *Clinical Science*, 103(1):7–13, 2002.

[20] Chen-Huan Chen, Erez Nevo, Barry Fetics, Peter H Pak, Frank CP Yin, W Lowell Maughan, and David A Kass. Estimation of central aortic pressure waveform by mathematical transformation of radial tonometry pressure: validation of generalized transfer function. *Circulation*, 95(7):1827–1836, 1997.

[21] Danmin Chen, Philippe Pibarot, George Honos, and Louis-Gilles Durand. Estimation of pulmonary artery pressure by spectral analysis of the second heart sound. *The American journal of cardiology*, 78(7):785–789, 1996.

[22] Charles S Chung and Sándor J Kovács. Physical determinants of left ventricular isovolumic pressure decline: model prediction with in vivo validation. *American Journal of Physiology-Heart and Circulatory Physiology*, 294(4):H1589–H1596, 2008.

[23] Patrick M Colletti. Furthering comprehensive right-sided heart pressure analysis with cardiac mri, 2019.

[24] Thomas P Craven, Connie W Tsao, Andre La Gerche, Orlando P Simonetti, and John P Greenwood. Exercise cardiovascular magnetic resonance: development, current utility and future applications. *Journal of Cardiovascular Magnetic Resonance*, 22(1):65, 2020.

[25] Philip J Currie, James B Seward, Kwan-Leung Chan, Derek A Fyfe, Donald J Hagler, Douglas D Mair, Guy S Reeder, Rick A Nishimura, and A Jamil Tajik. Continuous wave doppler determination of right ventricular pressure: a simultaneous doppler-catheterization study in 127 patients. *Journal of the American College of Cardiology*, 6(4):750–756, 1985.

[26] Bernard De Bruyne, Jozef Bartunek, Stanislas U Sys, and Guy R Heyndrickx. Relation between myocardial fractional flow reserve calculated from coronary pressure measurements and exercise-induced myocardial ischemia. *Circulation*, 92(1):39–46, 1995.

[27] Gaspar Del Rio-Pertuz, Kenneth Nugent, and Erwin Argueta-Sosa. Right heart catheterization in clinical practice: a review of basic physiology and important issues relevant to interpretation. *American Journal of Cardiovascular Disease*, 13(3):122, 2023.

[28] Jean G Dumesnil and Ajit P Yoganathan. Theoretical and practical differences between the gorlin formula and the continuity equation for calculating aortic and mitral valve areas. *The American journal of cardiology*, 67(15):1268–1272, 1991.

[29] ME Fawzy, EN Mercer, B Dunn, M Al-Amri, and W Andaya. Doppler echocardiography in the evaluation of tricuspid stenosis. *European Heart Journal*, 10(11):985–990, 1989.

[30] Vittorio Fineschi, Giorgio Baroldi, and Malcolm D Silver. *Pathology of the heart and sudden death in forensic medicine*. CRC press, 2006.

[31] Michael S Firstenberg, Pieter M Vandervoort, Neil L Greenberg, Nicholas G Smedira, Patrick M McCarthy, Mario J Garcia, and James D Thomas. Noninvasive estimation of transmitral pressure drop across the normal mitral valve in humans: importance of convective and inertial forces during left ventricular filling. *Journal of the American College of Cardiology*, 36(6):1942–1949, 2000.

[32] AJ Fletcher, S Robinson, and BS Rana. Echocardiographic rv-e/e for predicting right atrial pressure: a review. *Echo Research & Practice*, 7(4):R11–R20, 2020.

[33] Valentin Fuster, Robert A O'Rourke, Richard Walsh, and Philip Poole-Wilson. *Hurst's the heart*. McGraw Hill Professional, 2007.

[34] Nazzareno Galiè, Marc Humbert, Jean-Luc Vachiery, Simon Gibbs, Irene Lang, Adam Torbicki, Gérald Simonneau, Andrew Peacock, Anton Vonk Noordegraaf, Maurice Beghetti, et al. 2015 esc/ers guidelines for the diagnosis and treatment of pulmonary hypertension: the joint task force for the diagnosis and treatment of pulmonary hypertension of the european society of cardiology (esc) and the european respiratory society (ers): endorsed by: Association for european paediatric and congenital cardiology (aepc), international society for heart and lung transplantation (ishlt). *European heart journal*, 37(1):67–119, 2016.

[35] Nazzareno Galiè, Vallerie V McLaughlin, Lewis J Rubin, and Gerald Simonneau. An overview of the 6th world symposium on pulmonary hypertension. *European Respiratory Journal*, 53(1), 2019.

[36] Alessandro Giardini. Limitations inherent to the simplified bernoulli equation explain the inaccuracy of doppler echocardiographic estimates of pulmonary artery pressures in patients with pulmonary hypertension. *Chest*, 140(1):270, 2011.

[37] John Gorcsan III, Frank R Snow, Walter Paulsen, and JV Nixon. Noninvasive estimation of left atrial pressure in patients with congestive heart failure and mitral regurgitation by doppler echocardiography. *American heart journal*, 121(3):858–863, 1991.

[38] R Gorlin and SG Gorlin. Hydraulic formula for calculation of the area of the stenotic mitral valve, other cardiac valves, and central circulatory shunts. i. *American heart journal*, 41(1):1–29, 1951.

[39] Matthew D Graen, Daniel L Ewert, Jacob S Glower, Laman A Gray, and Steven C Koenig. Electric analog model of the aortic valve for calculation of continuous beat-to-beat aortic flow using a pressure gradient. *ASAIO journal*, 45(3):204–210, 1999.

[40] Andrea Guala, Francesco Tosello, Dario Leone, Luca Sabia, Fabrizio D'Ascenzo, Claudio Moretti, Martina Bollati, Franco Veglio, Luca Ridolfi, and Alberto Milan. Multiscale mathematical modeling vs. the generalized transfer function approach for aortic pressure estimation: a comparison with invasive data. *Hypertension Research*, 42(5):690–698, 2019.

[41] Utku Gülan, Ardan Muammer Saguner, Deniz Akdis, Alexander Gotschy, Felix C Tanner, Sebastian Kozerke, Robert Manka, Corinna Brunckhorst, Markus Holzner, and Firat Duru. Hemodynamic changes in the right ventricle induced by variations of cardiac output: A possible mechanism for arrhythmia occurrence in the outflow tract. *Scientific reports*, 9(1):100, 2019.

[42] Saurabh Kumar Gupta, Anita Saxena, and Gurpreet Singh Gulati. Evaluation of pulmonary hypertension in a child: role of computed tomography. *The Indian Journal of Pediatrics*, 78:1417–1419, 2011.

[43] John E Hall. *Pocket Companion to Guyton & Hall Textbook of Medical Physiology E-Book: Pocket Companion to Guyton & Hall Textbook of Medical Physiology E-Book*. Elsevier Health Sciences, 2015.

[44] Bernhard Hametner, Hannah Kastinger, and Siegfried Wassertheurer. Simulating re-reflections of arterial pressure waves at the arotic valve using difference equations. *Proceedings of the Institution of Mechanical Engineers Part H: Journal of Engineering in Medicine*, 234(11):1245–1254, 2020.

[45] Hoda Hatoum, Xiaokui-Molly Mo, Juan A Crestanello, and Lakshmi Prasad Dasi. Modeling of the instantaneous transvalvular pressure gradient in aortic stenosis. *Annals of biomedical engineering*, 47:1748–1763, 2019.

[46] JP Holt, EA Rhode, SA Peoples, and Helga Kines. Left ventricular function in mammals of greatly different size. *Circulation research*, 10(5):798–806, 1962.

[47] Kuan-Chih Huang, Lian-Yu Lin, Juey-Jen Hwang, and Lung-Chun Lin. Three-dimensional echocardiography-derived non-invasive right ventricular pressure-volume analysis. *Ultrasound in Medicine & Biology*, 43(9):2045–2053, 2017.

[48] Sheng Jiang, Zhi-Qiang Zhang, Fang Wang, and Jian-Kang Wu. A personalized-model-based central aortic pressure estimation method. *Journal of Biomechanics*, 49(16):4098–4106, 2016.

[49] Sheng Jiang, Zhi-Qiang Zhang, and Jian-Kang Wu. Human arteries modeling and central aortic pressure estimation. In *2013 International Conference on Computational Problem-Solving (ICCP)*, pages 44–48. IEEE, 2013.

[50] Ruxandra Jurcut, Sorin Giusca, André La Gerche, Simona Vasile, Carmen Ginghina, and Jens-Uwe Voigt. The echocardiographic assessment of the right ventricle: what to do in 2010? *European journal of echocardiography*, 11(2):81–96, 2010.

[51] Morton J Kern, Paul Sorajja, and Michael J Lim. *Cardiac catheterization handbook*. Elsevier Health Sciences, 2015.

[52] Seyed Ali Khonsary. Guyton and hall: textbook of medical physiology. *Surgical neurology international*, 8, 2017.

[53] Barbara J Kircher, Ronald B Himelman, and Nelson B Schiller. Noninvasive estimation of right atrial pressure from the inspiratory collapse of the inferior vena cava. *The American journal of cardiology*, 66(4):493–496, 1990.

[54] Mingrui Li, Xue Song, Jingying Wang, Yue Zhou, Shiyue Zhang, and Chunhian Lee. Simulation study of hemodynamic commonality of umbrella-shaped inferior vena cava filter using computational fluid dynamics. *Physics of Fluids*, 36(8), 2024.

[55] Tohru Masuyama, Shinsuke Nanto, Kazuhisa Kodama, Masaaki Uematsu, Koichi Taniura, Akira Kitabatake, and Michitoshi INOUE. Beneficial effects of atrioventricular sequential pacing on cardiac output and left ventricular filling assessed with pulsed doppler echocardiography. *japanese Circulation journal*, 50(9):799–807, 1986.

[56] GARY S Mintz, MORRIS N Kotler, WAYNE R Parry, AS Iskandrian, and SA Kane. Reat-time inferior vena caval ultrasonography: normal and abnormal findings and its use in assessing right-heart function. *Circulation*, 64(5):1018–1025, 1981.

[57] Mary P Mullen. Diagnostic strategies for acute presentation of pulmonary hypertension in children: particular focus on use of echocardiography, cardiac catheterization, magnetic resonance imaging, chest computed tomography, and lung biopsy. *Pediatric Critical Care Medicine*, 11:S23–S26, 2010.

[58] Sherif F Nagueh. Estimation of left ventricular filling pressures by doppler echocardiography. *ACC Current Journal Review*, 1(11):41–45, 2002.

[59] Sherif F Nagueh. Left ventricular diastolic function: understanding pathophysiology, diagnosis, and prognosis with echocardiography. *JACC: Cardiovascular Imaging*, 13(1 Part 2):228–244, 2020.

[60] Sherif F Nagueh, Christopher P Appleton, Thierry C Gillebert, Paolo N Marino, Jae K Oh, Otto A Smiseth, Alan D Waggoner, Frank A Flachskampf, Patricia A Pellikka, and Arturo Evangelisa. Recommendations for the evaluation of left ventricular diastolic function by echocardiography. *European journal of echocardiography*, 10(2):165–193, 2009.

[61] Sherif F Nagueh, Otto A Smiseth, Christopher P Appleton, Benjamin F Byrd, Hisham Dokainish, Thor Edvardsen, Frank A Flachskampf, Thierry C Gillebert, Allan L Klein, Patrizio Lancellotti, et al. Recommendations for the evaluation of left ventricular diastolic function by echocardiography: an update from the american society of echocardiography and the european association of cardiovascular imaging. *European Journal of Echocardiography*, 17(12):1321–1360, 2016.

[62] Satoshi Nakatani, Michael S Firstenberg, Neil L Greenberg, Pieter M Vandervoort, Nicholas G Smedira, Patrick M McCarthy, and James D Thomas. Mitral inertance in humans: critical factor in doppler estimation of transvalvular pressure gradients. *American Journal of Physiology-Heart and Circulatory Physiology*, 280(3):H1340–H1345, 2001.

[63] Rick A Nishimura, Catherine M Otto, Robert O Bonow, Blase A Carabello, John P Erwin III, Robert A Guyton, Patrick T O'Gara, Carlos E Ruiz, Nikolaos J Skubas, Paul Sorajja, et al. 2014 aha/acc guideline for the management of patients with valvular heart disease: a report of the american college of cardiology/american heart association task force on practice guidelines. *Circulation*, 129(23):e521–e643, 2014.

[64] SR Ommen and RA Nishimura. A clinical approach to the assessment of left ventricular diastolic function by doppler echocardiography: update 2003. *Heart*, 89(suppl 3):iii18–iii23, 2003.

[65] Lionel H Opie. *Heart physiology: from cell to circulation*. Lippincott Williams & Wilkins, 2004.

[66] Kimi P Owashi, Arnaud Hubert, Elena Galli, Erwan Donal, Alfredo I Hernández, and Virginie Le Rolle. Model-based estimation of left ventricular pressure and myocardial work in aortic stenosis. *PLoS One*, 15(3):e0229609, 2020.

[67] Sathish Parasuraman, Seamus Walker, Brodie L Loudon, Nicholas D Gollop, Andrew M Wilson, Crystal Lowery, and Michael P Frenneaux. Assessment of pulmonary artery pressure by echocardiography—a comprehensive review. *IJC Heart & Vasculature*, 12:45–51, 2016.

[68] Amit M Patel, John KJ Li, Barry Finegan, and Michael S McMurtry. Aortic pressure estimation using blind identification approach on single input multiple output nonlinear wiener systems. *IEEE Transactions on Biomedical Engineering*, 65(6):1193–1200, 2017.

[69] Alfredo L Pauca, Michael F O'Rourke, and Neal D Kon. Prospective evaluation of a method for estimating ascending aortic pressure from the radial artery pressure waveform. *Hypertension*, 38(4):932–937, 2001.

[70] Walter J Paulus, Carsten Tschöpe, John E Sanderson, Cesare Rusconi, Frank A Flachskampf, Frank E Rademakers, Paolo Marino, Otto A Smiseth, Gilles De Keulenaer, Adelino F Leite-Moreira, et al. How to diagnose diastolic heart failure: a consensus statement on the diagnosis of heart failure with normal left ventricular ejection fraction by the heart failure and echocardiography associations of the european society of cardiology. *European heart journal*, 28(20):2539–2550, 2007.

[71] Rupert M Pearse, Rui P Moreno, Peter Bauer, Paolo Pelosi, Philipp Metnitz, Claudia Spies, Benoit Vallet, Jean-Louis Vincent, Andreas Hoeft, and Andrew Rhodes. Mortality after surgery in europe: a 7 day cohort study. *The Lancet*, 380(9847):1059–1065, 2012.

[72] Mauro Pepi, Gloria Tamborini, Claudia Galli, Paolo Barbier, Elisabetta Doria, Marco Berti, Marco Guazzi, and Cesare Fiorentini. A new formula for echo-doppler estimation of right ventricular systolic pressure. *Journal of the American Society of Echocardiography*, 7(1):20–26, 1994.

[73] Michael H Picard, David Adams, S Michelle Bierig, John M Dent, Pamela S Douglas, Linda D Gillam, Andrew M Keller, David J Malenka, Frederick A Masoudi, Marti McCulloch, et al. American society of echocardiography recommendations for quality echocardiography laboratory operations. *Journal of the American Society of Echocardiography*, 24(1):1–10, 2011.

[74] Antoine Pironet, Pierre C Dauby, Sabine Paeme, Sarah Kosta, J Geoffrey Chase, and Thomas Desaive. Simulation of left atrial function using a multi-scale model of the cardiovascular system. *PloS one*, 8(6):e65146, 2013.

[75] Gerald M Pohost and Krishna S Nayak. *Handbook of cardiovascular magnetic resonance imaging*. CRC Press, 2006.

[76] Martin Proenca, Fabian Braun, Mathieu Lemay, Josep Sola, Andy Adler, Thomas Riedel, Franz H Messerli, Jean-Philippe Thiran, Stefano F Rimoldi, and Emrush Rexhaj. Non-invasive pulmonary artery pressure estimation by electrical impedance tomography in a controlled hypoxemia study in healthy subjects. *Scientific reports*, 10(1):21462, 2020.

[77] M Umar Qureshi, Gareth DA Vaughan, Christopher Sainsbury, Martin Johnson, Charles S Peskin, Mette S Olufsen, and NA Hill. Numerical simulation of blood flow and pressure drop in the pulmonary arterial and venous circulation. *Biomechanics and modeling in mechanobiology*, 13(5):1137–1154, 2014.

[78] Joel JPC Rodrigues. *Advancing Medical Practice through Technology: Applications for Healthcare Delivery, Management, and Quality: Applications for Healthcare Delivery, Management, and Quality*. IGI Global, 2013.

[79] Lawrence G Rudski, Wyman W Lai, Jonathan Afilalo, Lanqi Hua, Mark D Handschumacher, Krishnaswamy Chandrasekaran, Scott D Solomon, Eric K Louie, and Nelson B Schiller. Guidelines for the echocardiographic assessment of the right heart in adults: a report from the american society of echocardiography: endorsed by the european association of echocardiography, a registered branch of the european society of cardiology, and the canadian society of echocardiography. *Journal of the American society of echocardiography*, 23(7):685–713, 2010.

[80] Javier Sanz, Mbabazi Kariisa, Santo Dellegrottaglie, Susanna Prat-González, Mario J Garcia, Valentin Fuster, and Sanjay Rajagopalan. Evaluation of pulmonary artery stiffness in pulmonary hypertension with cardiac magnetic resonance. *JACC: Cardiovascular Imaging*, 2(3):286–295, 2009.

[81] Patrick Segers, Nikos Stergiopulos, and Nico Westerhof. Quantification of the contribution of cardiac and arterial remodeling to hypertension. *Hypertension*, 36(5):760–765, 2000.

[82] W Seitz, Paolo Marino, L Zanolla, C Buonanno, M McIlroy, and M Spiel. Cardiac valve orifice equation independent of valvular flow intervals: application to mitral valve area computation in mitral stenosis and comparison with the gorlin formula and direct anatomical measurements. *Cardiovascular research*, 18(11):669–674, 1984.

[83] W Seitz, L Oppenheimer, D MCILROY, and J OPERSCHALL. Aortic valve orifice equation independent of valvular flow intervals: Application to aortic valve area computation inaortic stenosis and comparison with the gorlin formula. *European Heart Journal*, 7(12):1022–1029, 1986.

[84] WS Seitz, JD Hosenpud, and R Schutz. An orifice formula independent of mitral pressure gradient for the evaluation of prosthetic mitral valve obstruction. *European Heart Journal*, 5(11):932–940, 1984.

[85] NAGUEH SF. Recommendations for the evaluation of left ventricular diastolic function by echocardiography. *J Am Soc Echocardiogr*, 22:107–133, 2009.

[86] Sanjiv J Shah and Mihai Gheorghiade. Heart failure with preserved ejection fraction: treat now by treating comorbidities. *Jama*, 300(4):431–433, 2008.

[87] T Skjaerpe and L Hatle. Noninvasive estimation of systolic pressure in the right ventricle in patients with tricuspid regurgitation. *European Heart Journal*, 7(8):704–710, 1986.

[88] Tyler J Smith, Vinesh Appadurai, Muhammed Gercek, Kameswari Maganti, Jeesoo Lee, Michael Markl, and James D Thomas. Mathematical modeling of echocardiographic underestimation of right ventricular systolic pressure in severe tricuspid regurgitation. *Circulation*, 148(Suppl_1):A17220–A17220, 2023.

[89] N Stergiopulos, Patrick Segers, and N Westerhof. Use of pulse pressure method for estimating total arterial compliance in vivo. *American Journal of Physiology-Heart and Circulatory Physiology*, 276(2):H424–H428, 1999.

[90] V Sunder, R Cha, K Hunter, R Dolan, and Cooper Heart Institute. A modified dabestani-mahan formula estimates a normal pulmonary artery systolic pressure: a single-center retrospective study. *European Heart Journal*, 42(Supplement_1):ehab724–0147, 2021.

[91] Andrew J Swift, Smitha Rajaram, Judith Hurdman, Catherine Hill, Christine Davies, Tom W Sproson, Allison C Morton, Dave Capener, Charlie Elliot, Robin Condliffe, et al. Noninvasive estimation of pa pressure, flow, and resistance with cmr imaging: derivation and prospective validation study from the aspire registry. *JACC: Cardiovascular Imaging*, 6(10):1036–1047, 2013.

[92] Matteo Toma, Stefano Giovinazzo, Gabriele Crimi, Giovanni Masoero, Manrico Balbi, Fabrizio Montecucco, Marco Canepa, Italo Porto, and Pietro Ameri. Multiparametric vs. inferior vena cava–based estimation of right atrial pressure. *Frontiers in cardiovascular medicine*, 8:632302, 2021.

[93] Wen-Yih Isaac Tseng, Mao-Yuan Marine Su, and Yao-Hui Elton Tseng. Introduction to cardiovascular magnetic resonance: technical principles and clinical applications. *Acta Cardiologica Sinica*, 32(2):129, 2016.

[94] Rayji S Tsutsui, Allen Borowski, WH Wilson Tang, James D Thomas, and Zoran B Popović. Precision of echocardiographic estimates of right atrial pressure in patients with acute decompensated heart failure. *Journal of the American Society of Echocardiography*, 27(10):1072–1078, 2014.

[95] Jean-Louis J Vanoverschelde, Annie R Robert, Alain Gerbaux, Xavier Michel, Claude Hanet, and William Wijns. Noninvasive estimation of pulmonary arterial wedge pressure with doppler transmitral flow velocity pattern in patients with known heart disease. *The American journal of cardiology*, 75(5):383–389, 1995.

[96] José G Venegas, R Scott Harris, and Brett A Simon. A comprehensive equation for the pulmonary pressure-volume curve. *Journal of applied physiology*, 84(1):389–395, 1998.

[97] Nicolaas Westerhof, Nikolaos Stergiopulos, Mark IM Noble, and Berend E Westerhof. *Snapshots of hemodynamics: an aid for clinical research and graduate education*. Springer, 2018.

[98] Yaseen, Gui-Young Son, and Soonil Kwon. Classification of heart sound signal using multiple features. *Applied Sciences*, 8(12):2344, 2018.

[99] Paul G Yock and Richard L Popp. Noninvasive estimation of right ventricular systolic pressure by doppler ultrasound in patients with tricuspid regurgitation. *Circulation*, 70(4):657–662, 1984.

[100] Michael R Zile and Catalin F Baicu. Biomarkers of diastolic dysfunction and myocardial fibrosis: application to heart failure with a preserved ejection fraction. *Journal of cardiovascular translational research*, 6:501–515, 2013.

General Conclusion

This thesis has systematically explored the intersection of advanced signal processing techniques and artificial intelligence (AI) methodologies in the early detection and management of cardiac pathologies. As cardiovascular diseases (CVDs) continue to be a leading global health challenge, the need for innovative, non-invasive diagnostic methods is more pressing than ever.

The research has demonstrated that enhancing the analysis of phonocardiogram (PCG) signals through advanced signal processing not only improves the signal-to-noise ratio but also clarifies cardiac sounds, facilitating more accurate interpretations. By developing tailored machine learning algorithms, this work significantly contributes to the automation of pathological feature detection in PCG signals, paving the way for timely and precise diagnoses.

Furthermore, the exploration of non-invasive methods for estimating intracardiac pressure has revealed their potential to provide critical insights into conditions such as heart failure and valvular disorders, which are often challenging to evaluate with traditional techniques. The findings underscore the effectiveness and reliability of these non-invasive approaches, making a compelling case for their integration into routine cardiovascular assessments.

The integration of AI with conventional cardiac monitoring practices has been shown to enhance diagnostic accuracy and positively influence clinical outcomes. By proposing a comprehensive framework that incorporates these advanced techniques, this thesis lays the groundwork for a transformative approach to cardiac disease management, emphasizing the importance of timely clinical interventions.

In conclusion, the advancements presented in this thesis not only contribute to the academic understanding of cardiac diagnostics but also hold significant implications for clinical practice. The integration of advanced signal processing and AI technologies presents a promising pathway toward improving patient outcomes in cardiovascular care, ultimately fostering a future where early detection and effective management of cardiac pathologies are the standard. Future research should focus on the continued refinement of these technologies and their application in diverse clinical settings to maximize their impact on global health.